





## **Hybrid Integrated Mode-Locked Lasers Using Silicon Nitride External Cavities**

**Ewoud Vissers**

Doctoral dissertation submitted to obtain the academic degree of  
Doctor of Photonics Engineering

### **Supervisors**

Prof. Bart Kuyken, PhD - Kasper Van Gasse, PhD  
Department of Information Technology  
Faculty of Engineering and Architecture, Ghent University

July 2023



ISBN 978-94-6355-735-1

NUR 965

Wettelijk depot: D/2023/10.500/67

## **Members of the Examination Board**

### **Chair**

Prof. Em. Daniël De Zutter, PhD, Ghent University

### **Other members entitled to vote**

François Leo, PhD, Université libre de Bruxelles

Prof. Jeroen Missinne, PhD, Ghent University

Prof. Geert Morthier, PhD, Ghent University

Hans Wenzel, PhD, Ferdinand-Braun-Institut, Germany

### **Supervisors**

Prof. Bart Kuyken, PhD, Ghent University

Kasper Van Gasse, PhD, Ghent University



# Dankwoord

Had mij zes jaar geleden gevraagd of ik een doctoraat zou gaan doen, en je had een zeer resolute 'nee' als antwoord gekregen. Maar nu ligt hier toch dit boek. Wat is daar gebeurd?

Voor mijn master moest ik minstens 14 weken op stage. Ergens in Canada was daarvoor mijn idee, maar na redelijk vlot contact met een bedrijf in Vancouver ging dat last-minute toch niet meer door. Na een (onverwacht korte) zoektocht kwam ik dan terecht bij IMEC in Leuven, so glamorous... Toen ik daar begeleid werd door Ashwyn terwijl hij zijn eigen doctoraat deed, toonde hij toch de betere kantjes van het doen van een doctoraat. Na het afronden van mijn masterproef in Enschede was het ook Ashwyn die mij in contact had gebracht met Bart. Ashwyn, thanks for inspiring me with your enthusiasm, making me reconsider doing a PhD, and thank you so much for connecting me with Bart!

Bart is me ook een echte enthousiasteling! Terugkijkend op mijn emails bleek ik op 16 maart 2020 mijn eerste laser 'aan de praat' te hebben, maar kort daarna kwam de eerste lockdown, dus ging ik er niet aan kunnen meten. Maar Bart denkt out of the box: 'Heb jij ruimte voor een optische tafel in je appartement?' Gelukkig/jammergenoeg kwam een halve dag later het mailtje van Roel dat er absoluut niemand spullen uit het labo mee naar huis zou nemen. Bij die laser bleek uiteindelijk dat het bij 'lijken werken' bleef, dus ik ben toch blij dat die optische tafel er niet is gekomen, dat zou de lockdown nog net een stukje erger hebben gemaakt als ik daar toen al achter kwam.

Ook toen vastzitten in het onderzoek in plaats van de lockdown weer het probleem werd was een meeting met Bart in het labo een gegarandeerde manier om weer vol goede moed en met een frisse blik door te gaan. Kasper in het labo was al net zo handig, waarbij ik mij het vinden van het eerste mode-locking punt nog goed herinner. Ik had het na 4 uur opgegeven, maar met Kasper erbij, 'beetje meer stroom', 'beetje minder spanning', stond dat spectrum toch ineens stil, en bleken die lasers toch echt wel te kunnen locken. Merci voor al je enthousiasme en ideeën Kasper!

Iedereen uit Team Bart is ook onmisbaar geweest, met de vele discussies in het labo,

bij de koffie, of auto's ontwijkend onderweg naar Ally's. Vooral StijnP en Camiel wil ik nog extra bedanken, voor de vele e-beam runs en IPKISS code: 'Remember that the last point is special, and it's best to make it double!' Volgens mij zou ik voor al die ebeam-runs nog een keer iets voor jullie bakken, dus dat komt er zeker nog eens aan. Ook stijnC: Heel erg bedankt voor de handige discussies in de laatste maanden van mijn onderzoek, wanneer ik weer eens met een vraag uit de lucht kwam vallen. Dat heeft me zeker vooruit geholpen!

In de cleanroom stond ik er ook niet alleen voor: Merci Steven om na mijn elfde aanvraag voor een verdund LioniX sample dat nog steeds te willen doen! En Liesbet: Nogmaals mijn excuses voor mijn FIB slot om 16:00 dat vanwege de techniker (die echt niet naar huis wilde) om 17:20 uitgesteld was naar vroeg de dag nadien. Het kwam niemand uit, maar het was zeker gezellig!

Voor in de meetkamer wil ik JasperJ bedanken, ik heb er elke keer van genoten om in de diepste krochten van onze vakgroep op zoek te gaan naar net die passende stage. Als we dat passende stukje niet gevonden hebben stond daar altijd Peter klaar om het dan zelf te maken. Als het dan uiteindelijk (in de meting, of daarbuiten) op puzzelen uitkwam, was daar nog altijd de hulp van Clemens, merci!

I would also like to thank all of my jury members, for taking the time to review my manuscript and providing me with feedback to improve the quality of the manuscript.

Wanneer het niet over het onderzoek ging ben ik ook zeer dankbaar voor veel mensen aan de onderzoeksgroep. Emmanuel: bedankt voor de dagelijkse telefoontjes tijdens de lockdown (en daarna). Het is na de lockdown niet meer zo frequent nu er weer naar igent gependeld moet worden, maar ik kijk er nog steeds weer altijd naar uit! StijnP: Zo ongeveer samen begonnen bij dezelfde promotor hebben wij veel samen gedaan, maar het liefst herinner ik mij de mooie vakanties, met de Bag Raiders en the War on Drugs, en in de file staan richting Ikea Hasselt staat hoe vreemd dat ook klinkt ook op dat lijstje.

Ook heb ik het genoeg gehad om mijn werk te kunnen doen vanuit het beste bureau in de groep. Er kon over werk gebabbeld worden, maar daarbuiten was er ook altijd genoeg te bespreken: Van mood indices, via soup tier list (eigenlijk Max' ding) tot short gaan op Rockley photonics (Ik had zo rijk kunnen worden). De sfeer zat er altijd goed in, bedankt daarvoor! Ik wil ook zeker ons lunchteam niet vergeten. We passen tegenwoordig niet meer aan één tafel, en eigenlijk ook niet meer in de koffie-corner, maar dat maakt het er wat mij betreft alleen maar gezelliger op!

Dan is er natuurlijk nog het leven buiten de onderzoeksgroep. Ik weet nog goed hoeveel stress ik had voor mijn auditie bij het GUK, maar dat was het allemaal dubbel en dwars waard! De repetities, concerten, weekends en reizen heb ik altijd naar uitgekeken. Ook daarnaast was er genoeg non-muzikaals te doen: van opgepropt op overvolle spelletjesavonden in Gent, tot kleddernat geregend in een

Vlaams gehucht op de GR. Zonder alle GUKkers was dat allemaal nooit gebeurd, dus merci daarvoor, jullie allemaal! En Joris, dat hebben we allemaal nog het meest aan jou te danken!

Als laatste rest mij nog om papa, mama, Anne en Judith te bedanken. We zijn er een (iets te) internationale familie op geworden, maar toch kan ik altijd nog bij jullie terecht, fysiek of bij de bijna wekelijkse facetime. Bedankt voor alle steun en interesse naar het onderzoek de laatste 4.5 jaar, en vooral om mij oppeppers te geven en mij terug aan het schrijven te krijgen wanneer ik dat nodig had. Anders was dit boek er dit jaar zeker niet meer gekomen.

Als allerlaatste ben ik ongetwijfeld nog belangrijke mensen vergeten. Bedankt aan iedereen die mij gesteund heeft doorheen de jaren, zowel op als naast het werk!

*Ewoud Vissers  
Gent, juni 2023*



# Contents

<b>Dankwoord</b>	<b>i</b>
<b>Contents</b>	<b>v</b>
<b>List of Acronyms</b>	<b>ix</b>
<b>Samenvatting</b>	<b>xiii</b>
1    Inleiding . . . . .	xiii
2    Resultaat . . . . .	xv
3    Conclusie . . . . .	xvii
<b>Summary</b>	<b>xix</b>
1    Introduction . . . . .	xix
2    Result . . . . .	xx
3    Conclusion . . . . .	xxiii
<b>1 Introduction</b>	<b>1</b>
1.1 Photonic integrated circuits . . . . .	1
1.2 Light generation for silicon (nitride) PICs . . . . .	3
1.2.1 Hybrid integration . . . . .	4
1.2.2 Heterogeneous integration . . . . .	5
1.3 Optical frequency combs . . . . .	6
1.3.1 Applications of frequency combs . . . . .	8
1.3.2 Kerr combs . . . . .	9

1.3.3	Electro-optic combs . . . . .	10
1.3.4	Mode-locked lasers . . . . .	11
1.4	Research objectives . . . . .	11
1.5	Thesis outline . . . . .	12
1.6	List of publications . . . . .	12
1.6.1	Publications in international journals . . . . .	12
1.6.2	Publications in international conferences . . . . .	12
<b>2</b>	<b>Extended cavity mode-locked lasers</b>	<b>15</b>
2.1	Introduction to lasers . . . . .	15
2.1.1	Gain media . . . . .	16
2.1.2	Semiconductor optical amplifier . . . . .	17
2.2	Mode-locked lasers . . . . .	20
2.2.1	Active mode-locking . . . . .	20
2.2.2	Saturable absorption . . . . .	21
2.2.3	Stable mode-locking points . . . . .	22
2.2.4	Integrated MLL architectures . . . . .	25
2.2.5	Self mode-locked lasers . . . . .	26
2.3	External cavity MLLs . . . . .	26
2.3.1	Laser noise . . . . .	26
2.3.2	Evolution of integrated MLLs . . . . .	30
2.3.3	Applicability of hybrid integrated ECMLLs . . . . .	32
<b>3</b>	<b>Design of hybrid-integrated extended-cavity mode-locked lasers</b>	<b>35</b>
3.1	SiN extended cavities . . . . .	36
3.1.1	On chip reflector . . . . .	36
3.1.2	Off-chip coupling . . . . .	39
3.2	Gain chips on MPW platforms . . . . .	50
3.2.1	HHI InP platform . . . . .	50

3.2.2	SMART InP platform . . . . .	53
3.3	Gain chips on C-mount . . . . .	55
3.3.1	Post-processing for SA fabrication . . . . .	55
3.3.2	Innolume gain chips . . . . .	60
3.3.3	FBH gain chips . . . . .	62
3.4	Details of fabricated cavity chips . . . . .	65
3.4.1	Design and simulation procedures . . . . .	65
3.4.2	Parameters of used chips . . . . .	69
<b>4</b>	<b>Characterization of hybrid-integrated extended cavity MLLs</b>	<b>71</b>
4.1	Aligning gain and cavity chips . . . . .	72
4.1.1	Permanent butt-coupling . . . . .	72
4.1.2	Non-permanent butt-coupling setup . . . . .	73
4.2	Mode-locked laser using the SMART MPW gain chip . . . . .	75
4.2.1	Short laser cavity . . . . .	77
4.2.2	Long laser cavity . . . . .	79
4.3	Self mode-locked laser . . . . .	82
4.4	Mode-locked laser at 1064 nm . . . . .	84
4.4.1	Chip-Chip coupling loss . . . . .	84
4.4.2	LI curves . . . . .	86
4.4.3	Mode-locking points . . . . .	87
4.4.4	Heterodyne optical linewidth measurement . . . . .	89
4.4.5	Injection locking . . . . .	92
4.5	Comparison of demonstrated integrated ECMLLs . . . . .	99
4.5.1	Comparison of the presented 1550 nm and 1064 nm MLLs	99
4.5.2	Comparison to other demonstrated hybrid integrated ECMLLs	100
<b>5</b>	<b>Conclusion and outlook</b>	<b>105</b>
5.1	Conclusions . . . . .	105

5.2 Outlook . . . . .	106
<b>References</b>	<b>R-1</b>

# List of Acronyms

ACPML	Anti-Colliding Pulse Mode-locked Laser
AM	Amplitude Modulation
AOM	Acousto-Optic Modulator
CPML	Colliding Pulse Mode-locked Laser
DAQ	Data AcQuisition system
DC	Directional Coupler
ECMLL	Extended Cavity Mode-Locked Laser
EDFA	Erbium Doped Fiber Amplifier
EO	Electro-Optic
ESA	Electrical Spectrum Analyzer
FIB	Focused Ion Beam
FM	Frequency Modulation
FP	Fabry-Pérot
FSR	Free Spectral Range
FWHM	Full width at Half Maximum
HR	High Reflectivity
HWHM	Half Width at Half Maximum
MLL	Mode-Locked Laser
MPW	Multi Project Wafer
MIR	Multi-mode Interference Reflector
MMI	Multi-Mode Interference
OSA	Optical Spectrum Analyzer
PIC	Photonic Integrated Circuit
QCSE	Quantum Confined Stark Effect

RSOA	Reflective Semiconductor Optical Amplifier
SA	Saturable Absorber
SCPML	Self-Colliding Pulse Mode-locked Laser
SOA	Semiconductor Optical Amplifier
SSC	Spot Size Converter

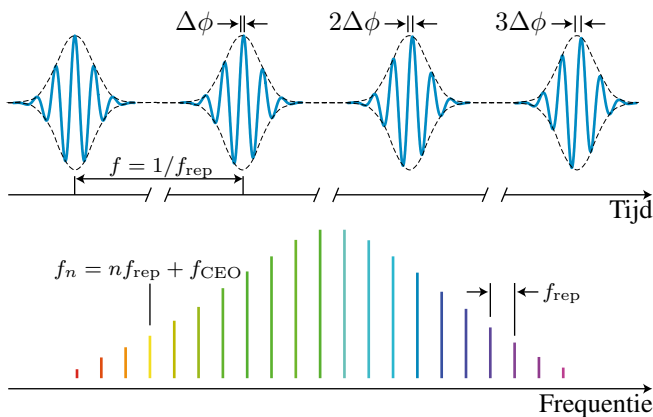




# Samenvatting

## 1 Inleiding

Optische frequentiekammen zijn een type licht dat voor verschillende doeleinden kan worden gebruikt, zoals spectroscopie, snellere telecommunicatie en LIDAR [1]. Hun tijdsdomein en frequentie-domein representatie wordt getoond in Fig. 1. The voornaamste reden voor de interesse in optische frequentiekammen is de simpele vergelijking voor de optische frequenties van elke individuele lijn:  $f_n = n f_{\text{rep}} + f_{\text{CEO}}$  Optische frequentiekammen zijn reeds gedemonstreerd in glasvezelgebaseerde systemen, die gebruikt worden in toepassingen waar de grote omvang van deze systemen geen probleem vormt, bijvoorbeeld voor de kalibratie van astronomische spectrografen [2]. Als deze frequentiekammen zouden kunnen worden gegenereerd in een geïntegreerd fotonisch chipsysteem, zouden nieuwe toepassingen mogelijk zijn door de kleinere afmetingen en door massafabricage de lagere prijs van de frequentiekambron.



Figuur 1: Schematische representatie van een frequentiekam in zowel het tijdsdomein als het frequentie-domein. Figuur uit [3]

Momenteel zijn de belangrijkste materiaalplatformen voor fotonische integratie InP, Si en SiN. InP wordt vooral gebruikt omdat het gemakkelijk is actieve componenten

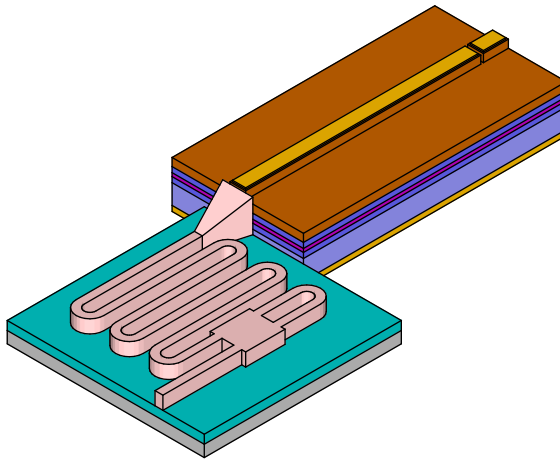
te integreren, waaronder halfgeleider optische versterkers (SOAs). Si wordt gebruikt vanwege de bestaande bewerkingskennis uit de geïntegreerde elektronica-industrie. SiN wordt vooral gebruikt vanwege de zeer lage propagatieverliezen die kunnen worden bereikt. In Si of SiN is het niet mogelijk om efficiënt licht te genereren. Om licht in een fotonische chip van Si of SiN te krijgen, zijn er twee opties. De ene optie is het gebruik van een externe lichtbron. De andere optie is het gebruik van een tweede materiaalplatform dat lichtgeneratie mogelijk maakt. Dit tweede platform moet worden geïntroduceerd via een integratiemethode, heterogene of hybride integratie. Bij heterogene integratie wordt het secundaire materiaal vroeg in het proces ingebracht, bovenop het primaire materiaal. Dit heeft het voordeel dat de integratie parallel kan gebeuren, voor vele chips tegelijk. Een nadeel is dat het productieproces moet worden aangepast om voor zowel het primaire als het secundaire materiaalsysteem te werken. Hybride integratie is een techniek waarbij twee afzonderlijke chips worden vervaardigd, één voor elk materiaalplatform. Deze worden dan na de fabricage één voor één gekoppeld. Dit is tijdrovender dan heterogene integratie voor grote volumes, maar heeft het voordeel dat het fabricageproces voor beide materiaalsystemen niet gewijzigd hoeft te worden.

De eerste geïntegreerde mode-locked lasers werden gemaakt als monolithische chips in III/V-materialen, omdat dit efficiënte versterkingsmaterialen zijn. De lasercaviteit werd gemaakt van een golfgeleider in het actieve III/V-materiaal, terwijl gekleefde (en soms ook gecoate) facetten van de golfgeleider fungeerden als de spiegels van de caviteit. Een klein deel van de golfgeleider was elektrisch geïsoleerd van de rest, om de verzadigbare absorbeerder te definiëren. Dit soort lasers had korte caviteiten, waardoor de herhalingsfrequenties boven de 10 GHz lagen. Bovendien waren de verliezen in de actieve III/V-golfgeleider relatief hoog. Daardoor was de fundamentele Schawlow-Townes-lijnbreedte ook breed, waardoor de optische en RF-lijnbreedte zeer breed waren.

Om de lijnbreedte te kunnen verlagen moest de lengte van de caviteit van geïntegreerde lasers worden vergroot zonder veel optisch verlies toe te voegen. Voor relatief hoge herhalingsnelheden kon dit efficiënt gebeuren door gebruik te maken van actieve-passieve integratie in een monolithisch III/V-platform. Met deze techniek kunnen twee soorten golfgeleiders op één chip worden gebruikt: een actieve golfgeleider kan worden gebruikt als optische versterker (SOA), terwijl de passieve variant gebruikt kan worden voor golfgeleiders met laag verlies. Bij lagere herhalingsfrequenties wordt het voordelig om over te schakelen op Si of SiN-golfgeleiders in plaats van de passieve III/V-golfgeleiders, vanwege het nog lagere verlies. Hier wordt de heterogene of hybride integratie noodzakelijk, om een (III/V) materiaal met efficiënte optische versterking te integreren met een golfgeleiderplatform met lage verliezen.

## 2 Resultaat

Alle in dit werk gepresenteerde lasers maken gebruik van een zeer vergelijkbaar extern SiN caviteitsontwerp. Voor de SiN-golfgeleiders op deze chip wordt slechts één patroon- en etsstap gebruikt, en er wordt een extra stap in het proces geïntroduceerd om SU8 modus-grootte omzetters toe te voegen. Deze omzetters maken een weinig verliesgevende koppeling met vele verschillende gain-chips mogelijk, omdat zowel de breedte als de hoogte van de uitgangsmodus gemakkelijk kunnen worden afgestemd. Hierdoor kan hetzelfde caviteitsontwerp worden gebruikt voor een breed scala aan versterkingschips. Een conceptuele representatie van de laser wordt getoond in Fig. 2.

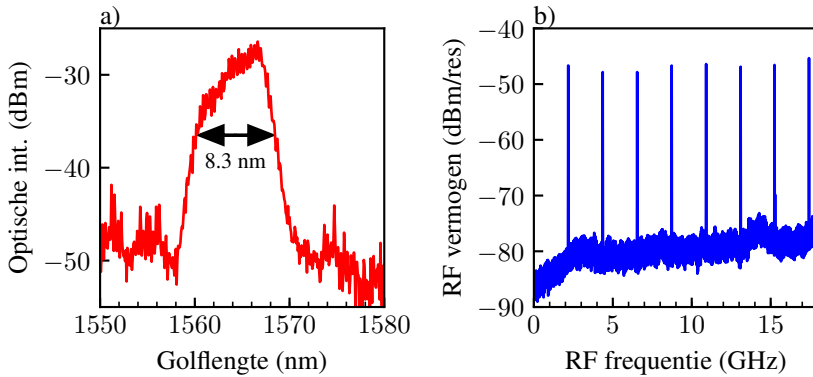


*Figuur 2: Conceptuele representatie van de externe-caviteit mode-locked lasers die gebruikt worden in dit werk.*

Deze caviteit chips kunnen worden gebruikt in combinatie met een reflectieve halfgeleider versterkingschip (RSOA) om een (mode-locked) laser te vormen. In dit geval functioneert het achterste facet van de RSOA als de primaire (sterk reflecterende) spiegel. Indien een verzadigbare absorbeerder (SA) aanwezig is, wordt deze direct naast de primaire spiegel geplaatst. Deze wordt dan gevolgd door een versterkingssectie, die onder een kleine hoek stopt bij het facet van de versterkingschip. De SiN caviteits-chip wordt aan dit facet gekoppeld, en een SU8 modus-grootte omzetter zorgt voor een weinig verliesgevende koppeling. Na de modus-grootte omzetter komt een vertragingslijn met laag verlies, die de FSR van de lasercaviteit bepaalt. Na de vertragingslijn wordt de lasercaviteit afgesloten met een secundaire spiegel in de vorm van een Sagnac-spiegel. Deze spiegel zendt ook een deel van het licht door, dat wordt gebruikt als uitvoer van de laser. Dat uitgangslight wordt geleid naar een tweede modus-grootte omzetter aan het

chipfacet, die wordt gebruikt om de laseruitgang te koppelen aan een gelensde glasvezel.

Dit SiN-ontwerp van de lasercaviteit is gebruikt om drie verschillende, geteste, modusvergrendelde lasers te maken. De eerste laser werkt op 1550 nm en gebruikt een versterkingschip gemaakt in het InP MPW-platform van SMART Photonics. Een ontwerp met een herhalingsfrequentie van 15,8 GHz en één met een herhalingsfrequentie van 2,18 GHz werden gedemonstreerd, beide gekoppeld aan exact dezelfde versterkingsstructuur op de InP chip. Door de langere levensduur van de fotonen in de 2,18 GHz laser was de RF-lijnbreedte aanzienlijk kleiner dan bij de 15,8 GHz laser. De fundamentele RF lijnbreedte van de 2,18 GHz laser werd bepaald met een faseruis meting, en was 31 Hz. Het optische- en RF-spectrum bij het optimale werkingpunt worden getoond in Fig. 3.



*Figuur 3: a) toont het optische spectrum en b) toont het RF spectrum bij het optimale werkingpunt van de SMART laser gekoppeld aan een lange externe caviteit.*

De tweede laser die werd getest was een ontwerp dat werkte op 1310 nm, met een commercieel verkrijgbare versterkingschip van Innolume. In deze laser was geen verzadigbare absorbeerder (SA) gedefinieerd in de lasercaviteit. Zonder een SA kunnen lasers nog steeds mode-locked zijn, via vier-bundel-mengprocessen in de caviteit, wat zelf mode-locking wordt genoemd. Helaas werd op geen enkel punt waar deze laser werd bediend mode-locking gedetecteerd. Er wordt aangenomen dat dit kwam doordat er geen element in de lasercaviteit was met anomalische dispersie, dat wel aanwezig was in een zeer vergelijkbare mode-locked laser die werd gepresenteerd [4].

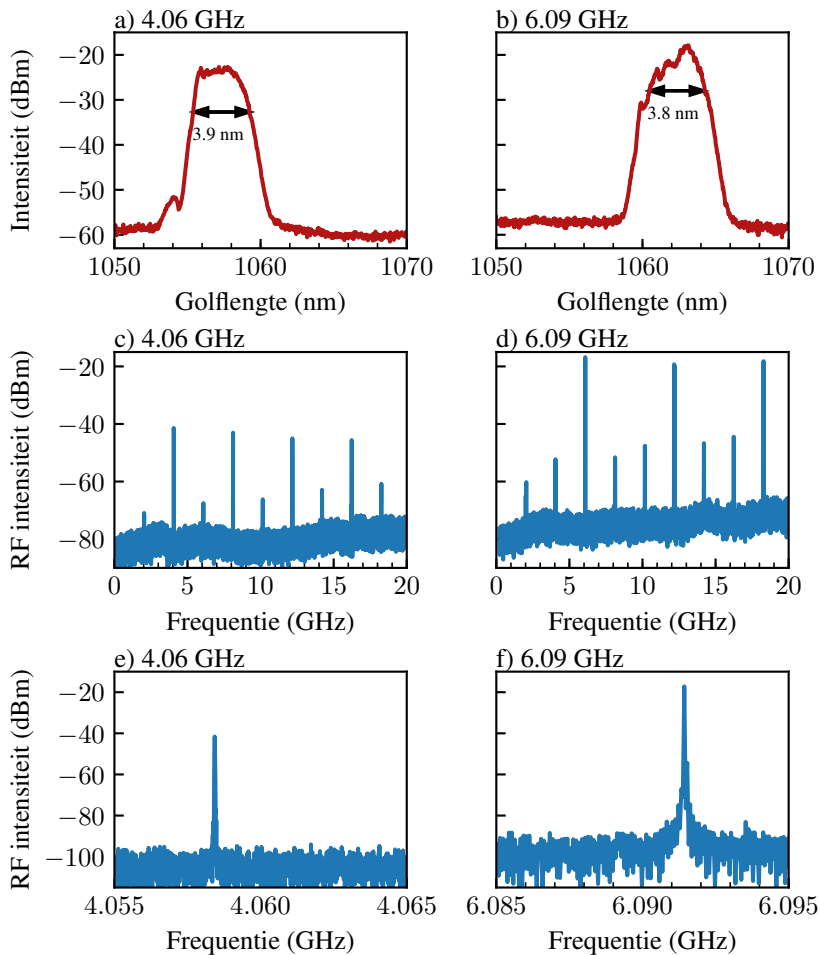
De laatste laser die werd getesd was een laser die werkte op 1060 nm, met een aangepaste versterkingschip uit een samenwerking met FBH, met een SA. De lasercaviteit had een FSR van 2,03 GHz, maar mode-locking werd alleen gemeten op de tweede en derde harmonische, voor herhalingsfrequenties van 4,06 en

6,09 GHz. De spectra bij deze operatiepunten worden getoond in Fig. 4. Voor het mode-locking punt bij 6,09 GHz was een externe fiber laser beschikbaar die overlapte met het optische spectrum van de MLL output. Deze laser werd gebruikt voor een heterodyne meting om de optische lijnbreedte van de MLL te meten. Uit deze meting bleek dat de bovengrens voor de optische lijnbreedte 4,5 MHz bedroeg. Ook bleek dat de optische lijnfrequenties van de laser zeer onstabiel waren, waarschijnlijk als gevolg van technische ruisbronnen. Daarom werd dezelfde externe laser gebruikt om de stabiliteit van één lijn in de frequentiekam te verhogen door middel van injectievergrendeling. De injectievergrendeling werkte, en met behulp van de fijnafstemming van de externe laser kon de injectievergrendelde lijn worden verplaatst over 14 pm, begrensd door het fijnafstembereik van de externe laser.

### 3 Conclusie

Er is aangetoond dat hybride integratie kan worden gebruikt om geïntegreerde mode-locked lasers te maken met een lage herhalingsfrequentie en een smalle RF-lijnbreedte. Ook is gebleken dat de laser in de gebruikte uitlijnings- en meetopstelling de laserlijnen doet verlopen. Dit verloop kon voor een enkele lijn worden gestopt door injectievergrendeling met een externe vezellaser. Dit vergrendelingsproces neemt wel het groottevoordeel weg dat geïntegreerde modusvergrendelde lasers bieden ten opzichte van reeds bestaande vezelgebaseerde modusvergrendelde lasers. Als een voldoende stabiele geïntegreerde laser met één frequentie kan worden gemaakt, zou de injectievergrendeling kunnen worden uitgevoerd met een geïntegreerde laser.

De drijvende laserlijnen zouden voor een groot deel kunnen worden veroorzaakt door de uitlijning die wordt gebruikt voor het koppelen van de chips. Dit probleem zou kunnen worden verminderd wanneer de hybride geïntegreerde laser wordt verpakt, aangezien de chips dan niet meer ten opzichte van elkaar kunnen bewegen. Dit probleem zou ook kunnen worden beperkt door over te stappen op heterogene integratie. Verder zou kunnen worden gewerkt aan de implementatie van hybride mode-locking in geïntegreerde MLL's om ook de herhalingsfrequentie van de kam te stabiliseren. Hierdoor zouden geïntegreerde MLL's kunnen worden gebruikt voor nauwkeurige (dubbele) frequentiespectroscopie. Zelfs zonder de stabilisatietechnieken zouden de lasers kunnen worden gebruikt voor LIDAR-toepassingen en voor spectroscopietoepassingen waarbij een referentiemateriaal kan worden gebruikt voor kalibratie.



Figuur 4: De optische en elektrische spectra op het 4 en 6 GHz werkingpunt. a) and b) tonen het optische spectrum met de -10 dB bandbreedte aangegeven c) and d) het RF spectrum over een groot bereik, and e) and f) tonen een zoom van de mode-locking piek in het RF spectrum. a), c) and e) tonen het 4 GHz werkingpunt, and b), d) and f) tonen het 6 GHz werkingpunt.

# Summary

## 1 Introduction

Optical frequency combs are a type of light that could be used for different purposes such as spectroscopy, faster telecommunications, and LIDAR [1]. Their time-domain and frequency-domain representation are shown in Fig. 5. The main reason why frequency combs are of interest is the simple relation for the optical frequencies of each individual line:  $f_n = n f_{\text{rep}} + f_{\text{CEO}}$ . Optical frequency combs have already been demonstrated in fiber-based systems, which are used in applications where the large size of these systems does not pose a problem, for example for the calibration of astronomical spectrographs [2]. If these frequency combs could be generated in an integrated photonic chip system, new applications could be enabled through the reduction in size and through mass-fabrication the reduction in price of the frequency comb source.

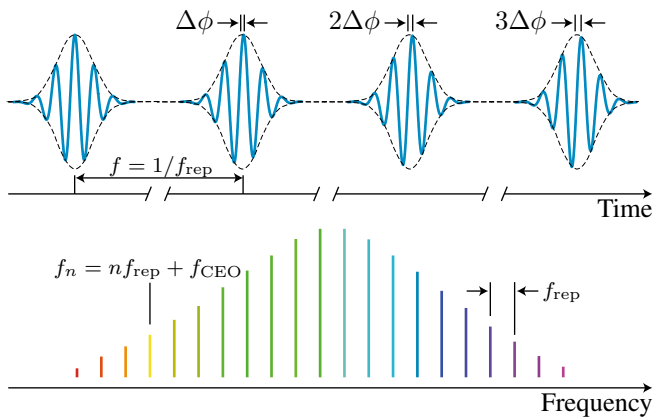


Figure 5: Schematic representation of a frequency comb in both the time domain and the frequency domain. Figure from [3]

Currently, the main material platforms for photonic integration are InP, Si, and SiN. InP is used mainly because it is easy to integrate active components, including Semiconductor Optical Amplifiers (SOAs). Si is used because of the processing

knowledge coming from the integrated electronics industry. SiN is mainly used because of the very low propagation losses that can be achieved. In Si or SiN, it is not possible to generate light efficiently. In order to get light into a Si or SiN photonic chip, there are two options. One option is to use an external light source. The other option is to use a second material platform that enables light generation. This second platform has to be introduced using an integration method, either heterogeneous or hybrid integration. With heterogeneous integration, the secondary material is introduced early on in the process, on top of the primary material. This has the advantage that the integration can be done in parallel, for many chips at the same time. A disadvantage is that the process needs to be adjusted to work for both the primary and secondary material systems. Hybrid integration is a technique where two separate chips are fabricated, one for each material platform. They are then integrated together one by one after the fabrication. This is more time-consuming compared to heterogeneous integration for large volumes, but it has the advantage that the fabrication process for both material systems does not need to be altered.

The first integrated mode-locked lasers were made as monolithic chips in III/V materials because these are efficient gain materials. The laser cavity was made from a waveguide in the active III/V material, while cleaved (and sometimes coated) facets of the waveguide acted as the cavity mirrors. A small section of the waveguide was electrically isolated from the rest, to define the saturable absorber. These types of lasers had short cavities, causing the repetition rates to be above 10 GHz. Additionally, the losses in the active III/V waveguide were relatively high. Therefore the Schawlow-Townes fundamental linewidth was also broad, meaning the optical- and RF beat note linewidth were very broad.

In order to decrease the linewidth, the cavity length of integrated lasers had to be increased without adding much optical loss. For relatively high repetition rates this could be done efficiently using active-passive integration in a monolithic III/V platform. With this technique, two types of waveguides can be used on a single chip: an active waveguide can be used as an SOA, while the passive waveguide can be used for low-loss waveguides. At lower repetition rates, switching to Si or SiN waveguides instead of the passive III/V waveguides becomes beneficial, because of the even lower loss. This is where the heterogeneous or hybrid integration becomes necessary, to integrate a (III/V) material with efficient optical gain with a low-loss waveguide platform.

## 2 Result

All lasers presented in this work use a very similar SiN external cavity design. Only one pattern and etch step is used for the SiN waveguides, and an extra step is introduced into the process to enable the fabrication of spot-size converters in SU8. These converters enable low-loss coupling to many different gain-chips, due

to the easy tunability of both the width and height of the output mode. This allows the same cavity design to be useful for a wide range of gain chips. A conceptual representation of the device is shown in Fig. 6.

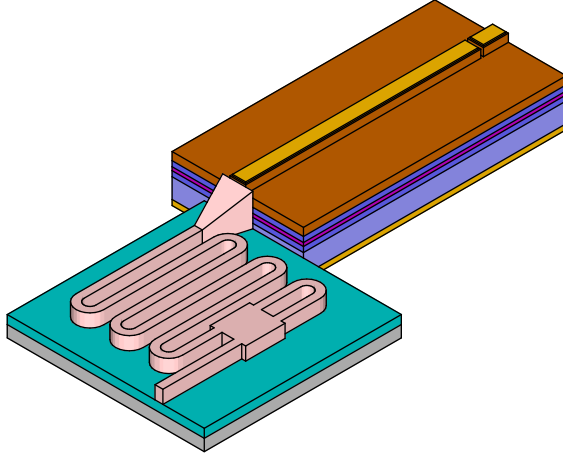


*Figure 6: Schematic overview of the extended cavity mode-locked lasers used in this work.*

These cavity chips can be used in combination with an RSOA gain chip to form a (mode-locked) laser. In this case, the rear facet of the RSOA acts as the primary (highly reflective) mirror. If an SA is present, this is placed directly next to the primary mirror. This is followed by a gain section SOA, which stops at the gain-chip facet under a small angle. The SiN cavity chip is butt-coupled to this facet, and a SU8 spot-size converter assures low-loss coupling. After the spot-size converter is a low-loss delay line, which determines the FSR of the laser cavity. After the delay line, the laser cavity is closed using a secondary mirror in the form of a Sagnac mirror. This mirror also transmits part of the light, which is used as the output of the laser. That output light is routed to a second spot-size converter at the chip facet which is used to couple the laser output to a lensed fiber.

This SiN cavity design has been used to make three different mode-locked lasers that were tested. The first laser works at 1550 nm and uses a gain chip made in the InP MPW platform of SMART Photonics. A design with a repetition rate of 15.8 GHz and one with a repetition rate of 2.18 GHz were demonstrated, both while coupled to the exact same gain structure on the InP chip. Due to the longer photon lifetime in the 2.18 GHz laser, the RF linewidth was significantly narrower compared to the 15.8 GHz laser. The fundamental RF linewidth of the 2.18 GHz laser was extracted from a phase noise measurement and was 31 Hz. The optical and RF spectrum at the optimal operating point of the 2.18 GHz laser is shown in Fig. 7.

The second laser that was tested was a design working at 1310 nm, using a com-

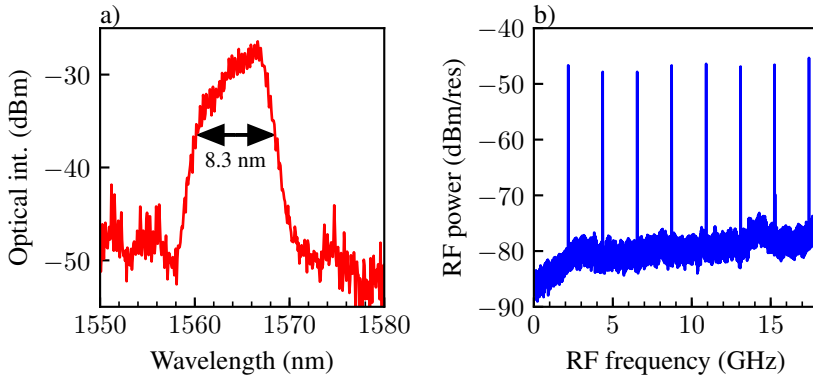


Figure 7: a) shows the optical spectrum and b) shows the RF spectrum at the optimal operating point of the SMART laser coupled to a long cavity.

mercially available gain chip from Innolume. In this laser, no saturable absorber was defined in the cavity. Without an SA, lasers can still be mode-locked, through four-wave-mixing processes in the cavity [5], which is called self-mode-locking. Unfortunately, no mode-locking was detected at any point where this laser was operated. It is assumed this was because there was no element in the cavity with anomalous dispersion, which was present in a very similar mode-locked laser that was presented [4].

The last laser that was measured was a laser working at 1060 nm, using a custom gain chip from a collaboration with FBH, with an SA. The laser cavity had an FSR of 2.03 GHz, but mode-locking was only measured at the second and third harmonic, for repetition rates of 4.06 and 6.09 GHz. The spectra at these operating points are shown in Fig. 8 For the mode-locking point at 6.09 GHz, an external fiber laser was available that overlapped the optical spectrum of the MLL output. This laser was used for a heterodyne measurement to measure the optical linewidth of the MLL. This measurement showed the upper bound for the optical linewidth to be 4.5 MHz. It also showed that the optical line frequencies of the laser were very unstable, likely due to technical noise sources. Therefore, the same external laser was used to increase the stability of one line in the frequency comb using injection locking. The injection locking worked, and using the fine-tuning of the external laser, the injection locked line could be moved over 14 pm, limited by the fine-tuning range of the external laser.

### 3 Conclusion

It has been demonstrated that hybrid integration can be used to make integrated mode-locked lasers with a low repetition rate and narrow RF linewidth. It has also been found that the laser in the alignment and measurement setup used does cause the laser lines to drift. This drift could be stopped for a single line by using injection locking with an external fiber laser. This injection-locking process does remove the size benefit that is brought by integrated mode-locked lasers over already existing fiber-based mode-locked lasers. If a stable enough integrated single-frequency laser can be built, the injection locking could be done using an integrated laser.

The drifting laser lines could be caused for a large part by the alignment setup used for butt-coupling the chips. This problem could be mitigated when the hybrid integrated laser is packaged since the chips can't vibrate in respect to each other anymore. This problem could also be mitigated by moving to heterogeneous integration. Further work could be done to implement hybrid mode-locking in integrated MLLs to stabilize the repetition rate frequency of the comb as well. This would enable integrated MLLs to be used for precision (dual) frequency comb spectroscopy. Even without the stabilization techniques, the lasers could be used for LIDAR applications, as well as spectroscopy applications where a reference sample can be used for calibration.

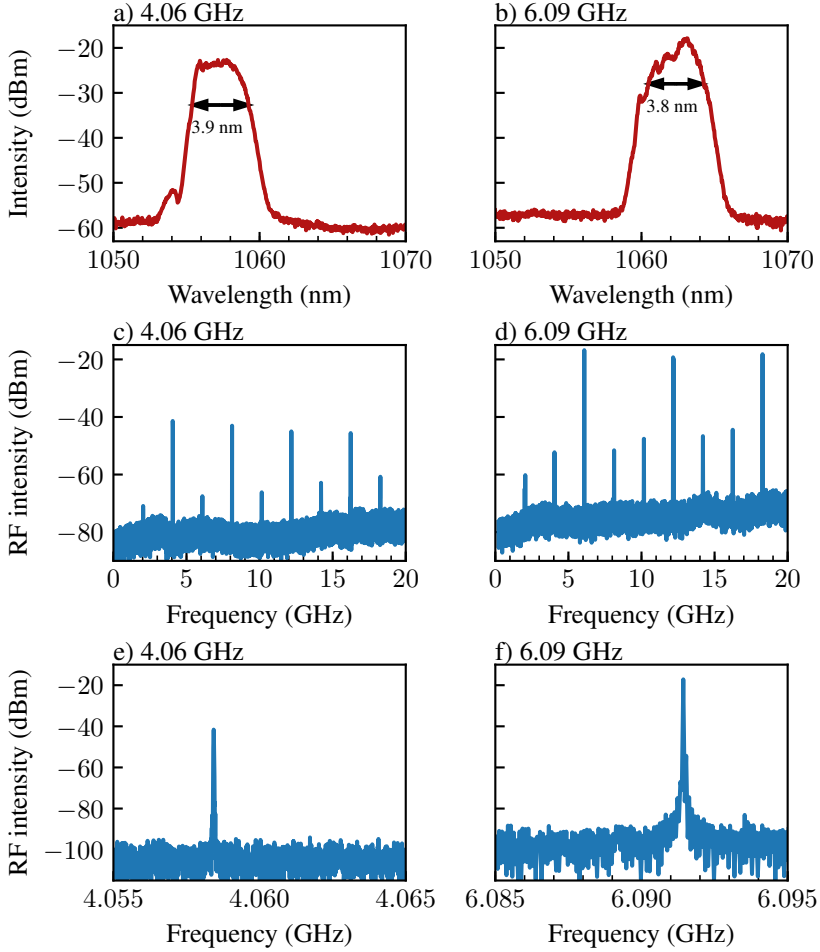


Figure 8: The optical and electrical spectrum at the 4 and 6 GHz mode-locking points. a) and b) show the optical spectrum with the 10dB bandwidth indicated, c) and d) the RF spectrum over a large span, and e) and f) show a tighter zoom on the mode-locking peak in the RF spectrum. a), c) and e) show the 4 GHz operating point, and b), d) and f) show the 6 GHz operating point.

# 1

## Introduction

---

<b>1.1 Photonic integrated circuits . . . . .</b>	<b>1</b>
<b>1.2 Light generation for silicon (nitride) PICs . . . . .</b>	<b>3</b>
1.2.1 Hybrid integration . . . . .	4
1.2.2 Heterogeneous integration . . . . .	5
<b>1.3 Optical frequency combs . . . . .</b>	<b>6</b>
1.3.1 Applications of frequency combs . . . . .	8
1.3.2 Kerr combs . . . . .	9
1.3.3 Electro-optic combs . . . . .	10
1.3.4 Mode-locked lasers . . . . .	11
<b>1.4 Research objectives . . . . .</b>	<b>11</b>
<b>1.5 Thesis outline . . . . .</b>	<b>12</b>
<b>1.6 List of publications . . . . .</b>	<b>12</b>
1.6.1 Publications in international journals . . . . .	12
1.6.2 Publications in international conferences . . . . .	12

---

### 1.1 Photonic integrated circuits

We are currently living in the information age, which is enabled by the availability of electronics. This started with the demonstration of the first transistor by J.

Bardeen, W. Brattain, and W. Shockley at Bell labs in 1947 [6] Its significance was soon recognized, since the Nobel Prize in Physics of 1956 was awarded for this invention [6]. The Nobel Prize in Physics of the year 2000 was also significant for the electronics industry, since it awarded half of the prize to Jack Kilby, for his part in the invention of the integrated circuit in 1958 [7]. The integrated circuits have then been improved year after year, starting from a circuit using 2 transistors on a 16 mm<sup>2</sup> chip, to currently the AD102 GPU in the NVIDIA RTX4090 containing 76 billion transistors on a 608 mm<sup>2</sup> die [8].

Photonics could be following a similar trend. A very important Nobel Prize related to photonics was awarded in 1964 to C.H. Townes, N.G. Basov and A.M. Prokhorov, “*for fundamental work in the field of quantum electronics, which has led to the construction of oscillators and amplifiers based on the maser-laser principle*” [9]. The first laser was demonstrated in 1960. In 1970, two breakthroughs happened around the same time, when the first working semiconductor laser was demonstrated [10], as well as the first optical fibers with a transmission loss below 20 dB/km [11]. Together, these inventions would form the basis for optical fiber communications, which powers the internet as it is today.

With the introduction of the semiconductor laser, on-chip circuit integration became a possibility. The first Photonic Integrated Circuit (PIC) was demonstrated in 1987 [12, 13]. Following in the footsteps of the electronics industry, this was followed by the standardization of building blocks, opening up the possibility of offering Multi Project Wafer (MPW) runs, which were first fabricated in 2008, both in InP and Silicon material systems [12]. This allows anyone to make designs for photonic integrated circuits, and receive their fabricated chips within a few months.

Differently from the electronics integration industry, there is not one material of choice for photonic integrated circuits. Three different mature material platforms are the main choices nowadays: indium phosphide (InP), silicon (Si) and silicon nitride (SiN). Each material has specific advantages and drawbacks, which are summarized in table 1.1.

**Indium Phosphide** is the only mature platform nowadays where light sources can be defined in the material itself during the fabrication of the chips, while in the other two platforms the light sources need to be made from a different material and coupled to the chip. The drawbacks of InP platforms are the relatively high optical propagation losses limiting the amount of components that can feasibly be integrated, and relatively large minimum bend radii increasing the footprint of a circuit. Additionally, InP is completely incompatible with CMOS fabs.

**Silicon** is the material platform that borrows the most from the electronics industry, and is therefore the easiest material platform for scaling to large volumes: The

defect rate is low, and 300 mm wafers are available, providing an increase in production efficiency. On top of that, it very compatible with the CMOS process, since it uses the exact same materials. Performance of the waveguides is also good, with low propagation losses and the tightest bend radii of the three discussed platforms, providing the possibility of integrating many components in a single circuit. The largest drawback of the silicon photonics platform is that light sources cannot be fabricated in the silicon itself, meaning that extra work needs to be done for the integration of the light source. Photodetectors can be implemented in the silicon itself [14].

**Silicon nitride** is a platform in a similar position as the silicon platform. It has the lowest propagation losses of all three platforms discussed, but has larger bend radii compared to the silicon platform. Silicon nitride is a CMOS compatible material, though the thick layers of SiN necessary provide unique challenges [15]. Just as with the silicon platform, light sources cannot be made in the SiN directly, requiring extra steps for the light source integration. In SiN, photodetectors cannot be implemented in the material itself.

	InP	Si	SiN
Passive components	+	++	+++
Lasers	+++	0	0
Modulators	+++	++	+
Switches	+++	+++	+
Optical Amplifiers	+++	0	0
Photodetectors	+++	+++	0
Footprint	++	+++	+
CMOS compatibility	-	++	+

*Table 1.1: Summary of the properties of the three main photonic platforms, adapted from [16]*

## 1.2 Light generation for silicon (nitride) PICs

Since silicon and silicon nitride cannot be used to make light sources, a second material system is necessary to generate light. The material of choice for this is III/V semiconductor compounds, like InP, GaAs, or GaSb. By choosing the right materials, a wide range of wavelengths can be generated, ranging down to at least 450 nm [17], and up to at least 3.2  $\mu\text{m}$  [18]

There are two main options to introduce a light source to the circuits in the silicon

(nitride) platform. The light source and the PIC can both be separately manufactured and integrated together afterwards, or a different material system can be introduced into the platform during the fabrication of the circuit. The first method is called hybrid integration, while the second one is called heterogeneous integration. Both of these methods can be used to integrate a complete laser fabricated in the second material system, or make a hybrid laser where part of the laser cavity is defined in the Si(N) PIC, and the second material is only used as a gain section. One example of hybrid integration (butt-coupling) and one of a heterogeneously integrated laser are shown in Fig. 1.1. Note the main difference: the hybrid integrated laser uses two separate dies, while the heterogeneously integrated laser consists of one die.

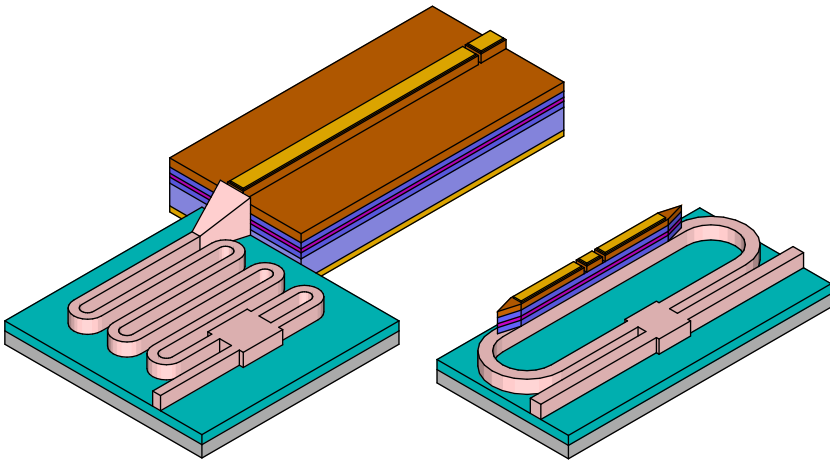


Figure 1.1: Diagram of a hybrid integrated ECMLL (left) and a heterogeneously integrated ECMLL (right). Note the difference in the number of dies.

### 1.2.1 Hybrid integration

Hybrid integration of the light source with a PIC comes in a few forms:

**Fiber coupling** is the least integrated variant. With this approach, the PIC and the light source are fabricated and packaged independently and connected with an optical fiber. This is the only method where both chips don't affect each other thermally [19]. However, it is the bulkiest approach to hybrid integration.

**Photonic wire bonding** is an approach where both chips are brought close to each other. Both chips are fabricated individually, and mounted to the same submount. Both chips are then covered with a photosensitive polymer from which the photonic wire bonds will be made. Using computer vision techniques the exact location

of the individual components is measured. These measurements are then used to calculate the optimal 3D shape of the photonic wire bond waveguides. These shapes are then written into the polymer using direct write Two-Photon Polymerization (TPP) lithography. After this step, the photonic wire bond is cladded using a second polymer with a lower index, both for mechanical support and for the optical waveguiding [20].

The chips can be placed much closer together using photonic wire bonding compared to fiber coupling, leading to a smaller end result. Thermal coupling between both chips is increased though, since both are mounted to the same submount, meaning both chips have to work at the same temperature.

Machines and processes for photonic wire-bonding are now commercially offered by at least one company: Vanguard Automation in Karlsruhe, Germany.

**Butt-coupling**, the technique used in this work, brings the two chips even closer together so two facets touch. Both chips have one or more waveguides ending at the touching facet, and by precise alignment, the two waveguides can be coupled together with little loss. If they are then glued they can be packaged together afterwards.

In a research environment, butt-coupling can be done temporarily using a precise alignment setup without gluing the chips together. Commercially, it is now offered as part of the packaging process by at least one company: PhiX in Enschede, the Netherlands [21].

**Flip-chip integration** makes use of a specially designed PIC, where a recess is made with an exact depth and contacts for solder bumps [22]. A waveguide runs up to the recess where a second die will be placed upside down (since the waveguide is on top), aligning to the waveguide and the solder bumps to make an electrical and an optical connection. This is the most compact solution of the hybrid integration methods, but a special recess etch step needs to be added to the PIC process, with tight tolerances for the etch depth. Additionally, the thermal coupling between both chips is the highest of the hybrid integration methods since the second material is right on top of the first.

## 1.2.2 Heterogeneous integration

When the gain material is introduced to the PIC material early in the fabrication process, before the Back End Of Line (BEOL), it is called heterogeneous integration. Compared to all the hybrid integration approaches, heterogeneous integration is more suited for mass fabrication due to the possible parallelism in the fabrication process. The integration can be done for many devices on a wafer at once, versus

one by one for hybrid integration methods. Because of this, all heterogeneous integration methods apply the secondary material on top of the first.

**Wafer bonding** is a method in which complete and unprocessed wafers of the secondary material are bonded on top of the PIC material. This does not require precise alignment in the bonding step since the secondary material will only be patterned and etched after the bonding, providing accurate alignment to the underlying circuit using standard cleanroom tools. Wafer bonding is however quite wasteful since most PICs don't need the secondary material everywhere, but only at places in the circuit where a light source has to be. Secondly, the wafer sizes of the suitable gain materials are smaller than those of Silicon, leading to a loss of a large part of the silicon wafer where the secondary wafer does not reach.

**Die to wafer bonding** solves the problem of wasting secondary material by bonding separate dies instead of full wafers, to only the locations where the die is necessary. The die is not processed beforehand, and therefore the alignment during the bonding step is not critical.

**Micro-transfer printing** is a technique that has similarities to both flip-chip integration and die-to-wafer bonding. In this case, the primary and secondary materials are both processed individually on a wafer scale. Afterwards, a transfer printing tool can pick up many dies of the secondary material at once and print them onto the primary circuit. Since both wafers have been patterned already this printing step does need to have very accurate alignment.

### 1.3 Optical frequency combs

Another important Nobel Prize in the field of photonics was awarded in 2005, when John L. Hall and Theodor W. Hänsch were both awarded a quarter of the prize “*for their contributions to the development of laser-based precision spectroscopy, including the optical frequency comb technique*” [23].

While normal laser sources emit only a single wavelength of light or multiple wavelengths where each individual laser line is not correlated to the others, optical frequency comb spectra contain laser lines of many wavelengths, where there is a fixed phase relation between all these lines. On the optical frequency spectrum there is a very simple relationship between all the lines [3]:

$$f_n = n f_{\text{rep}} + f_{\text{CEO}}$$

All three of these frequencies are labeled in Fig. 1.2. In this case,  $f_n$  refers to the optical frequency of each line, with line number  $n$ , which is impossible to directly

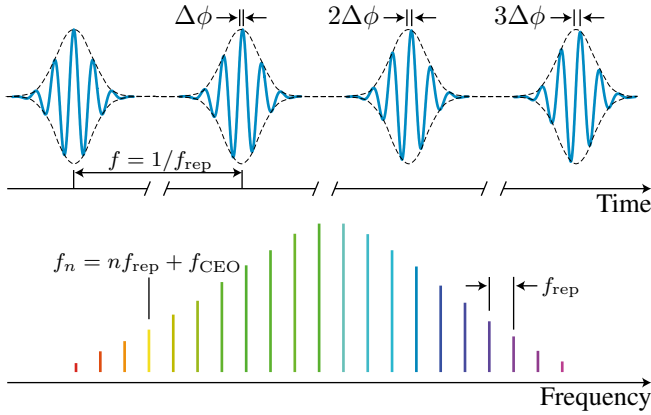


Figure 1.2: Schematic representation of a frequency comb in both the time domain and the frequency domain. Figure from [3]

measure with high precision.  $f_{\text{rep}}$  and  $f_{\text{CEO}}$  refer to the repetition rate frequency and carrier-envelope offset frequency respectively which both have frequencies in the RF domain.  $f_{\text{rep}}$  is very simple to measure in comb spectra. When taking the inverse Fourier transform of the frequency comb spectrum, the amplitude will be periodic in time, with a period given by  $1/f_{\text{rep}}$ . Therefore, the repetition rate frequency can be directly measured by shining the light onto a fast enough photodiode and measuring the electrical frequency at the output.

The carrier-envelope offset frequency cannot be measured from the spectrum directly, but once it is measured, the exact optical frequency of each individual line can be deduced from the simple equation. The Nobel Prize was awarded for the work that enabled this measurement. The fundamental idea behind measuring  $f_{\text{CEO}}$  relies on having a fixed relationship between two laser lines at significantly different frequencies through a nonlinear process. These two laser lines can then be compared to two separate comb lines that are far apart. The different frequency offsets at both sides of the comb can then be used to infer  $f_{\text{CEO}}$ . The first demonstration of this was done at the Max Planck Institute of Quantum Optics, Theodor Hänsch' lab, using an earlier idea of a frequency divider chain [24]. In this case, two comb lines were compared where the ratio between line numbers  $n_1$  and  $n_2$  was 7 : 8, which required a comb bandwidth that could be reached using the output of a Ti:Sapphire fs mode-locked laser that was spectrally broadened in a nonlinear fiber. This measurement setup was very complicated though.

Soon after, the measurement of  $f_{\text{CEO}}$  was made significantly simpler by work in John Hall's lab at the Joint Institute for Laboratory Astrophysics, where a much simpler measurement scheme was used [25]. By using a different nonlinear fiber,

the spectrum of a Ti:Sapphire laser could be broadened to span more than an octave, making it possible to use a self-referenced  $f$ - $2f$  technique, schematically shown in Fig. 1.3. In this case, a low-frequency comb line is filtered out and frequency doubled, and then compared to a high-frequency comb line. The first line  $n_1$  is at  $n_1 f_{\text{rep}} + f_{\text{CEO}}$  before the frequency doubling, and therefore at  $2n_1 f_{\text{rep}} + 2f_{\text{CEO}}$  after doubling. If the second line  $n_2$  is chosen at twice the line number of  $n_1$ , its frequency will be  $n_2 f_{\text{rep}} + f_{\text{CEO}} = 2n_1 f_{\text{rep}} + f_{\text{CEO}}$ , meaning there's a frequency difference between both lines of  $1f_{\text{CEO}}$ , which can be directly measured as a beat note.

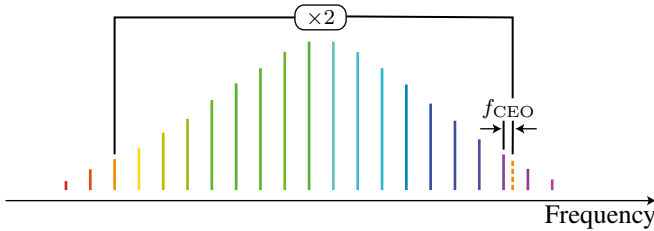


Figure 1.3: Schematic representation of  $f$ - $2f$  referencing of a frequency comb, which can be applied to measure  $f_{\text{CEO}}$  in octave-spanning frequency combs. The  $\times 2$  block represents second harmonic generation.

### 1.3.1 Applications of frequency combs

One of the important applications where it is useful to know the exact frequency of light is precision spectroscopy, which can be used to advance fundamental research. Additionally, it could be used in the future for optical clocks that are more accurate than the atomic clocks used nowadays. In this case, a transition in an atom would be probed with a much higher frequency than the transition used in the current cesium clocks. [26]

Spectroscopy can benefit from another property of frequency combs when two of them are used together to do Dual Comb Spectroscopy (DCS). When the repetition rate of both frequency combs is slightly different, the interference between both combs measured using a photodiode will be another frequency comb, consisting of RF frequencies. Each line in this comb will correspond to the beating of 2 optical lines close together at a certain wavelength. This means that if frequency comb 1 is passed through a sample, the optical transmission spectrum of it is sampled by the lines of comb 1. If it is then interfered with comb 2 on a photodiode, the RF output of the photodiode contains the same information captured by comb 1. This means that no scanning of the laser is necessary, as is the case with conventional spectroscopy

techniques [27], and only the electrical output signal from the photodiode has to be measured.

There are other applications of frequency combs where exact knowledge of  $f_{\text{CEO}}$  is not necessary. Telecom is one example, where a single frequency comb can be used to replace several CW laser sources in a Wavelength Division Multiplexing (WDM) transmitter [28]. Another important example is (dual frequency comb) LIDAR, which could be used in autonomous cars [1]. Both of these applications can only be enabled when the frequency comb source can be made physically small enough and robust enough for use in a moving vehicle or at data center temperatures. Additionally, they have to be able to be made in large enough volumes for a low enough price before these applications would be economically viable to implement. To fulfill all these requirements, a fully integrated comb generator is a very promising possibility. Three types of integrated optical frequency comb sources have been demonstrated today, which are listed below.

### 1.3.2 Kerr combs

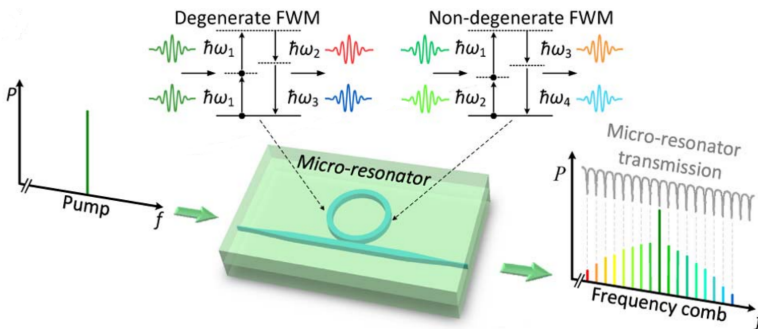


Figure 1.4: Schematic of Kerr comb generation. From [29]

Kerr combs are generated in a microresonator, using nonlinear optical effects. It is schematically shown in Fig. 1.4. The microresonator is pumped with a continuous wave single frequency laser source, where some of the pump light is converted to different frequencies through (degenerate) four-wave mixing. The frequency spacing will be given by (an integer multiple of) the Free Spectral Range (FSR) of the microresonator, and the exact shape and bandwidth of the comb are controlled by the dispersion in the microresonator. An advantage of Kerr combs is that the process is easily described theoretically using the Lugiato-Lefever equation [30], which makes it possible to predict the spectrum generated by a system with a high precision before actually fabricating it.

Fundamentally, Kerr comb generation becomes more difficult for decreasing repetition rates because the threshold power for the comb generation is inversely proportional to the repetition rate [31]. Therefore Kerr combs are best suited to applications where narrow line spacing is not necessary.

For a long time, all demonstrated integrated Kerr combs used a microresonator on a chip that was pumped with an off-chip laser that was coupled using a fiber. Recently, systems have been demonstrated where the pump source was integrated onto the chip, either using butt-coupling [32] or heterogeneous integration using bonding [33]. These systems had line spacings of 43.35 and 100 GHz respectively.

### 1.3.3 Electro-optic combs

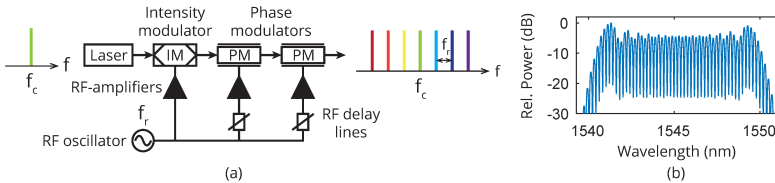


Figure 1.5: Schematic of EO comb generation. From [34]

Electro-Optic (EO) combs are generated by actively modulating a single-frequency pump laser, which generates sidebands in the spectrum. If the modulator is placed inside a resonator and driven at an integer multiple of cavity's FSR, the sideband generation will cascade, generating a broad spectrum. As with Kerr combs, the resonator's dispersion has a significant effect on the bandwidth that can be achieved [35].

The requirement of active modulation can be a disadvantage, since it requires complex driving electronics, increasing the size and cost of a working device. On the other hand, if the device does not make use of the resonant cavity it can be an advantage as well: Using active modulation means that the repetition rate can be freely varied, limited only by the driving electronics and the modulator bandwidth. In a resonant configuration, the repetition rate can still be changed, but only to integer multiples of the resonator's FSR.

Electro-optic combs using an integrated light source have already been demonstrated in monolithic III/V platforms with 4 to 8 GHz line spacing [36, 37]. Systems combining III/V and lithium niobate have also been demonstrated: Using heterogeneous integration, a 19 GHz repetition rate was demonstrated [38], and 10 GHz was achieved using hybrid integration [39].

### 1.3.4 Mode-locked lasers

Mode-Locked Lasers (MLLs) are the third demonstrated way to generate frequency combs in an integrated platform, and are the subject of the rest of this thesis. Different from Kerr combs and EO combs, the MLL does not require an external laser, since it is the laser. This means the complexity of a system can go down by using an MLL over a Kerr comb or EO comb.

The repetition rate of a mode-locked laser can only be at an integer multiple of the laser cavity's FSR, but in contrast to Kerr combs the FSR of the cavity can be decreased without a significant penalty to the efficiency of the comb generation. When low-loss cavities are used, the addition of extra cavity length will only come with a small increase in cavity loss, which increases the threshold current and decreases the slope efficiency of the laser slightly. Therefore, mode-locked lasers are preferred over Kerr combs for low repetition rate comb generation.

Many integrated MLLs have been demonstrated so far, mostly in monolithic platforms, but the recent trend is towards lower repetition rates, requiring hybrid or heterogeneous integration. Using hybrid integration, a repetition rate of 360 MHz has been achieved in a self-mode-locked laser [4]. Using a more conventional MLL architecture with Amplitude Modulation (AM) mode-locking, a hybrid integrated MLL has reached a repetition rate of 2.18 GHz (presented in this work). Using heterogeneous integration, a repetition rate of 930 MHz has been demonstrated with a laser made using a bonding technique [40] and 755 MHz has been achieved using transfer printing [41].

## 1.4 Research objectives

The primary aim of this research was to use hybrid integration to demonstrate a mode-locked laser with an external cavity made in SiN and measure its performance. In order to be competitive against Kerr combs, low repetition rates ( $< 5$  GHz) will be targeted. Additionally, it was planned to stabilize the comb output of one of these lasers as much as possible, to make it usable in dual-comb spectroscopy experiments.. Once this was achieved, it was planned to attempt to use these lasers for (dual comb) spectroscopy experiments in the lab of the Max Planck Institute of Quantum Optics. Unfortunately, the available time in this project ran out soon after the injection-locking stabilization of one of these lasers. Therefore, no spectroscopy experiments have been performed.

## 1.5 Thesis outline

This thesis contains five chapters. In chapter 2 it starts with a theoretical overview of how semiconductor mode-locked lasers work, and what factors have an impact on the noise characteristics of these lasers. Chapter 3 is about the design and fabrication of hybrid integrated mode-locked lasers using an external cavity in a SiN platform. The largest portion of the chapter is about the design and fabrication of the SiN external cavity chip, which was done in the cleanroom facilities of Ghent University as part of this work. Another portion is devoted to describing several gain chips used for experiments, as well as attempts at post-processing gain chips that were acquired from external companies to add a saturable absorber. Chapter 4 is about the characterization of three different lasers that were made. Two of them showed good mode-locking performance, but one of them would not exhibit mode-locking. In chapter 5 conclusions are drawn from this research work and an outlook is given of future work that could be performed on this topic.

## 1.6 List of publications

This dissertation has led to the following list of publications in international peer-reviewed journals and conferences.

### 1.6.1 Publications in international journals

1. **E. Vissers**, S. Poelman, C. Op de Beeck, K. Van Gasse, B. Kuyken, “Hybrid integrated mode-locked laser diodes with a silicon nitride extended cavity”, *Optics Express*, vol. 29, no. 10, pp. 15013–15022, 2021
2. **E. Vissers**, S. Poelman, H. Wenzel, H. Christopher, K. Van Gasse, A. Knigge, B. Kuyken, “Hybrid integrated mode-locked laser using a GaAs-based 1064 nm gain chip and a SiN external cavity”, *Optics Express*, vol. 30, no. 23, pp. 42394–42405, 2022

### 1.6.2 Publications in international conferences

1. **E. Vissers**, S. Poelman, K. Van Gasse, B. Kuyken, “Hybrid-integrated extended cavity mode-locked laser using SiN and a generic III/V platform”, *The European Conference on Lasers and Electro-Optics 2021*, Munich, Germany, 21–25 June 2021

- 
2. D. Maes, L.N Reis, S. Poelman, **E. Vissers**, V. Avramovic, G. Roelkens, S. Lemey, E. Peytavit, B. Kuyken, “High-Speed Photodiodes on Silicon Nitride with a Bandwidth beyond 100 GHz”, *Conference on Lasers and Electro-Optics 2022*, San Jose, United States of America, 15-20 May 2022



# 2

## Extended cavity mode-locked lasers

---

<b>2.1</b>	<b>Introduction to lasers</b>	<b>15</b>
2.1.1	Gain media	16
2.1.2	Semiconductor optical amplifier	17
<b>2.2</b>	<b>Mode-locked lasers</b>	<b>20</b>
2.2.1	Active mode-locking	20
2.2.2	Saturable absorption	21
2.2.3	Stable mode-locking points	22
2.2.4	Integrated MLL architectures	25
2.2.5	Self mode-locked lasers	26
<b>2.3</b>	<b>External cavity MLLs</b>	<b>26</b>
2.3.1	Laser noise	26
2.3.2	Evolution of integrated MLLs	30
2.3.3	Applicability of hybrid integrated ECMLLs	32

---

### 2.1 Introduction to lasers

A laser is a conceptually very simple device, with two main components: the laser cavity and the gain medium inside the cavity. Light will travel around the cavity, experiencing some optical losses. When the gain medium can provide more optical

gain compared to the optical losses inside the laser cavity, the amount of light inside the cavity will increase. The increased amount of light will decrease the effective amplification of the gain medium, which will cause the system to reach a steady state.

The losses in the laser cavity are caused by two things: the undesired imperfections in the laser cavity, and the desired out-coupling of the laser light leading to a loss in the cavity, but also to the useful light output of a laser.

The gain medium is a material that takes energy from an external source and releases this energy in the form of photons inside the laser cavity through stimulated emission. In this case, a photon is emitted into the laser cavity with the same phase and wavelength as a photon that was already present in the laser cavity.

### 2.1.1 Gain media

There are many different gain media that can be used to make a laser, but fundamentally they have the same working principle. The medium has several discrete energy levels where carriers can exist, and several physical processes can transition carriers between energy states. Some of these processes absorb or emit a photon. A four-level system is close to the ideal laser, and can be seen on the left in Fig. 2.1. Four transitions are important in this case: The pump transition absorbs either a high-energy photon or electrical energy to transition a carrier from the ground state to energy state 3 in the system, which has the highest energy. The lifetime in this state is short, and therefore the carrier will spontaneously transition to energy state 2. From here, the carrier can transition to state 1 in two ways, either through stimulated emission (solid arrow) or through spontaneous emission (dotted arrow). This transition from state 2 to 1 (or vice versa) is also called the laser transition. The lifetime in state 1 should ideally also be low, so the carrier transitions from state 1 to the ground state almost immediately.

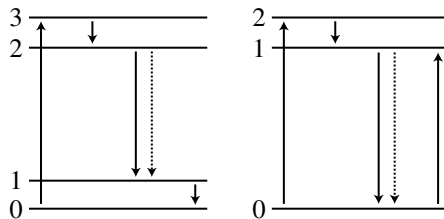


Figure 2.1: Energy levels in a four-level system (left) and a three-level system (right), with the important energy level transitions indicated with arrows.

Due to the short lifetime of energy state 1, the population in this state will be

negligible during continuous wave operation. This means that photon absorption cannot happen at the laser transition, since there are no carriers at energy level 1 to be raised to level 2 through absorption. This effect is different in a three-level system.

In a three-level system, the intermediate energy state 1 does not exist, leaving the system with three transitions as shown on the right in 2.1. This has the disadvantage that the lower energy state of the laser transition will not always be almost empty, and therefore absorption can also happen at the laser transition, where a photon is taken out of the cavity to excite a carrier from the ground state to energy level 1, as shown by the rightmost arrow in Fig. 2.1.

## 2.1.2 Semiconductor optical amplifier

Semiconductors can also act as gain media. Since they can be fabricated using the same kinds of processes as photonic integrated circuits, they are a very suitable option for integrated photonic systems.

### Band structure

In the case of semiconductors, electron-hole pairs in the material represent a higher energy state, which relaxes to the ground state when the electron and hole recombine. This recombination can happen radiatively or non-radiatively, where the radiative recombination will produce a photon, while non-radiative recombination will produce heat. Radiative recombination can happen as either spontaneous emission or stimulated emission, where stimulated emission is the responsible process for lasing to occur.

The energy states in a semiconductor are more complicated than in a simple three- or four-level system. Since electrons and holes are particles, they have a momentum  $p$  and a mass  $m$ . In a vacuum, this would mean that their energy can be calculated using  $E = \frac{P^2}{2m}$ . Once these electrons are present in the semiconductor material though, this energy-momentum relationship changes significantly. The relationship in a certain material is shown in the material's band structure diagram. The band structure diagrams for InP and Si are shown in Fig. 2.2. These band structures plot the relationship between momentum (x-axis) and energy (y-axis) for the electrons and holes in the material. The x-axis signifies certain directions for the momentum along the crystal plane. What the x-axis signifies is actually a three-dimensional momentum vector, which is very hard to visualize. The directions that are chosen for band structure plots capture the minima and maxima of the relationship.

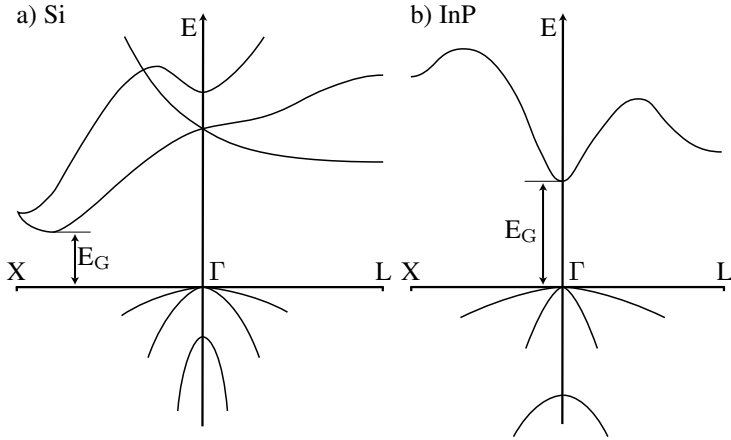


Figure 2.2: Schematic of the band structure of a) silicon and b) indium phosphide. The bandgap is indicated for both of them. Adapted from [42, 43].

An important material property that can be read from the band structure diagram is the band gap energy, which specifies the height of the energy region where no holes or electrons can exist, irrespective of their momentum. This means any absorption or emission can only happen for photon energies that are greater than the band gap energy. All energy levels above the bandgap energy are part of the conduction band, where excited electrons can exist. The energy levels below the bandgap are part of the valence band, where holes can exist. Excited electrons will thermally redistribute to fill up the lowest energy states in the conduction band first, while holes will redistribute to fill up the highest energy states in the valence band [44].

A photon can be absorbed or emitted only when both energy and momentum are conserved. The momentum of a photon is negligible compared to the momentum of an electron, therefore a transition can efficiently occur vertically in a band structure plot. If an excited electron can transition straight down in the band structure diagram to recombine with a hole, a photon can be emitted without changing the momentum of the electron. Radiative transitions between states with different momentums are possible, but this requires the emission of a phonon as well. This decreases the efficiency of the process [44].

This efficiency difference between transitions with or without phonon emissions is what makes the distinction between direct and indirect band gap materials important. A material has a direct band gap when the highest point of the valence band and the lowest point of the conduction band have the same momentum, like in InP. With an indirect band gap material, these points have different momentums, like in Si.

Light generation in an indirect band gap material is very inefficient, since after

redistribution of the carriers the electrons in the conduction band do not ‘see’ any holes with the same momentum. Therefore, a phonon is necessary for every transition, which makes the process inefficient. In a direct band gap material, the redistribution will bring the available states to the same momentum, increasing the efficiency of radiative redistribution. This is also the reason why Si platforms need another material to enable light source integration.

### Electron injection/extraction

In order to amplify light, the excited electrons need to be at the same location as the light, in order to interact with the photons. This can be done by using a second semiconductor material with a larger band gap and sandwiching the smaller bandgap material in between. This structure is called a heterostructure. When electrons and holes are injected through the high band gap materials, they will be trapped in the material with the lower band gap. If the light is also guided through this region, the stimulated emission can happen.

In order to inject electrons and holes efficiently, positive and negative doping can be added to the higher bandgap layers of the heterostructure, to add electrons or holes. The energy levels as a function of position then look like in Fig. 2.3. When a current is sent from left to right through this device (forward biased), the only way for this current to flow is through recombination events between electrons and holes in the place where they overlap, which is in the low band gap material. [44]

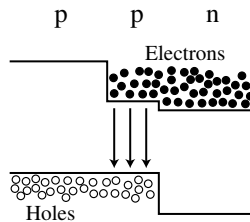


Figure 2.3: Schematic view of carrier injection in doped heterostructures. The left and middle sections are p-doped, and the right section is n-doped. A current flows from left to right in this image (negatively charged electrons from right to left). Adapted from [44].

### Quantum well amplifiers

The amplifiers described above are so-called bulk SOAs. In these amplifiers, the layer of material where the electrons can be excited is relatively large ( $>100$  nm), which means they are free to move. When the thickness of the layer is reduced,

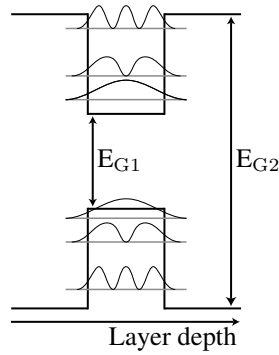


Figure 2.4: Schematic representation of the allowed confined wavefunctions of electrons and holes in a quantum well structure. The wavefunctions are drawn in black on top of their energy level in grey.

the position of the excited electrons and holes becomes confined, and the structure becomes a quantum well. Amplifiers made using quantum wells offer wider optical bandwidth and higher saturation output power compared to bulk SOAs [45]. Calculating the allowed wavefunctions of electrons and holes in a quantum well structure leads to the formation of several confined states, where the allowed electron states come with additional confinement energy. The same thing happens for holes, but the confinement energy is negative. This means the effective bandgap in the material is increased, and therefore also the emitted light is of a higher energy [44].

## 2.2 Mode-locked lasers

A Mode-Locked Laser (MLL) is a laser that emits a frequency comb at the output. A mode-locked laser can be made from a laser that supports many longitudinal resonator modes, by including a mechanism that can lock the phase of these resonating modes to each other. Depending on this mechanism, MLLs can be divided into three categories: active mode-locking, passive mode-locking or self-mode-locking lasers, as described in the following sections.

### 2.2.1 Active mode-locking

When a laser line is actively amplitude or frequency modulated inside the laser cavity, sidebands will be created next to the laser line with an offset frequency equal

to the modulation frequency. These sidebands carry phase information of both the laser line and the modulation signal. If the laser resonator supports multi-mode lasing, and the modulation frequency is equal to the laser mode-spacing, this means that the generated sidebands will overlap with another laser line. This will cause the two laser lines to couple to each other, and start oscillating with a fixed phase relationship [46].

If the amplitude modulator has a broad optical bandwidth, this sideband modulation will happen for several laser modes at once, each with the same offset frequency. This turns the laser output into a frequency comb, where each laser line's frequency is given by  $f_n = n f_{\text{rep}} + f_{\text{CEO}}$ . The laser output is now mode-locked since the cavity modes are now phase-locked together. Such mode-locking can be achieved using many types of actively driven modulators [46, 47].

## 2.2.2 Saturable absorption

Mode-locking can also be achieved without an actively driven modulator inside the cavity by making use of a Saturable Absorber (SA). An SA is a nonlinear component where the amount of absorption is a function of the light intensity: the absorption decreases for higher optical powers. If the phases of a few laser lines randomly line up to cause a slight spike of the output power in the time domain, the SA temporarily drops in absorption. This means that the laser lines experience less loss when they have that phase relative to each other. Therefore, operation in this state is preferred over other modes, and the random drifting of the phase is pushed towards that state. If the chromatic dispersion relation in the cavity is correct, the lines can stay in phase for subsequent roundtrips, and all modes will then be phase-locked together and form a pulse train, causing the most amount of saturation in the SA, and therefore the lowest amount of loss in the cavity.

Conveniently, SOAs can be used as SAs as well. At any moment, the net gain (ignoring spontaneous emission) of an SOA is proportional to  $N_1 - N_0$  where  $N_1$  is the number of excited electrons, and  $N_0$  amount of electrons in the ground state. If  $N_1$  is lower than  $N_0$ , this means the SOA will absorb more photons than it emits. By applying a reverse bias to the junction, electrons excited by absorbing a photon will be taken out of the conduction band by the external voltage to deplete  $N_1$ , to return to the valence band without emitting a new photon. However, if the rate of photon absorption is higher than the rate of electron removal from the conduction band, the ratio  $N_1 - N_0$  will become less negative, decreasing the net loss of the SA until the excited electrons have been returned to the conduction band.

Often, exactly the same material is used for the SA as for the SOA in an MLL. This causes the gain and absorption spectra to be similar in wavelength, but there

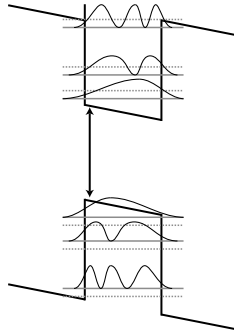


*Figure 2.5: The Quantum Confined Stark Effect (QCSE), showing the electron and hole wavefunctions when a bias is applied to a quantum well. The dashed gray lines show the energy levels when no bias is applied, the solid gray lines show the energy levels with the bias applied.*

are some differences between the gain and absorption spectra. In a quantum well SOA that's reverse biased, the energy levels of the electrons and holes get closer together, since the tilted potential leads to different conditions, and therefore different wavefunctions and energy levels. It is schematically shown in Fig. 2.5. The higher the reverse bias, the higher the shift in energy levels. Another factor that comes into account from the different added bias is that the wavefunction overlap between the electrons and the hole states is also decreased because the wavefunctions both shift to the opposite direction of the quantum well. Therefore, the peak absorption wavelength of the absorber increases for a higher bias, while the peak absorbance decreases for a higher bias. Additionally, the absorption spectrum is more prominent on the red side of the spectrum compared to the blue side when compared to the gain spectrum, due to the exciton absorption [48].

### 2.2.3 Stable mode-locking points

Having the required components in a laser cavity is not enough for passive mode-locking to occur, the operating parameters also need to be correct for this to happen. For stable mode-locking to happen, a stable solution should exist where the laser pulse has the exact same shape after one roundtrip in the laser cavity, both in the time domain and in the frequency domain. A lot of work has been done to describe the pulses formed in passively mode-locked lasers, where the Haus Master Equation is very influential. This equation is a differential equation describing the changes to a pulse shape as a function of at least roundtrip gain and loss, and saturable absorber/active modulator loss. The equation taking into account the

time-dependent laser gain  $A$ , the time-dependent absorber loss  $B$ , second-order dispersion, resonator loss, and time-dependent loss is given by [49]:

$$\delta T \frac{dv}{dt} = -\frac{\omega_0}{2Q} T_R \left( 1 - \frac{1}{\omega_C^2} \frac{d^2}{dt^2} - \left( \frac{2A(t)Q}{\omega_0 T_R} \right) + \left( \frac{2B(t)Q}{\omega_0 T_R} \right) \right) v$$

In this equation,  $\delta T$  is the pulse time delay/advance relative to the roundtrip time in the cavity caused by the uneven absorption of different parts of the pulse,  $v$  is the pulse envelope shape,  $Q$  is the quality factor of the optical resonator,  $\omega_0$  is the optical center frequency,  $\omega_C$  the width of the bandwidth limiting filter, and  $T_R$  the roundtrip time in the cavity.

Herman Haus published solutions to these equations describing the pulse shapes and the necessary conditions to achieve these in actively mode-locked lasers [50], and passively mode-locked lasers with a fast [51] and slow [49] saturable absorber. The difference between a fast and slow saturable absorber is in the relaxation time of the absorber. A fast absorber has a relaxation time faster than the pulse width, while the slow saturable absorber relaxes slowly relative to the pulse width. For semiconductor mode-locked lasers, since the carrier lifetime in the upper state of the gain medium is typically on the order of nanoseconds [52], but the typical pulse widths on the order of picoseconds [53] The reverse bias across the SOA used as an SA does decrease the lifetime below that of a forward biased SOA, but still not towards the ps timescale, which is the order of magnitude of the pulse widths measured in typical semiconductor MLLs.

In simple cases, the Haus Master equations work very well, but solving them is outside of the scope of this thesis. Unfortunately, parasitic effects in semiconductor amplifiers and SAs limit the usefulness of these equations for the case of semiconductor MLLs, since many complicated effects happening in the SOAs need to be taken into consideration, increasing the difficulty of finding analytical solutions. Additionally, extracting the parameters necessary to solve these simulations is a difficult task in semiconductor lasers.. However, the work still gives an insight into the effects that are important for mode-locking to occur.

In the time domain, a stable solution could work as follows: A pulse is relatively broad before entering the SA section of the MLL. The SA absorbs the leading edge of the pulse before it saturates, the rest of the pulse travels through the SA with less loss. The pulse then enters the gain section, where mostly the middle of the pulse is amplified. This amplification of the pulse peak will reduce the number of excited carriers, and therefore also the amount of gain for the trailing edge of the laser, an effect called gain saturation.. Therefore, after passing through the SA and the gain section, the pulse will have become more narrow, since the leading and trailing edges of the pulse have been amplified less than the middle part. because of the cavity dispersion, this narrow pulse will broaden again, and in a stable solution will

have the same shape it had at the start when it reaches the SA for the second time. Additionally, since the front part of the pulse was absorbed, the pulse is slightly delayed compared to the roundtrip of the cavity, meaning the repetition rate will be very slightly lower than the fundamental cavity FSR. Additionally, this slight delay means that even if there's a net positive gain window behind the pulse, any noise that starts in this window has a finite time to be amplified and overpower the initial pulse before the pulse itself covers up that noise [54]

In order for a stable solution like this to exist, the combination of driving parameters for the MLL needs to be correct. There are three main driving parameters at play, the gain section current, the SA bias, and the laser temperature.

Tuning the gain current has a large impact on the optical power inside the cavity, which plays a big role in the saturation of both the gain section and the SA. Additionally, it alters the rate at which saturated gain is restored. Lastly, due to carrier injection and temperature effects, it also changes the spectral shape of the gain.

Tuning the SA bias has an impact on the strength and the spectral shape of the absorption effect. In quantum well structures, the absorption profile will decrease and red-shift for higher reverse biases, because of the Quantum Confined Stark Effect (QCSE). Additionally, a higher reverse bias decreases the restoration time after the SA saturates, since generated energy-hole pairs will be extracted from the structure faster due to the stronger electric field across the SA.

Tuning the temperature of the laser has an impact on the gain and absorption spectrum of the gain section and the SA. This can make a difference for if the right wavelength ranges of these spectra overlap.

### **Stable points in semiconductor MLLs**

It is difficult to predict the driving parameters that will lead to stable mode-locking in fabricated devices, especially in semiconductor MLLs. Therefore, sweeping the driving parameters to find mode-locking points after fabrication is what is typically done. This method was also used to find the operating points of the lasers characterized in this thesis. These operating points can be visualized in a mode-locking map, where a parameter of the output spectrum (usually output power or peak RF power) is plotted in a colormap as a function of gain current and SA bias. If there is a high RF power at the fundamental cavity repetition rate or a multiple thereof, this shows that mode-locking has likely occurred. Often, the mode-locking can also be seen if the laser is connected to an OSA since the spectrum in the mode-locked state will be very stable over time, and show a smooth envelope.

## 2.2.4 Integrated MLL architectures

Mode-locked lasers with one Saturable Absorber (SA) can have several architectures, schematically shown in Fig. 2.6. The resonator can either be a linear Fabry-Perot style resonator or a ring type. For the Fabry-Perot style, a further subdivision can be made between a Colliding Pulse Mode-locked Laser (CPML), Self-Colliding Pulse Mode-locked Laser (SCPML), and an Anti-Colliding Pulse Mode-locked Laser (ACPML) [55]. For the ring type MLL, a Colliding Pulse Mode-locked Laser (CPML) architecture can be used, which is similar to the CPML scheme, except that the mirrors are replaced with a connection between both sides, and the light will be outcoupled from the cavity using a tap inside the ring. If an optical isolator is incorporated in the cavity, a unidirectional mode-locked laser can also be realized, where no pulse collision happens in the SA. Due to the immaturity of integrated optical isolators, such a unidirectional ring MLL has not been demonstrated yet in integrated platforms, while CPML ring lasers have been demonstrated [56].

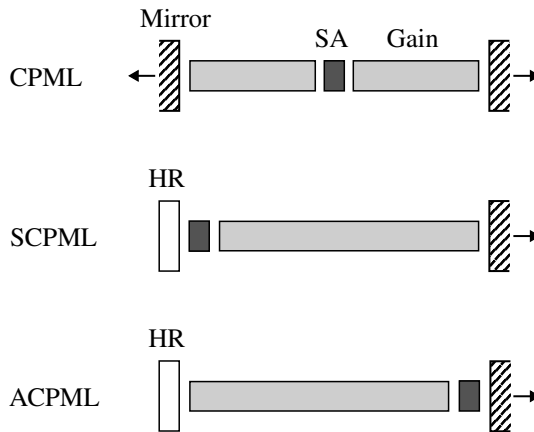


Figure 2.6: Three Fabry-Perot MLL architectures, where the differences are in the positioning of the SA in the cavity relative to the mirrors.

The difference between the Fabry-Pérot type architectures is where the SA is placed in the resonator. The CPML scheme places the SA in the center of a completely symmetrical cavity. This would cause two pulses to propagate through the cavity at once (departing in both directions from the SA), which would pass the SA at the same time, thereby increasing the instantaneous power in the SA, and saturating it more quickly. For the gain sections, only the intensity of one pulse is present at a time, reducing the amount of gain saturation experienced. The CPML scheme is very sensitive to a mismatch between both sides of the laser cavity, and the pulse repetition rate is also twice the FSR of the cavity, due to the two pulses in

the cavity. To get around these characteristics, the SCPML scheme was proposed, where the SA was placed near the High Reflectivity (HR) mirror. This causes only a single pulse to propagate in the cavity, which would pass the SA twice in quick succession, colliding with itself inside the SA after the reflection. From this scheme, an alteration was proposed to go to the ACPML scheme, where the SA is placed at the outcoupling mirror, thereby reducing the intensity of the light before the second pass through the SA, and reducing the amount of pulse-collision.

There are also Mode-Locked Laser (MLL) architectures with several SAs. These are used when a higher pulse repetition rate than the fundamental cavity FSR is desired. By dividing the cavity into sections with equal optical length, separated by individual SA sections, several pulses will form in the cavity. A pulse traveling forwards will collide with a pulse traveling backward in the SA sections in this case.

### 2.2.5 Self mode-locked lasers

Recently, another type of mode-locking has been discovered, where no SA or external modulation is necessary, which is called self-mode-locking. In this case, several laser lines are phase-locked together through nonlinear four-wave mixing effects in the cavity, especially in the gain section. In these kinds of lasers, the output spectrum is less concentrated into pulses, but the mode-locking effect causes the light output to be relatively steady, but constantly sweep in instantaneous frequency with a period equal to the repetition rate of the mode-locked laser. A hybrid integrated self-mode-locked laser was demonstrated during the time of the work on this PhD in [4] Using a dispersive element for pulse shaping, it is still possible to measure pulses at the output of these kinds of MLLs. The same kind of mode-locking has also been demonstrated in a hybrid integrated laser with a vernier filter, that was originally designed for single-frequency operation [57, 58]

## 2.3 External cavity MLLs

### 2.3.1 Laser noise

In 1958, before the first laser was demonstrated, a theoretical analysis describing the fundamental limit of the stability of a laser line was published in a paper by A. Schawlow and C. Townes. This paper led to the famous Schawlow-Townes linewidth equation [59]:

$$\Delta\nu_{\text{osc}} = \frac{4\pi h\nu}{P} \Delta\nu^2$$

In this equation,  $\Delta\nu_{\text{osc}}$  is the Half Width at Half Maximum (HWHM) linewidth of the laser line,  $h\nu$  the photon energy at the laser wavelength,  $P$  the optical power in the cavity, and  $\Delta\nu$  the HWHM of the cavity resonance at the laser wavelength.

This equation considers the linewidth of a laser in a perfect environment, assuming there is no instability in the cavity length (due to temperature or mechanical effects). In this case, the only effect causing linewidth broadening is spontaneous emission happening on top of the stimulated emission. If a photon is added to the cavity through spontaneous emission, this can happen with any phase. The phase of the light in the cavity can therefore be pulled slightly forward or backward. This change in phase on every spontaneous emission event causes the frequency of the laser line to broaden. The broadening is therefore inversely proportional to the power inside the cavity since a single photon will have a smaller impact on the total phase if more photons are already present in the cavity.

In 1967, M. Lax adjusted this equation for lasers operated above the laser threshold, in which case the fundamental linewidth is actually half of the linewidth calculated from the original Schawlow-Townes equation [60]. A second change was the addition of the spontaneous emission factor  $\theta$  to the equation to capture the increased spontaneous emission in three-level gain media. The  $\Delta\nu$  in the original equation can also be expressed in terms of resonator roundtrip time  $T_{\text{rt}}$ , outcoupling transmission  $T_{\text{oc}}$  and internal losses  $L_{\text{tot}}$ , and HWHM can be changed to the more frequently used FWHM to get the following equation: [61]

$$\Delta\nu_{\text{laser}} = \frac{h\nu\theta L_{\text{tot}}T_{\text{oc}}}{4\pi T_{\text{rt}}^2 P_{\text{out}}}$$

In this form, it can be easily seen that the fundamental linewidth can be drastically improved by increasing the roundtrip time in the resonator. The first reason for this is that it takes the place of the scaling effect of  $P$  in the original equation, which has been replaced with  $T_{\text{rt}}P_{\text{out}}$ . Since the output power is proportional to the ‘photon density’ in the cavity, increasing the cavity length increases the number of photons in the cavity for a fixed output power. The second reason is that another factor of  $T_{\text{rt}}$  in the modified equation is coming from the resonator bandwidth  $\Delta\nu$  in the original equation.

### **Laser noise in diode lasers**

For semiconductor lasers, there are two extra significant contributions to the linewidth. One is the linewidth enhancement factor  $\alpha$ , the other the Petermann factor  $K$  [46].

The linewidth enhancement factor  $\alpha$  arises due to coupling between the amplitude

and phase of the laser, caused by the fact that the refractive index of the gain medium is influenced by the carrier density. Therefore fluctuations in the phase (due to spontaneous emission) change the gain and vice-versa. The Fundamental Schawlow-Townes linewidth is therefore multiplied by a factor  $(1 + \alpha^2)$  [62]. Linewidth enhancement factors of 5 - 6 are not unusual for typical diode lasers [46].

The Petermann factor  $K$  is a factor on top of the Schawlow Townes linewidth equation that is relevant when the output coupling of the laser is high, as is the case in simple as-cleaved diode lasers. In this case, an assumption made during the derivation of the Schawlow-Townes linewidth is broken. In this derivation, the field amplitude is assumed constant throughout the entire laser cavity, and spontaneous emission is not amplified in the gain medium. This assumption is invalid in the case of high output coupling, where the gain in the laser medium is very high to overcome the losses. Spontaneous emission generated in the laser medium is then also amplified before it leaves the laser, therefore increasing the influence of the spontaneous emission on the phase of the output.

The Petermann factor is a function of reflectivities of the two laser mirrors  $r_1$  and  $r_2$ , and is given by the following equation [46]:

$$K = \left( \frac{(\sqrt{r_1} + \sqrt{r_2})(1 - \sqrt{r_1 r_2})}{\sqrt{r_1 r_2} \ln(r_1 r_2)} \right)^2$$

When combining both the Petermann factor and the linewidth enhancement factor, the Schawlow-Townes linewidth will be multiplied by the factor  $K(1 + \alpha^2)$

Besides the increase of the round trip time by an external resonator, which decreases the linewidth, there is also an additional effect if the external reflectivity experienced by the laser is wavelength dependent. This happens, for example, if an extra wavelength-dependent filter is incorporated in the cavity as well, with a resonance width that is larger than the individual longitudinal modes as shown in Fig. 2.7 There are two opposite effects, depending on which side of the wavelength filter resonance the longitudinal laser mode is [63]. In case the longitudinal mode is on the red side of the resonance, a decrease (blueshift) in the wavelength of the laser line (due to noise) increases the reflectivity experienced by the laser mode. This increases the photon density in the laser, which in turn decreases the carrier density. This decrease in carrier density in turn increases (redshifts) the wavelength of the laser through the carrier plasma effect. When the resonance is on the blue side of the resonance, this feedback loop provides positive feedback, therefore increasing the linewidth of the laser. Both effects (an increase of roundtrip time and feedback effect) are often incorporated into one factor, called chirp reduction factor [63].

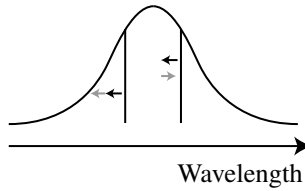


Figure 2.7: An image showing the effect that's captured by the chirp reduction factor. In case a laser mode is on the red (right) side of the wavelength filter resonance, the drift (black arrow) is compensated for by the restoring force from the carrier plasma effect (gray arrow). In case it is on the blue (left) side of the resonance, the drift is enhanced by the same effect.

### MLL RF noise

In a mode-locked laser, there's a second linewidth that is of interest: the RF linewidth. When a comb spectrum is detected on a photodiode with a bandwidth above the repetition rate of the comb, the electrical spectrum will contain a beat note at the repetition rate frequency (and its harmonics). From the optical spectral point of view, this beat note is caused by the summation of the beat notes of every comb line with its immediate neighbors. Since the lines in a comb spectrum are all equally spaced, they will all build up power at the exact same frequency as long as the phase differences of the beat notes allow constructive interference. From the point of view of the time domain, this mainly constructive interference will always be the case when pulses are emitted by the laser since this same RF note will also have to appear in the RF domain when a Fourier transform of the time domain signal of a pulsetrain is taken.

The linewidth of the RF line is important since it plays a role in the detection scheme of many applications of frequency combs. When used for dual frequency comb spectroscopy for example, the RF linewidth imposes a minimum value on  $\Delta f_{\text{rep}}$  to ensure individual RF lines can be distinguished. This in turn imposes a minimum value on the required electrical bandwidth to cover a given part of the optical bandwidth. Lower RF linewidths could therefore decrease the necessary electrical bandwidth for the same optical bandwidth coverage. If the comb is used for a photonic ADC, the RF linewidth dictates the amount of timing jitter in the pulse rate, and therefore the amount of jitter in the sampling rate of the ADC [64].

The fundamental RF linewidth that can be achieved for passively mode-locked lasers is very similar to the optical linewidth, in that there's a fundamental lower limit to the linewidth. This lower limit is given by a Lorentzian shape with a given linewidth [65]. All RF line noise that shows up above this limit could in theory be removed by reducing the influence of external noise on the laser. This is the reason

why many mode-locked laser publications report this fundamental linewidth if it can be measured.

To measure the fundamental RF linewidth accurately, a single sideband phase noise measurement can be done. Such a measurement measures the power spectral density of the RF spectrum at a range of offset frequencies from the RF peak center frequency. The result is usually plotted on a logarithmic frequency scale on the x-axis, and a value in dBc/Hz on the y-axis, where dBc means dB referenced to the intensity of the RF peak that is measured (c for carrier). The fundamental RF linewidth can then be estimated by fitting a Lorentzian line to a phase noise measurement for high enough offset frequencies where there is no impact of other (technical) noise sources anymore, but where the measurement is not yet limited by detector noise. In a typical phase noise plot, this is very simple since it just involves fitting a straight line with a slope of -20 dB/decade to the portion of the data at the highest offset frequency where the measurement is not limited by the flat noise floor of the detector. A good example is shown in Fig. 4.10 a). If no region of the data exists where the slope of the measurement is -20 dB/decade, the fundamental linewidth cannot be measured, as the fundamental component cannot be detected when it's overwhelmed by other noise sources. These other noise sources could be any effect that could theoretically be removed by better stabilization of the laser and the environment around it.

### 2.3.2 Evolution of integrated MLLs

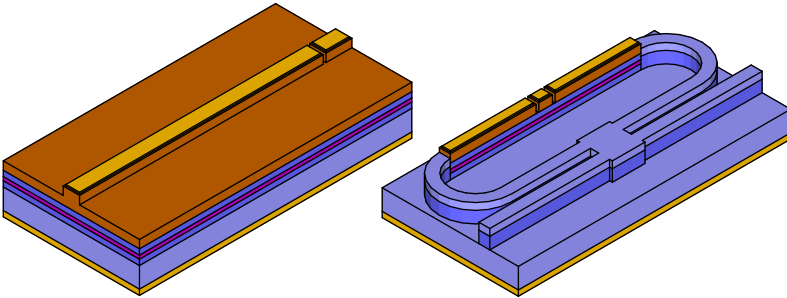


Figure 2.8: Diagram of a monolithic III/V laser (left) and an external cavity laser using active/passive integration (right)

The first demonstrations of integrated MLLs used the same fabrication techniques as used for ridge laser diodes, with the only difference that a small section of the laser was isolated from the rest to use as a saturable absorber [66]. The mirrors were usually cleaved (and sometimes coated) facets. Such a laser is schematically

shown in Fig. 2.8. The cavity lengths achieved this way are relatively short, and this leads to repetition rates above 10 GHz and broad RF linewidths. In order to achieve lower repetition rates and improve noise performance, external cavity lasers were demonstrated.

An external cavity laser is a laser where the laser cavity is split into two parts, where one part provides optical gain, and the second part provides a low-loss delay line to increase the cavity length without introducing much loss. Following the Schawlow-Townes linewidth equation, this is a way to improve the noise performance of the laser. Using an external cavity to increase the cavity roundtrip time is more efficient compared to using the same material that provides optical gain if the laser is driven for the same output power. This is caused by the fact that a longer gain section providing the same amount of net optical gain through stimulated emission will generate a larger amount of spontaneous emission compared to a shorter gain section.

The earliest integrated ECMLLs were made using active/passive integration in an InP platform [67], schematically shown in Fig. 2.8. In these platforms, an active and a passive waveguide cross-section are available. The active waveguide material contains quantum wells which are electrically pumped to provide gain. The passive waveguide is made from a material with a bandgap higher than the photon energy used to prevent it from absorbing the light. The two waveguides are coupled together using butt joints that are made on-chip, with a coupling loss of around 0.1 dB [68]. The lowest repetition rate demonstrated in such a laser is 2.5 GHz, where an RF linewidth of 6 kHz was achieved [56]. The propagation losses in the waveguides used for this laser cavity were 5 dB/cm.

Since the waveguide loss in passive InP waveguides is higher compared to Si or SiN waveguides, switching to Si or SiN waveguides for the extended cavity could be beneficial for MLLs with longer cavities. Transitioning the light from the InP to the Si or SiN waveguide will come with a loss penalty, but the decreased propagation losses in the cavity will compensate for this loss if the cavity is long enough. Two methods have been tried to integrate the two waveguide platforms, heterogeneous and hybrid integration, both schematically shown in Fig. 2.9. With heterogeneous integration, the gain material is placed on top of the Si or SiN waveguides during the processing of the chip. With hybrid integration, the external cavity and the gain material chip are fabricated completely separately, and butt-coupled together after fabrication. This work investigates hybrid integrated ECMLLs.

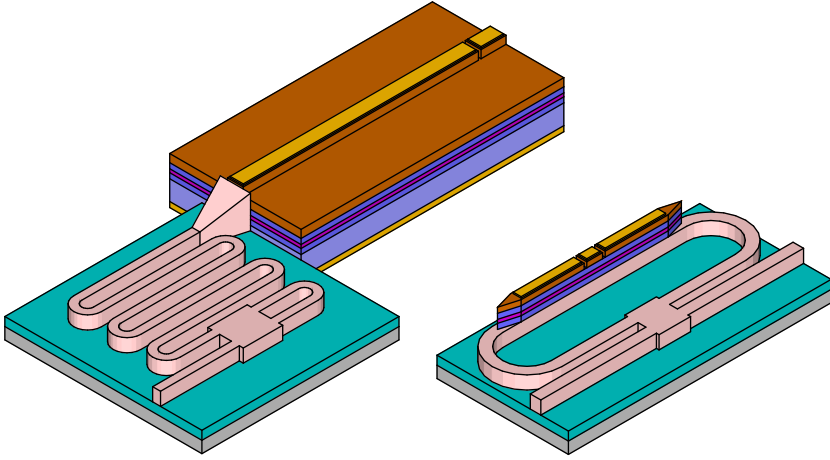


Figure 2.9: Diagram of a hybrid integrated ECMLL (left) and a heterogeneously integrated ECMLL (right)

### 2.3.3 Applicability of hybrid integrated ECMLLs

The repetition rate/cavity length where hybrid integration of an ECMLL becomes beneficial over using the waveguides in an active/passive platform is dependent on the propagation losses in both platforms, and the additional loss introduced by coupling the two platforms together. The option should be chosen where the sum of external cavity loss and coupling loss is the lowest for the cavity length associated with a given repetition rate. An example of this analysis is given in Fig. 2.10. In this plot, the loss of the external cavity is given for different waveguide platforms for the cavity length associated with a range of repetition rates.

In this case, the analysis was done for a laser making use of the SMART MPW platform for the gain section. When using the active/passive integration approach and making the external cavity in the SMART InP platform (orange line), tight bends are needed to fit the cavity onto a chip efficiently. This requires the use of deep-etched waveguides, which have a propagation loss of 3 dB/cm [68]. In this case, no loss penalty is paid for integrating a second waveguide material system, which is why the line will drop to 0 dB for high repetition rates (short cavities). When using a hybrid integration approach, the simulated coupling loss for the design proposed in section 3.2.2 is 1.7 dB for a single pass, leading to 3.4 dB extra loss for a full cavity roundtrip, which is what the loss drops to for high repetition rates. The propagation losses are however lowered significantly, giving an advantage over the InP waveguides at lower repetition rates (longer cavities). The standard SiN waveguides made using the process in the UGent cleanroom have optical

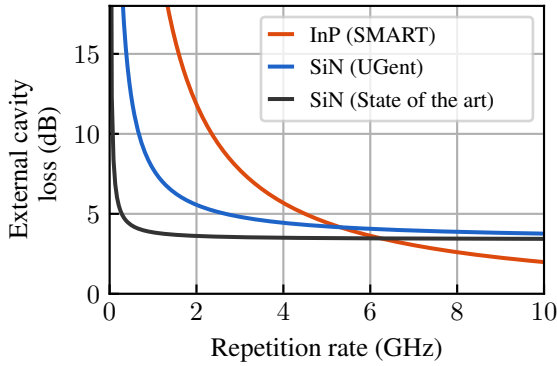


Figure 2.10: External cavity loss caused by several cavities as a function of repetition rate, where InP is made using active/passive integration, and the SiN cavities use an external cavity butt-coupled to the gain chip. Both the SiN waveguides made in the University of Ghent cleanroom and waveguides with state-of-the-art losses are shown. The values used for the calculation are applicable to the laser proposed in section 3.2.2

propagation losses of 0.3 dB/cm at 1550 nm (blue line). Using state-of-the-art waveguides that can be made in commercial MPW runs, this value could be reduced even further to 0.03 dB/cm or lower (black line) [16]. It can be seen that for the SiN waveguides that are used in the UGent cleanroom, hybrid integration becomes beneficial for repetition rates below 5 GHz, which is why the lasers demonstrated in this work were targeted at repetition rates around 2 GHz.



# 3

## Design of hybrid-integrated extended-cavity mode-locked lasers

---

<b>3.1</b>	<b>SiN extended cavities</b>	<b>36</b>
3.1.1	On chip reflector	36
3.1.2	Off-chip coupling	39
<b>3.2</b>	<b>Gain chips on MPW platforms</b>	<b>50</b>
3.2.1	HHI InP platform	50
3.2.2	SMART InP platform	53
<b>3.3</b>	<b>Gain chips on C-mount</b>	<b>55</b>
3.3.1	Post-processing for SA fabrication	55
3.3.2	Innolume gain chips	60
3.3.3	FBH gain chips	62
<b>3.4</b>	<b>Details of fabricated cavity chips</b>	<b>65</b>
3.4.1	Design and simulation procedures	65
3.4.2	Parameters of used chips	69

---

An Extended Cavity Mode-Locked Laser (ECMLL) is made up of two main parts: the extended cavity chip and the gain chip. The first section is about the design considerations for the extended cavity chip, and the simulations necessary to optimize a cavity chip for a certain gain chip. Then it will introduce the different gain chips that were acquired and tested.

### 3.1 SiN extended cavities

The SiN extended cavities used in the fabricated lasers have 4 building blocks, laid out from the gain chip to the outcoupler as follows, as also schematically shown in Fig. 3.1:

- Chip-chip coupler
- Delay line
- Reflector
- Chip-fiber coupler

Section 3.1.1 describes the design and fabrication process for the reflector. Section 3.1.2 describes the design and fabrication of both the chip-chip and chip-fiber couplers.

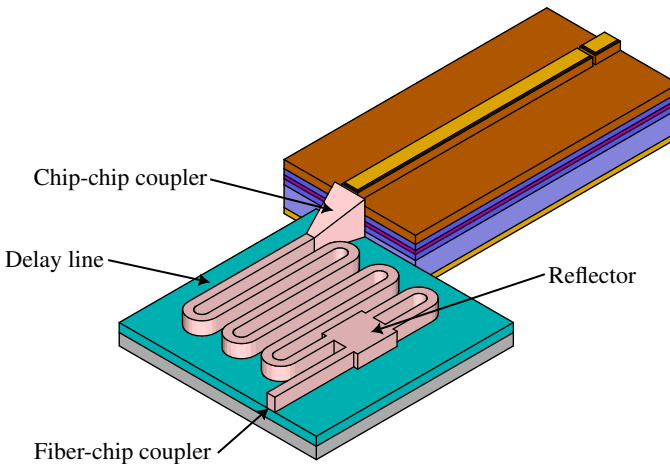


*Figure 3.1: Schematic overview of a Fabry-Perot SCPML mode-locked laser, with the 4 main cavity components indicated*

#### 3.1.1 On chip reflector

In waveguide platforms, many types of reflectors have been realized, each with a different trade-off between the amount of reflection, bandwidth, ease of fabrication, variability, and size.

**Cleaved facet reflectors** are very simple structures, requiring no space. The reflector works because of the Fresnel reflection at the interface between the waveguide and the air. The reflection  $R$  is given by  $R = \left(\frac{n_1 - n_2}{n_1 + n_2}\right)^2$  where  $n_1$  is the effective refractive index of the on-chip waveguide, and  $n_2$  is the refractive index off the chip. This type of reflector has a large bandwidth, but little freedom in choosing the amount of reflection since you're limited in the refractive indices that can be reached by the materials of your chip. For the standard air-clad waveguide of  $1.5\ \mu\text{m}$  wide, this would lead to a reflection of 4.6%.

**Coated facet reflectors** work by depositing a thin-film stack on the waveguide facet. By controlling the refractive indices and layer thicknesses of each layer, both high-reflection and low-reflection coatings can be engineered. The bandwidth of the reflection is dependent on the number of layers used in the stack and falls between cleaved facet reflectors and waveguide Bragg gratings.

**Waveguide Bragg grating reflectors** work by periodically alternating the waveguide cross sections along the propagation direction of the light. Each period will introduce a small reflection of the light. If the period of the alternations matches the wavelength of the light, all reflections interfere constructively, increasing the total reflection. Having more periods increases the reflection, and decreases the bandwidth. Bragg gratings are relatively difficult to fabricate since subwavelength structures need to be patterned. Small manufacturing deviations can move the center wavelength of the reflector. This coupled with the narrow bandwidth makes it difficult to fabricate a reflector targeting a specific wavelength.

**Sagnac mirrors**, also called loop mirrors, work by splitting the light using a  $1 \times 2$  or  $2 \times 2$  splitter, with the 2 output ports connected to each other using a waveguide. Using a  $1 \times 2$  splitter, 100% reflection is achieved, when assuming lossless components. When using a  $2 \times 2$  splitter, the reflection is dependent on the splitting ratio of the splitter.

For the purpose of making a mode-locked laser, broadband reflection is desirable to achieve broader comb bandwidths, which is why the Bragg grating was not chosen. The cleaved facet reflector was also not suitable because of the low reflection. This would reduce the achievable noise performance of the laser. Metal-coated facet reflectors were not chosen because there was no experience with the process in the cleanroom of Ghent University. Therefore, the Sagnac mirror was the only component left, and it was used for the design of the external cavities.

## Sagnac mirrors

Sagnac mirrors are well-suited as reflectors for an integrated MLL because they can offer high bandwidths, and any chosen amount of reflection for a certain wavelength. In the case of a hybrid-integrated MLL, where the reflector on the SiN chip is also the outcoupling mirror, the case of a 100% reflection using a  $1 \times 2$  splitter is not useable.

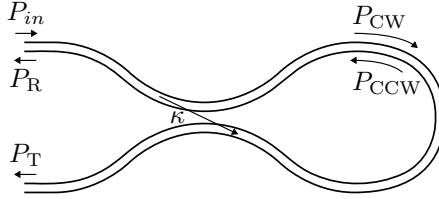


Figure 3.2: Schematic view of a Sagnac mirror, realized using a directional coupler with coupling factor  $\kappa$

For the case of a  $2 \times 2$  splitter, the mirror becomes a 2 port system, where part of the light is reflected, and part of the light is transmitted. It is schematically shown in Fig. 3.2. The reflection is given by  $\frac{P_{1,\text{out}}}{P_{1,\text{in}}}$ . For a power coupling ratio  $\kappa$ , the values of  $E_{CW}$  and  $E_{CCW}$  can be written as a function of  $E_{1,\text{in}}$ :

$$E_{CW} = \sqrt{(1 - \kappa)} E_{\text{in}}$$

$$E_{CCW} = \sqrt{\kappa} e^{j\pi/2} E_{\text{in}}$$

$E_R$  can then be written as a function of  $E_{CW}$  and  $E_{CCW}$ :

$$E_R = \sqrt{\kappa} e^{j\pi/2} E_{CW} + \sqrt{(1 - \kappa)} E_{CCW} = 2e^{j\pi/2} \sqrt{\kappa} \sqrt{1 - \kappa} E_{\text{in}}$$

Taking the intensity of this field leads to  $P_R$ , and dividing that by  $P_{\text{in}}$  leads to the reflection coefficient:

$$R = \frac{|E_R|^2}{P_{\text{in}}} = \frac{4\kappa(1 - \kappa)P_{\text{in}}}{P_{\text{in}}} = 4\kappa(1 - \kappa)$$

This expression is also plotted in Fig. 3.3. As can be seen, the reflection is 100% for a power coupling ratio of 50%, and 0% for ratios of 0% and 100%. It also shows the component is most sensitive to power coupling variations for low-reflection targets.

The  $2 \times 2$  splitter can be chosen to be a directional coupler, or an unbalanced MMI (since a balanced one would lead to 100% reflection). The splitter should be chosen to have very little reflection of its own since it would lead to a spurious reflection on top of the reflection caused by the loop. Because of this, directional couplers are often the best choice, since they lack the abrupt interfaces present in MMI's.

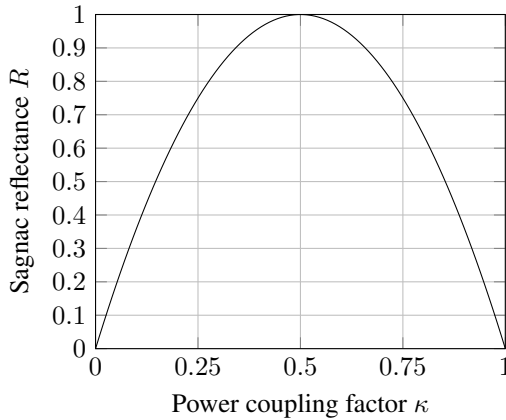


Figure 3.3: Sagnac mirror reflection as a function of the power coupling factor of the  $2 \times 2$  splitter.

### 3.1.2 Off-chip coupling

The off-chip coupling is necessary for 2 things: Coupling between the gain chip and the SiN cavity chip, and coupling from the cavity chip to the outside world, where the light can be used. In this research case, the outcoupling was done to a fiber, to use fiber-based measurement equipment.

The chip-chip coupler is the more crucial coupler of the two because it is inside the laser cavity. Any optical loss and spurious reflections will therefore decrease the noise performance of the laser, and the spurious reflections could possibly inhibit mode-locking altogether.

Of course, while designing the chip-chip coupler, the designs of both the gain chip and the cavity chip need to be taken into account together. Firstly, the gain chip itself should have a facet that leads to low back reflection. This is done by applying two techniques: terminating the waveguide at a small angle relative to the facet, and applying an AR coating to the facet. The angled facet is used to ensure that light that is reflected will not couple back into the waveguide, but into slab modes at a different angle than the waveguide. The AR coating is used to ensure that most light will be coupled out of the chip instead of reflected back at the different angle. If only the angled facet is used, there will still be a significant amount of light lost due to Fresnel reflections. In the case of an effective refractive index of 3.5 and a facet angle of  $7^\circ$ , only 66% of the power is actually coupled out of the chip as calculated using the Fresnel equations for S-polarized light, which is the situation for a TE mode in the waveguide [69].

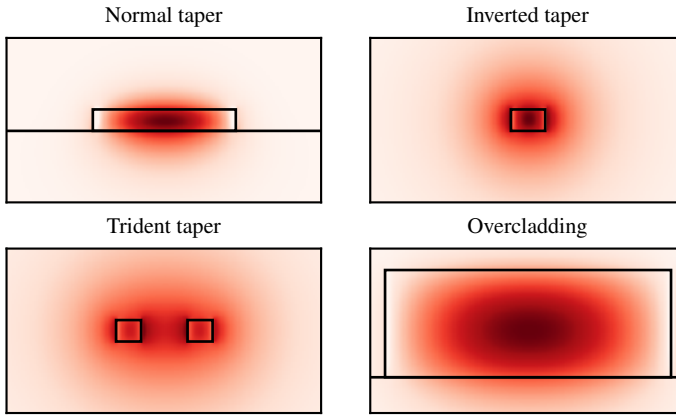


Figure 3.4: The cross-section and mode shape of the four described classes of SSC.

The AR coating is applied by depositing layers on the facet with carefully tuned thickness and refractive indices, as also explained in section 3.1.1. On commercially available gain chips, these coatings are often designed to work optimally when the light is transmitted into air, with the intended use case being extended cavity lasers using conventional free-space cavities.

The mode shape in the gain chip is difficult to alter. Since the performance of the gain chip is dependent on the mode shape, especially regarding small-signal gain and saturation power. On the passive cavity chip, the mode size does not matter for performance, as long as the non-linear effects of the waveguide remain low enough for the used optical powers. Therefore, the design of the cavity chip should be adjusted to match well with the gain chip.

The fixed mode shape determined by the gain chip most likely does not have the same size as the mode of the waveguide on the external cavity chip, therefore, a Spot Size Converter (SSC) should be used. An SSC works by transitioning from the waveguide cross-section used on the chip to another waveguide cross-section, with low loss and low parasitic reflectance. The transition between the cross-sections can be either an adiabatic transition, or rely on interference patterns.

Important aspects in the choice of an SSC are the additional loss introduced by the converter geometry itself, the output mode shape and effective refractive index determining the overlap and Fresnel reflection, and the ease of fabrication. When looking only at the output mode, these SSCs can be divided into several main classes, schematically shown in Fig. 3.4:

**Standard tapers:** In these structures, the size of the waveguide is changed, with-

out introducing any material change. The mode will be mostly confined to the waveguide core material. Therefore, these structures can work, independent of the cladding materials. The disadvantage is that the mode shape cannot be increased in height without changing the layer thickness as well. The effective refractive index is slightly lower than the core material.

**Inverted tapers:** In these structures, the size of the waveguide is also changed, but it is shrunk down, to push the mode into the cladding material. The advantage of this over standard tapers is that the mode will also increase in height. Inverted tapers can only work well in a cross-section where the cladding material is the same refractive index all around the core waveguide. If there is a significant mismatch in the index of the bottom and top cladding, the mode will propagate in the cladding with a higher index. Additionally, inverted tapers can only support mode shapes that are close to circular. The effective refractive index of the output mode is slightly higher than the cladding material.

**Trident tapers:** These tapers are similar to inverted tapers, in that they use narrow waveguides and the mode mostly propagates in the cladding material. The difference to a normal inverted taper is that more than one narrow tip is used. In this way, the mode shape can be adapted to a non-circular shape. This technique can be used to spread out the mode either vertically or horizontally. The refractive index of a trident taper is also slightly higher than the cladding material, just as in a normal inverted taper. A symmetric cladding material is also a requirement for effective structures.

**Thin-Overcladding SSC:** Thin overcladding SSCs are very similar to normal tapers, where the mode is mostly guided inside the core material. The difference is that this core material is different from the core material on the standard waveguide on the chip. Since the output waveguide is made in a different material, the thickness of this material can be tuned without altering the waveguide performance on the chip. For an overcladding SSC, a material with a lower refractive index than the normal core material is used. It is introduced over the normal waveguide, after which the normal waveguide tapers down to adiabatically transition the mode to the overcladding waveguide. The refractive index of the mode in this type is slightly lower than the refractive index of the overcladding material.

Both the inverted taper and the trident taper were not easily feasible in the cleanroom of Ghent University for devices working at 1550 nm. Since the used SiN is deposited on buried oxide, an oxide cladding has to be deposited over the chip. All oxide that can be deposited in the cleanroom of Ghent University has an absorption peak around 1550 nm, therefore using this would significantly increase the losses on the entire chip.

The other two options that could be fabricated are the normal taper and the overcladding SSC. Both of these options have been fabricated. The following two sections will describe the fabrication of the normal tapers in our SiN, and overcladding tapers using SU8.

### Design of an SSC

Since the gain chip dictates the mode shape at the chip-coupling interface and the emission angle of the light beam, the only thing that needs to be done in the design of the SSC facet is to optimize the dimensions for the highest overlap, and afterward set the facet angle so the output angle in air of the beam is the same for both chips.

To optimize the dimensions, the actual mode shape at the facet of the gain chip needs to be used. Either this can be known from a simulation of the gain chip waveguide structure, or it can be taken from the datasheet of the chip. Often, the data sheets of gain chips only mention beam divergence angles in the horizontal and vertical plane, either as a Full width at Half Maximum (FWHM) or as a Full width at  $1/e^2$  intensity. In the case angles are given, a Gaussian approximation of the output mode is used, and the width and height of the Gaussian beam emitted from that can be calculated from the divergence angles and the wavelength.

The output angle of the beam is either given directly in the datasheet, or it can be calculated from the facet angle and the effective index of the mode in the gain chip through Snell's law  $\frac{\sin\theta_1}{\sin\theta_2} = \frac{n_2}{n_1}$ .

In the case of an overcladding SSC, a structure to transition the optical mode from the SiN waveguide to the overcladding waveguide needs to be designed as well. This can be achieved using an inverted taper of the SiN waveguide material while it's covered by the overcladding, as schematically shown in Fig. 3.5. Three things significantly impact the efficiency of such a structure: The mode overlap between the modes at both sides of the sudden waveguide transitions, and the taper length. The sudden waveguide transitions are the point where the overcladding material is introduced, and at the tip of the SiN taper, where the SiN waveguide abruptly stops. In the schematic, the introduction of the overcladding is done at an angle, to decrease the amount of reflections coupled back into the waveguide.

### Fabrication of normal taper SSCs

The fabrication of normal taper SSCs was attempted using the standard SiN wafers used in the cleanroom of Ghent University. These wafers are bought from LioniX International. The layer stack consists of a 750  $\mu\text{m}$  silicon substrate, followed by

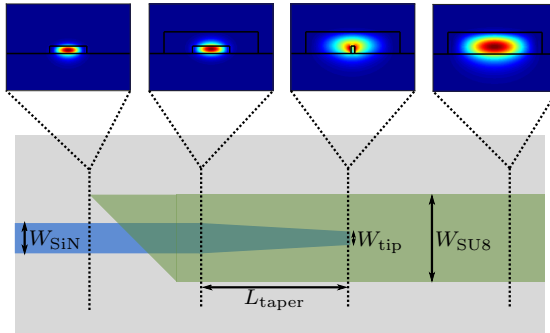
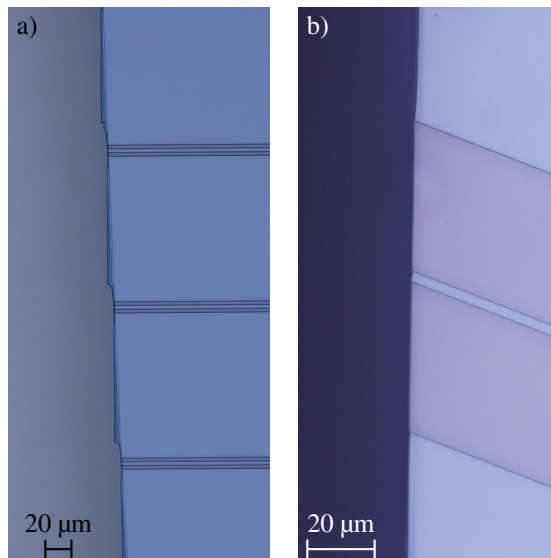


Figure 3.5: Schematic of the transition from the SiN waveguide on the left to the overlapping waveguide on the right of the image. The mode images show the mode profiles right before and right after the sudden transition at both ends of the SiN taper section.

3.3  $\mu\text{m}$  thermal oxide, and finished with 300 nm of LPCVD silicon nitride [70]. Two things need to be realized for the normal taper SSC to work. First, at the part of the chip where outcoupling should happen, the waveguide should be tapered to the desired cross-section at the facet. Afterward, the entire chip should be cleaved or diced through the waveguides at the location with the desired cross-section. Care should also be taken that the waveguide is at the correct angle for the gain chip it will be used with.

Before starting the experiments, a process was already available in the cleanroom of Ghent University for fabricating facets for coupling out of a chip. These facets were used for coupling to a lensed fiber. In this process, the wafer is thinned down using a grinding tool, from the initial 750  $\mu\text{m}$  thickness to around 300  $\mu\text{m}$ . This process can be done either before any processing is done (both wafer- or sample-scale), or after the waveguides have been etched. The wafers are easier to cleave after the thinning process, and the cleave line will deviate less from the initial scratching position. Fig. 3.6 a) shows the result of the initial fabrication process.

It can be seen from the image that the cleave is far from perfect. The waveguide facets seem to be flat (although this can only be really seen at higher magnification), but the SiN that is not removed between the waveguides is not following the cleave line of the substrate. This is likely caused by the fact the SiN is not the same crystal structure as the substrate, and that it is under stress. For the case where a single lensed fiber is coupled to the waveguide, this would not be a problem, since the lensed fiber will not bump into the parts of SiN that are sticking out of the facet. For chip-to-chip coupling though, these parts of SiN do pose a big problem, since



*Figure 3.6: Microscope images showing problems with cleaved facets in our SiN wafers. a) shows the overhanging SiN. b) shows the waveguide facet not following the desired angle for angled facets, as well as the wider trench in the cladding to solve the problem of SiN sticking out of the facet.*

the second chip will bump into these, which will limit how close together the two waveguide facets can be. Therefore, the SiN in between the trenches of several waveguides should be etched away as well, so it cannot stick out from the facet.

Another trial was done with an angled facet, with a 3  $\mu\text{m}$  wide waveguide (used for outcoupling to a lensed fiber) at an angle of 10 degrees. The result can be seen in Fig. 3.6 b). It can be seen that the cleave through the actual waveguide does not follow the angle of the rest of the facet, but it goes at a right angle to the waveguide direction. This is also because the actual waveguide is indirectly cleaved. It does not have to follow the crystal directions of the substrate and therefore will break in the direction that is weakest, which is the direction that leaves the smallest surface exposed after the break.

The problem with the angled facet breaking at the wrong angle is a fundamental problem with cleaving [71]. Therefore, a method that directly removes the SiN layer is necessary. There are two options, dicing and/or polishing. Dicing works by cutting the chip with a dicing saw. This cuts both the substrate and the SiN layer at the same time, therefore circumventing the problem of the indirect cleave. Polishing starts from a cleaved or diced facet that is not perfectly smooth. By polishing the facet, material is slowly removed until a flat and smooth facet is achieved.

Several tests with dicing were done, both on samples of the original  $750\ \mu\text{m}$  thickness and on samples thinned down to  $300\ \mu\text{m}$ . The problem with dicing is shown in Fig. 3.7. Along the diced facet, there are many holes going into the SiN layer. This phenomenon is called chipping [71]. The chipping also happens in the trenches of the waveguide, and therefore, the position of the facet of the actual waveguide is still not well controlled. This would result in a low yield of these facets. There was a polishing blade available, which is supposed to give a smooth facet, but it is designed to work in a two-step dicing process, where the top layer of the chip is slightly deeper into the chip, as shown schematically in Fig. 3.8. This works well if the targeted application is to couple from the chip to a (lensed) fiber, but it will not work when coupling to a second chip, since the substrate will collide with the chip, leaving a large gap between both waveguide facets.

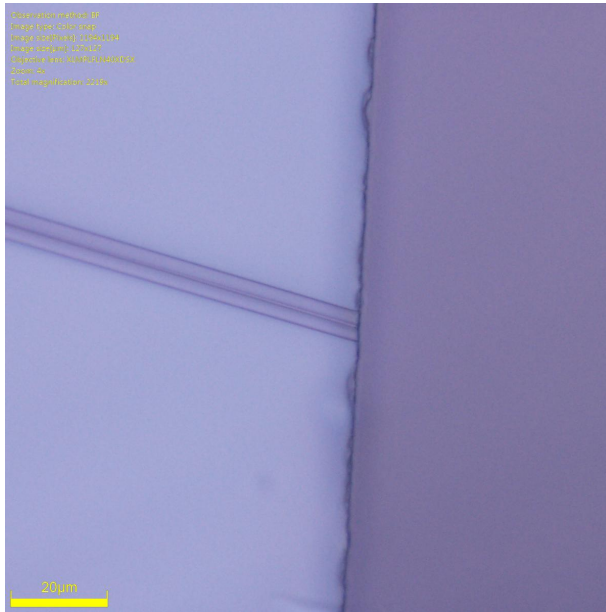


Figure 3.7: A zoom on the chip facet after dicing. A lot of chipping can be seen.

Polishing was not tried, because of the time the process takes. It has been done in the cleanroom of Ghent University, by H. Zhao, and the process is described in his thesis [72]. The SiN used was different though, and it was unsure whether the polishing would work well for the LPCVD SiN wafers used in this work. Therefore, a switch was made to fabricating thin-overcladding SSCs.

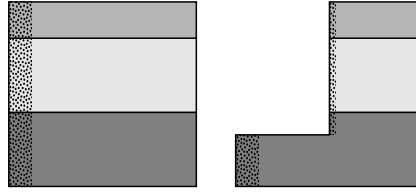


Figure 3.8: Schematic view of the polished dicing process, starting with a coarse dice (left), a second shallow dicing step is done with a polishing blade, leaving a side-view of the facet as seen on the right. The dotted area shows the depth of the defects caused by dicing.

### Fabrication of thin-overcladding SSCs

A large advantage of an overcladding SSC is the fact that the thickness of the SSC can be freely chosen, without impacting the rest of the chip. In order to not impact the rest of the chip, an overcladding material should be chosen that can be etched without impacting the underlying SiN waveguides. Also, the refractive index has to be higher than the undercladding of the normal waveguide structure. If this is not the case, the mode will transition to the bottom cladding instead of the overcladding in the taper section. If the index is also significantly lower compared to the normal waveguide core material, no narrow taper tips need to be defined in the overcladding for an efficient transition, since the overcladding can, in that case, be introduced to the waveguide with an abrupt transition, without causing much reflection.

Some photoresists are a very good material choice for overcladding SSCs. The refractive index of many photoresists is slightly higher than that of oxide, due to the spinning process the layer thickness can be easily tuned, and the photolithography process used to pattern the photoresist layer will not affect the rest of the chip. In order to choose a specific photoresist, the desired thickness range, the refractive index and the stability over time of the photoresist are important parameters.

Of the resists used by the Photonics Research Group in the cleanroom of Ghent University, SU-8 was designed to be very stable after the baking step and to never be removed after the baking step. Additionally, the photoresist is transparent for a large range of wavelengths and is marketed to be used for waveguides as well [73]. Therefore, SU-8 was the material of choice for the overcladding SSCs.

For the gain chips used, vertical mode sizes were between 1 and 2 micrometers. To match these modes, the SU-8 thickness would need to be in the same range. Therefore, the least viscous variant SU-8 2 was used. The spin curve was measured on the spinner available in the cleanroom of Ghent University, and is shown in Fig. 3.9.

In the Ghent University cleanroom, the standard wavelength used in the lithography tools is 320 nm. For SU8, it is recommended to not expose it with any light with a wavelength below 350 nm. This would be absorbed mostly in the top layer of the resist, and therefore form a negative sidewall angle [73]. Therefore, the light filter in the tool should be changed while exposing SU8, to what is nicknamed the SU8 filter in the Ghent University Cleanroom. This filter is an i-line (365 nm) bandpass filter, which blocks all light from the light source except the i-line.

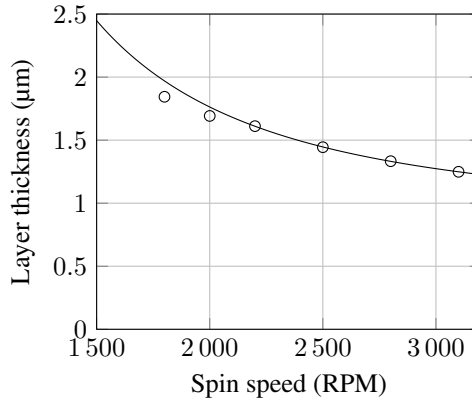


Figure 3.9: Spin speed curve of SU-8 2 measured in cleanroom of Ghent University.

The process flow used is as follows:

- Acetone, IPA, water clean
- 20 minutes Tepla (for adhesion), 500 SCCM O<sub>2</sub>, 500 W RF power
- Spin SU8-2, 60 seconds, acceleration 010, RPM as in Fig 3.9
- Pre-exposure bake 65 °C, 1 min, then 95 °C, 1 min
- Expose 45 seconds through SU8 filter
- Post-exposure bake 65 °C, 1 min, then 95 °C, 1 min
- Develop in undiluted SU8 developer, 50 seconds, no agitation
- Hardbake 65 °C 1 min, 95 °C 1 min, 130 °C 30 min, 65 °C 1 min, 95 °C 1 min
- Cleave sample

In all baking steps, the temperature is slowly ramped up and down, by using several hotplates and transferring the sample between them quickly. If the ramping is skipped, cracks will form in the SU8 layer.

An image of the final fabricated SU8 edge coupler can be seen in Fig. 3.10 a). Optically, the waveguide seems almost flat, and most importantly, the facet follows the cleave of the substrate. An SEM image of the facet was also taken, and can be

seen Fig. 3.10 b). It can be seen that the facet is not perfectly flat, which will likely cause some extra coupling loss to the gain chip. The emission angle of the light will likely not be impacted significantly.

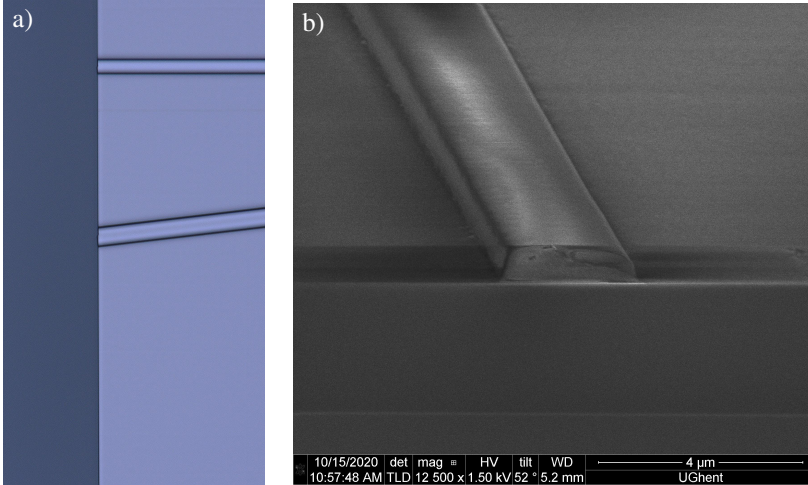


Figure 3.10: Images of the SU8 facet after cleaving. a) shows an optical microscope image, b) an SEM image.

### Optical power damage threshold in SU8 SSCs

The SU8 SSC on the first fabricated cavity chip that was coupled to the angled FBH chip measured in section 4.4 broke during the alignment procedure with the gain chip. Since the central wavelength was visible on the camera used in the setup, the intensity of the scattered light from the cavity was used as optimization parameter for the alignment, and therefore the gain current on the chip was set to the maximum allowed current. During optimization, the cavity chip suddenly went very dark, and the alignment could not be restored. After inspection of the cavity, it was clear the SSC was damaged, and a large part of the SU8 was removed. Particles seemed to be scattered around the original location as well.

Initial thoughts were that the optical power in the SU8 SSC had gone above the damage threshold for the material. In [74] the laser-induced damage threshold for SU8 was measured using both a 1064 nm 11 ns and a 1030 nm 343 fs pulsed laser source. In the ns regime, the measured damage threshold was  $0.49 \pm 0.09 \text{ J/cm}^2$  for 1000 pulses, while in the fs regime it was  $0.17 \pm 0.05 \text{ J/cm}^2$  for 1000 pulses.

Taking the cross-section of the SU8 ( $1.6 \times 2.0 \mu\text{m} = 3.2 \times 10^{-8} \text{ cm}^2$ ) as the area the pulse travels through, the maximum pulse energy becomes 15.7 nJ for ns pulses,

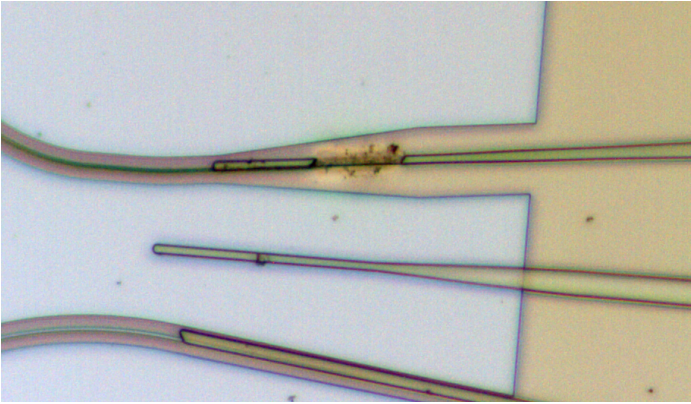


*Figure 3.11: Microscope image of the SU8 edge coupler that was damaged.*

and 5.4 nJ for fs pulses. The fundamental repetition rate of the cavity where the damage was observed was 9 GHz. In order to reach a 5.4 nJ pulse energy in that case, where fs pulses were measured to damage SU8, an average in-cavity power of 48.6 W would be necessary. For ns pulses, 141 W would be necessary. Both these powers were obviously not reached in the case where the SU8 SSC converter was damaged since the pump power into the gain chip was below 1 W.

The measured data can however most likely not be directly mapped to the case of the SU8 waveguides though, because the geometries used are very different. In the cited work, a uniform layer of SU8 with a thickness of  $11.8 \pm 0.72 \mu\text{m}$  on top of 1 mm thick soda-lime glass was illuminated by the laser from above. The beam profile was a Gaussian beam with a diameter of  $44 \mu\text{m}$  ( $1/e^2$ ) [75]. This situation is of course very different compared to light being guided inside the significantly smaller SU8, surrounding a SiN taper tip, especially at ns pulse timescales, where thermal effects are most significant [74]. At ps timescales, no data was found for SU8.

Still, the damaged SU8 was attributed to a particle, either on the SU8 or embedded inside the SU8 during the fabrication, that was absorbing at 1064 nm and started a chain reaction damaging the rest of the SU8 around it once the in-cavity optical power got high enough during the alignment of the gain chip. A second fabrication run yielded several working cavities where the SU8 SSC's were never damaged, even though the same gain current was used on the gain chip.

## 3.2 Gain chips on MPW platforms

For the first demonstration of a hybrid-integrated MLL, it was chosen to use a gain chip made in an MPW run as the gain material. This would allow to have many slightly different gain sections, to increase the chance of a working laser. Also, since they are delivered as bare dies, there is total freedom in the mounting method. Two different chips were designed. The first one in HHI's MPW platform, and the second one in the MPW platform of SMART Photonics.

In both MPW platforms, two types of lasers were realized: A ring laser design, and an Self-Colliding Pulse Mode-locked Laser (SCPML) design. It was opted not to make Anti-Colliding Pulse Mode-locked Laser (ACPML) mode-locked lasers, since that would necessitate using space on the die for outcoupling from the laser (implementing the SA in the external cavity was not considered), reducing the number of different laser designs that could be put on a single chip. Additionally, this would make the measurement setup significantly different compared to lasers made using C-mounted Reflective Semiconductor Optical Amplifiers (RSOAs).

Both platforms use two different cross sections for the active waveguides and passive waveguides, which are butt-jointed together [76]. Therefore, each transition between active and passive waveguides comes with a small loss- and reflection-penalty, and should be kept to a minimum. Another similarity between both platforms is that optical grade facets could only be realized on two sides of the chip, namely the east and west facets. Additionally, active waveguides could only be oriented horizontally, meaning the light is guided perpendicular to the output facets.

### 3.2.1 HHI InP platform

An image of the layout of the HHI gain chip is shown in Fig. 3.12. The size of the chip is  $2 \times 6$  mm. The structures from top to bottom of the image on the west facet are: A gain test structure, 2 Fabry-Perót MLLs with an etched facet reflector an 1 Fabry-Perót MLLs with a loop mirror. From top to bottom on the east facet the structures are a test structure for the SA, and 2 ring type MLLs.

In the HHI platform, no compact mirror building block was available. Therefore, to implement the SCPMLs, two different mirrors were tried. A loop mirror using a  $1 \times 2$  MMI for 100% reflection, and a more compact mirror realized using an etched facet mirror on the chip. A grating-based reflector was available in the platform, but it was opted not to use it, due to its low reflection bandwidth of around 3 nm.

Because of the design rules in the platform regarding transitions between active and passive waveguides, there is a significant amount of space between where the

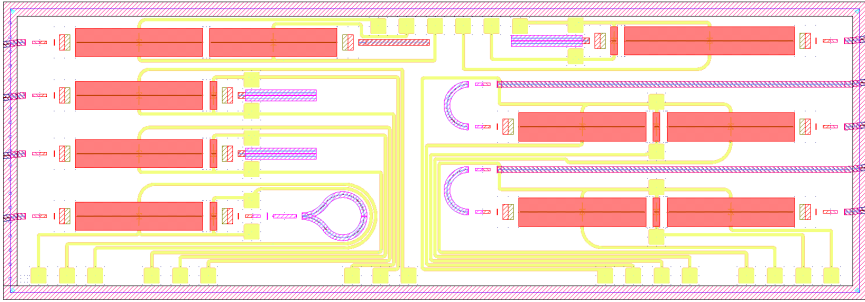


Figure 3.12: Layout of the HHI gain chip design. West facet top to bottom: 1 SOA gain test structure, 2 etched facet MLLs, and 1 loop mirror MLL. East facet top to bottom: 1 SA test structure, 2 ring type MLLs.

SA ends, and where the mirror structure can start. This space is used for the butt joint between the active and passive waveguide. The butt joint takes up  $150\ \mu\text{m}$ , and transitions to a shallow-etched waveguide. The optical pulse has to pass this transition twice between the first and second pass through the SA, taking a time of  $3.4\ \text{ps}$ .

An etched facet somewhere in the middle of the chip was not available as a building block in the platform, therefore it was realized by ending a medium-etch depth waveguide in the middle of the chip, and using the etched trench in between two deep-etched waveguides to act as the etch-step forming the facet for the medium-etched waveguide. This is schematically depicted in Fig. 3.13. Since the effective index of the waveguide is around 3.4, the Fresnel reflection at this facet is 30%.

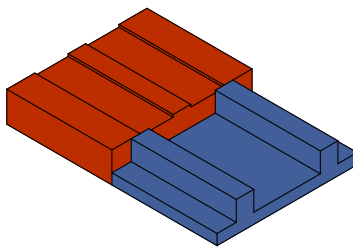


Figure 3.13: Schematic view of the facet mirror. The waveguide connecting to the gain section is in red, and the deep-etched waveguides are in blue and used only for their trench etch. Etch depths are to scale.

The loop mirror is implemented using a  $1 \times 2$  MMI, where the 2 output ports are connected to each other. The length of waveguide used for this comes from 2 bends outwards with a radius of  $200\ \mu\text{m}$  and an angle of  $55^\circ$ , and an inwards bend with

150  $\mu\text{m}$  bend radius and an angle of  $290^\circ$ , meaning a total waveguide length of 1.14 mm which the pulse passes once. The MMI length is 244  $\mu\text{m}$ , which has to be passed twice. Additionally, the MMI is made in a deep-etched waveguide, adding 205  $\mu\text{m}$  that is passed twice for the shallow-etch to deep-etch transition. Therefore, the light travels 3.06 optical mm between entering and exiting the mirror, taking 10.2 ps. The 3.4 ps for the active-passive transition has to be added to this as well, for a total time between both passes of the SA of 13.6 ps. Therefore, the optical power enhancement in the SA due to the pulse colliding with itself is not expected to happen, since the expected pulse lengths are around 10 ps for MLLs in this platform [77]. Therefore, only one of the lasers on the chip was implemented using the loop mirror, as a backup if the facet mirrors would not work.

A ring laser was also implemented on the platform. In order to keep the geometry as symmetrical as possible, both gain sections and the SA were placed in a line, also preventing extra active-passive transitions. After the active sections, a 180-degree bend was placed to route the light back to the facet. The distance between the two waveguides of the ring laser along the facet was 300  $\mu\text{m}$ .

Two ring laser designs and a facet-laser design fit on the east side facet of the chip. The west side facet contained the loop mirror laser, 2 facet lasers, and a test structure for the gain sections. The gain-section lengths were chosen to fill out the chip area and ended up at 900  $\mu\text{m}$  for all the gain sections, except the facet laser on the east side which has a 1200  $\mu\text{m}$  gain section. All SA sections were 50  $\mu\text{m}$ , since this is the minimum length of an SOA section in the process.

Additionally, two test structures with multiple gain sections in a row were added, which could be used for measuring the gain and (saturable) absorption characteristics of the SOAs, placed on the top of the chip.

To test the gain chip, it was mounted to a PCB and wire bonded. An external laser was sent into port 1 of a circulator, port two was connected to a lensed fiber that was coupled to an RSOA on the HHI chip. Port 3 of the circulator was connected to an OSA. The external laser was set to 1550 nm, and the minimum output power of -15 dBm was used. The lensed fiber alignment was done by optimizing for the amount of ASE coupled out of the cavity. After turning on the external laser, the strength of the 1550 nm peak on the OSA was measured as a function of input power for several gain currents. This allows us to measure both the gain and the saturation power. The measurement results can be seen in Fig. 3.14. To compensate for coupling loss from the lensed fiber to the chip, the simulated value of 3 dB was used. An extra 1.7 dB of loss in the circulator was also taken into account. It can be seen that at the maximum current and below the saturation power, the gain is 4 dB. This would mean that to make a useful external cavity laser, the total loss introduced by the cavity has to be below 4 dB to have a threshold current below

the maximum current, and even then the laser can only be operated slightly above threshold. This was deemed unfeasible.

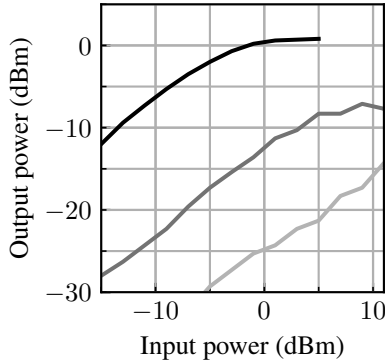


*Figure 3.14: Gain and saturation measurement of the HHI RSOA at three different gain currents of 20 (lightest line), 70, and 110 mA (darkest line). The output power after a single pass of the RSOA is plotted as a function of the input power. It can be seen that even at the highest gain current the light is amplified by 4 dB at most in the RSOA, which is not enough to make an ECMLL work, due to the extra losses caused by the external cavity and outcoupling from the laser.*

Additionally, the voltage to the gain section was not stable, and the optical output power showed transient behaviour upon turn-on, starting high, and settling to a lower output power in around 2 seconds. A reason for this was not found. Because of this fact and the low gain, no more experiments were done with these chips.

### 3.2.2 SMART InP platform

In the SMART platform, more space was available compared to the HHI platform, and therefore many more lasers could be fabricated. This meant that every laser could be doubled, and put close to each other, with the intention of coupling two gain section structures to two cavity structures on the same SiN chip at the same time to generate two optical combs simultaneously. This could be useful for dual-comb applications. The layout of the SMART chip can be seen in Fig. 3.15.

A compact, medium bandwidth mirror was available in the PDK, in the form of a Multi-mode Interference Reflector (MIR) [78]. The typical reflection is 60 to 70%. Since this was a proven PDK component, this was the only mirror that was used in the design. This mirror can be connected directly to an SOA section since the butt joint connection between the two waveguide types takes no space. The length

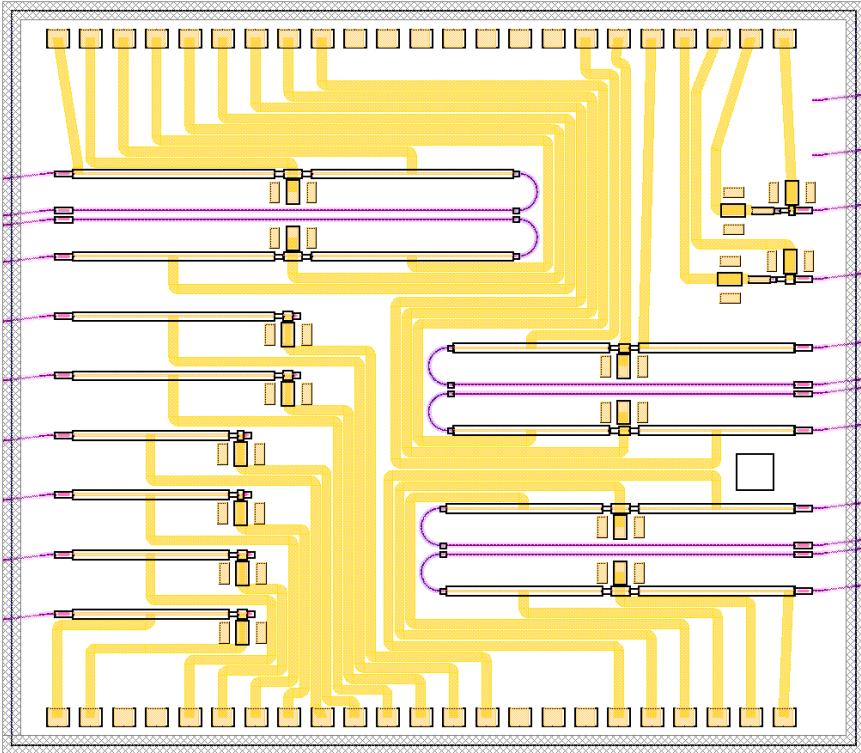


Figure 3.15: Layout of the SMART gain chip design. The sections that were used for the final laser are the two structures at the bottom of the west facet in this image.

of the MMI is  $39.2 \mu\text{m}$ . Therefore, the time it takes the pulse between exiting and entering the SA section is  $0.9 \text{ ps}$ , significantly better than what could be achieved in the HHI platform. Self-pulse collision is therefore expected in the SAs of these devices.

On the SMART platform coupling in and out of the chip can only be done using the predefined building blocks for edge couplers, where the only choice is between a straight facet and an angled facet. These coupler waveguides are multimode, therefore, a  $1 \times 1$  MMI mode filter was inserted after the coupling structure to suppress lasing at multiple modes.

Fabry-Pérot lasers were implemented on the chip with the following lengths:

- $2 \times 850 \mu\text{m}$  gain section,  $30 \mu\text{m}$  SA
- **$2 \times 850 \mu\text{m}$  gain section,  $50 \mu\text{m}$  SA**, characterized in section 4.2.
- $2 \times 1100 \mu\text{m}$  gain section,  $50 \mu\text{m}$  SA

Ring lasers were implemented with the following lengths:

- $2 \times 850 \mu\text{m}$  gain sections,  $100 \mu\text{m}$  SA
- $2 \times 850 \mu\text{m}$  gain sections,  $50 \mu\text{m}$  SA
- $2 \times 1100 \mu\text{m}$  gain sections,  $100 \mu\text{m}$  SA

The final lengths of the gain sections were chosen to fill out the horizontal chip space with the longest gain sections possible with the given chip space, while only using two different lengths across all laser types. The lasers with the  $850 \mu\text{m}$  gain section and  $30 \mu\text{m}$  SA were used for the characterization in section 4.2.

Additionally, two test structures were implemented that could be used to characterize the absorption of the SA.

### 3.3 Gain chips on C-mount

In addition to custom gain chips on MPW runs, chips on an industry-standard C-mount were also used for the experiments. Three of the gain chips obtained had no SA, therefore, post-processing was tried to turn the single gain section into two electrically isolated sections, with the larger section being the gain section and the smaller section being the SA. Several other gain chips did include an SA section already.

#### 3.3.1 Post-processing for SA fabrication

##### GaSb Gain chip

The first gain chip where post-processing was tried was a prototype GaSb gain chip from Brolis. GaSb gain chips have operating wavelengths between  $1.7$  and  $2.5 \mu\text{m}$  [79]. The starting point was a monolithic laser mounted to a C-mount, with one HR-coated facet, and one outcoupling facet that provided enough reflection for lasing without external feedback. The laser bar had only one gain section and no SA. Therefore, post-processing steps were done to create an SA, which would be achieved by etching away metal contact and the P-doped layer around a region that would form the new SA section. Removing both these layers removes the electrical conduction path between the two metal contacts.

It was initially opted to try isolating an SA section using Focused Ion Beam (FIB)-milling for two reasons: No etching recipes in the cleanroom had been tested on GaSb before, and removing the bond wires to enable optical lithography was deemed too risky for the chip. Using FIB milling, no optical lithography is necessary, and

the etching depth can very easily be tracked during etching. A disadvantage of FIB milling is the ion implantation caused in the etched region, which could reduce the amount of electrical isolation between the gain section and the newly defined SA section.

The result of the FIB milling is shown in Fig. 3.16. It can be seen that the isolation etch is split into three sections: The outside regions far from the waveguide with an etch depth of at least 10 microns, while the center section near the waveguide is etched less deep. The two different etch depths were used to create as much electrical isolation between the two sections as possible while reducing the optical loss introduced by the cut in the waveguide. Unfortunately, the shallow etch near the waveguide region was still etched very deep into the waveguide, shown in Fig 3.16 b). This is an SEM image taken after 1 side had been deep etched, and the center had been shallow etched. The deep etch causes a significant optical loss in the waveguide.

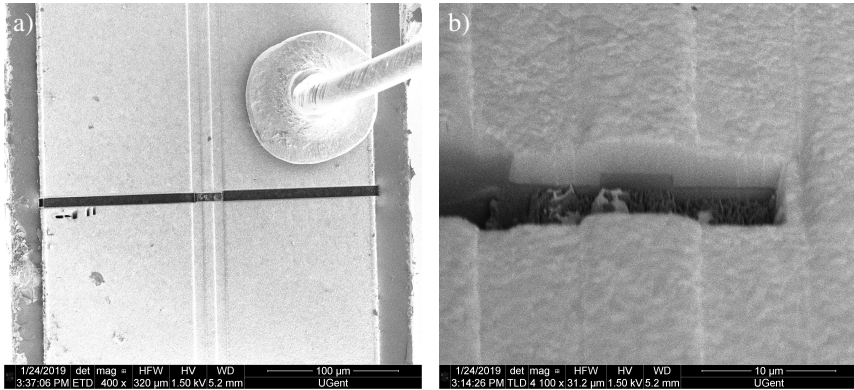


*Figure 3.16: SEM images of the FIB cut made in the GaSb gain chip. a) shows the overview of the chip, showing the deep and shallow etch. b) shows a zoom on the cut near the waveguide, showing the etch was significantly deeper than the ridge depth, causing high optical losses*

IV curves were measured before and after the post-processing using the FIB, and they are shown in Fig. 3.17. It can be seen that the IV curve is significantly altered, and a parallel resistance has been added to the diode. This is attributed to the ion implantation caused by the FIB milling creating an additional electrical conduction path around the diode. This additional path reduces the electro-optic conversion efficiency of the SOA.

Additionally, the electrical isolation between the SA section and gain section contacts was measured to be  $37 \Omega$ . This is a very low value and would mean that a significant current from the gain section source is flowing around the diode through

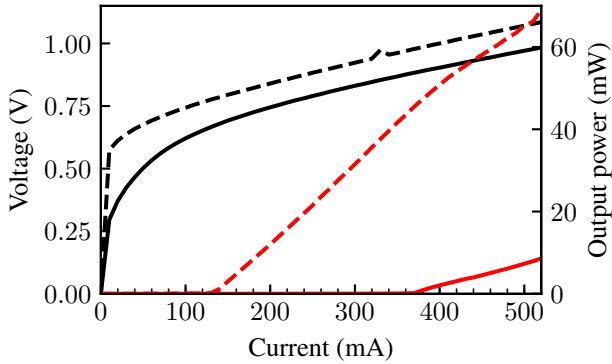


Figure 3.17: LIV measurements of the GaSb gain chip before and after the FIB processing. Black lines show the voltage and red lines show the output power as a function of current. The solid line is the post-processed laser while the dashed line is the unmodified laser.

the voltage source connected to the SA. This effect was also attributed to the ion implantation, creating a conduction path between the two electrical contacts.

Finally, the LI curve of the laser was measured before and after the post-processing. The results are shown in Fig. 3.17. It can be seen that the threshold current has increased significantly, and the slope efficiency was decreased. Both effects are likely caused by a combination of the added optical loss in the cavity, as well as the reduced electro-optic conversion efficiency.

### SAF 1126 gain chip

The SAF 1126-55-90-COS was the second gain chip without an SA that was acquired. It is marketed to be used with an external free-space cavity or a fiber Bragg reflector cavity. The chip came mounted to a submount, which was then mounted to a C-mount by an external company so it could be used in the available setup. Since it uses an angled facet, it would not lase without external feedback. The gain material is InP, and the operating wavelength is 1550 nm.

Even though the results of the FIB processing on the GaSb were not promising, similar processing was also tried on the InP gain chip, since the different material would react differently to the ion implantation caused by the FIB processing, which might make the method usable for InP gain chips.

To test the isolation between a FIB-separated contact and the original contact without damaging the waveguide yet, two square sections were isolated in the bulk

part of the gain-chip, one with a shallow etch and one with a deep etch, as shown in Fig. 3.18. The shallow etch was intended to remove the metal contact and the P-doped layer, while the deep etch was intended to etch through the entire diode structure.

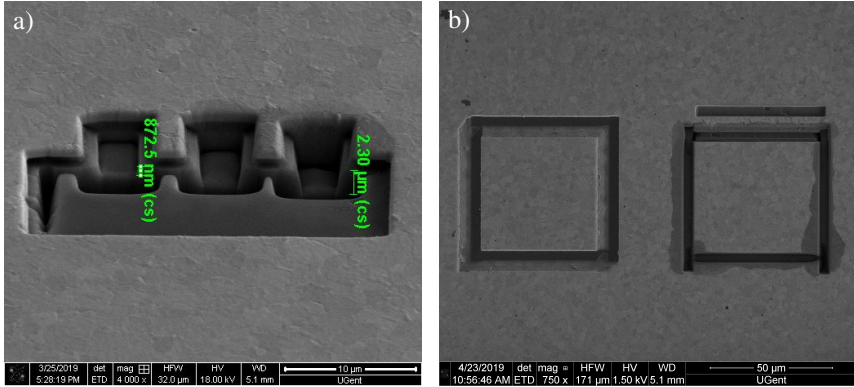
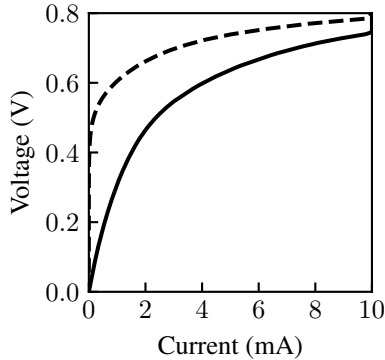


Figure 3.18: SEM images of the FIB cut made in the InP gain chip. a) shows the cross section of the shallow etch (leftmost etch) and deep etch (rightmost etch) used. The two steps in the etching tests are caused by the different etching speeds of the metal contact and the InP. b) shows the defined contact pads after the etching

Afterwards, the IV curve of the large contact was measured again, and compared to the original IV curve. The result can be seen in Fig. 3.19. It can be seen that the FIB procedure has significantly altered the IV curve for the InP chip as well, showing that it is not a problem with the GaSb material only. Again an extra parallel conduction path seems to be added to the diode. Additionally, the electrical isolation between the newly defined contacts and the original electrical contact was measured. The shallow etched contact could not be probed, while the deep etched contact could be probed. The measured resistance was  $6 \Omega$ , even lower than the measured isolation in the GaSb chip. Therefore, a more conventional etching method was used next to isolate an SA.

In order to be able to do this, the bond wires were removed from the chip using tweezers, a steady hand, and a stereo-microscope. Afterwards, the chip and the submount were coated with photoresist using a fine brush, taking extra care to cover the existing waveguide facets as well. Afterwards, using soft-contact mode on an MA6 mask aligner, an isolation etch was patterned in the photoresist, making sure the waveguide isolation etch would cut through the waveguide at a small angle. Using ICP etching, the metal stack and around 1 micron of the active material were etched away, resulting in an isolated section of the chip with a length of around  $100 \mu\text{m}$ . The resist was then washed off using acetone. Since the top surface of the electrical contact was already damaged due to removing the bond wires, it was



*Figure 3.19: IV curve of the InP gain chip before (dashed) and after (solid) the etching of an isolated contact. It can be seen that the diode performance has dropped significantly after the post-processing.*

opted to continue using the gain chip using only probe needles for making electrical connections. An image of the chip after the post-processing can be seen in Fig. 3.22. The conventional post-processing did significantly impact the IV curve of the diodes, with more parallel resistance showing in the IV curves for both the SA and the gain contact.

To analyze the gain chip performance after the post-processing, electro-optical measurements were done without coupling to an external cavity. When driving the maximum gain current, and forward biasing the SA at 1.3 V, it was possible to get the gain chip to lase on the residual reflection on the gain facet, which indicates that it has been damaged during or after the post-processing. The optical spectrum measured with these driving parameters can be seen in Fig. 3.20. The measured FSR shows the lasing cavity is between the rear facet of the gain chip and the angled facet or the tip of the lensed fiber. The possible parasitic cavities formed by the isolation etch were not visibly affecting the output spectrum of the laser, which means it is unlikely to break up the pulse during mode-locked lasing.

When reducing the bias on the SA to 0 V, there was not enough gain for self-lasing, and the measured ASE spectrum can be seen in Fig. 3.21.

Unfortunately, after this measurement, the probe contact was lost while the used SMU was in constant-current mode without a voltage limit set. Therefore the SMU increased the voltage, creating a spark between the probe and the gain contact. This broke the chip, and no other chips were available anymore.

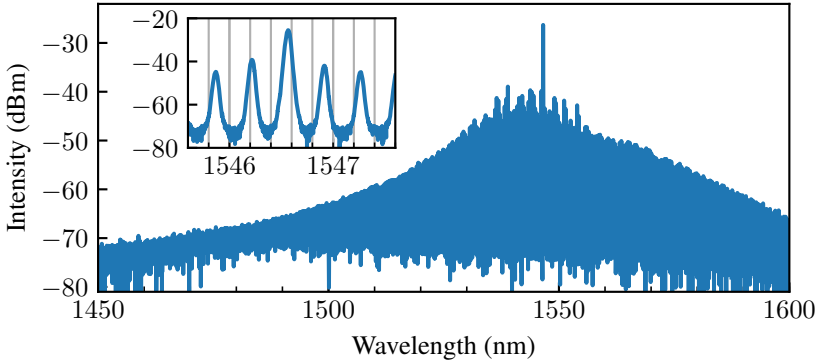


Figure 3.20: The spectrum of the SAF 1126 gain chip self-lasing after post-processing for a gain current of 350 mA and an absorber bias of +1.3 V.

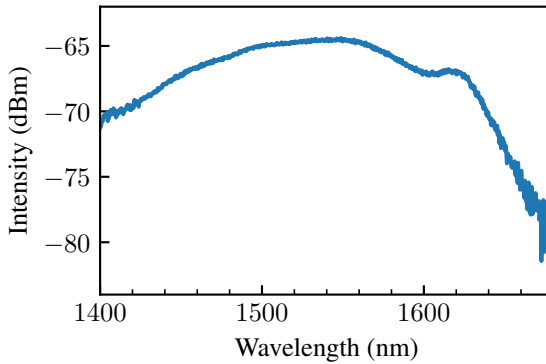
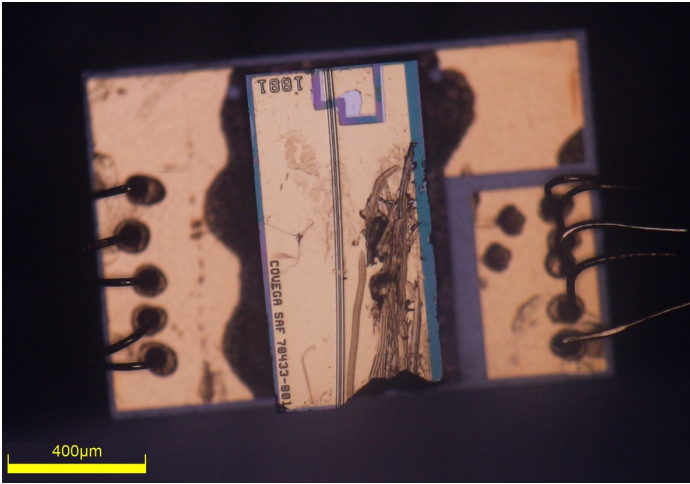


Figure 3.21: ASE spectrum of the SAF 1126 gain chip ASE after post-processing, for a gain current of 350 mA and an absorber bias of 0 V.

### 3.3.2 Innolume gain chips

From Innolume, two gain chips were acquired, with two different operating wavelengths. One chip was designed for 1180 nm emission, the other for 1310 nm emission.



*Figure 3.22: Image of the SAF 1126 gain chip after the post-processing steps. It can be seen the bond wires have been removed from the laser die, and a second contact pad and SOA section have been defined at the rear facet.*

### **1180 nm Innolume chip**

The 1180 nm gain chip from Innolume was bought because it was the only one immediately available with a saturable absorber. It was also the first gain chip with an SA that came delivered to the lab, and therefore the first chip that was used for butt-coupling to an external SiN cavity. An optical spectrum measured while using the external SiN cavity is shown in Fig. 3.23.

The measured spectrum shows a large ripple with a significantly larger FSR than the full cavity. The individual laser lines of the longitudinal modes could not be resolved by the OSA used. The ripple is caused by a parasitic resonator inside the laser cavity. This behaviour was independent of driving parameters. The resonance period is 1 nm. When using a group index of 4 inside the gain chip, this would point to a resonator length of 175 μm, which is exactly the length of the SA in the chip. This indicated the isolation etch between the SA and the gain section had a significant parasitic reflection, leading to a resonance between the isolation etch and the back facet HR reflector. Since the optical output spectrum was far from the ideal comb shape, experiments were continued using other gain chips.

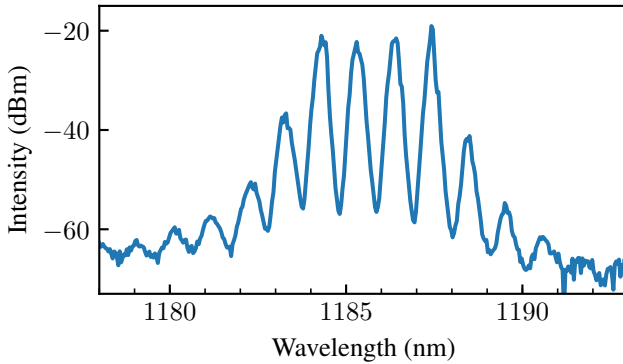


Figure 3.23: The optical spectrum of the 1180 nm Innolume external SiN cavity MLL at 500 mA, -2.41 V. The parasitic resonance with an FSR of 1 nm is caused by reflections between the back facet reflector and the SA isolation etch.

### 1310 nm Innolume chip

The second Innolume chip that was acquired was a chip emitting around 1310 nm. This chip did not have an SA. Due to the bad results with previous attempts at post-processing to define an SA contact, it was opted not to try this route. Therefore, it was attempted to make a self-mode-locked laser with an external SiN cavity as was also demonstrated in [4]. The results are described in section 4.3.

We had two of these gain chips available. Initially, a cavity chip could not be butt-coupled to either of them efficiently, since both chips could not make close contact due to a collision before the waveguide facets were touching each other. After inspection in the SEM it turned out that for both of the gain chips, the submounts caused the issue. As can be seen in Fig. 3.24, the laser die is mounted on the submount with a slight overhang, but the submount itself is not flat. Around 300  $\mu\text{m}$  below the top of the laser bar, there is a large bump on the submount, which is what the gain chip would collide with when trying to butt-couple. Therefore, the cavity chips used with this gain chip were thinned down further than usual, to 225  $\mu\text{m}$  thickness.

### 3.3.3 FBH gain chips

From FBH, two gain chips were acquired, both with an SA section. The difference between both chips is that one was fabricated with a straight facet combined with an optimized AR coating to prevent spurious reflections in the cavity. The other one

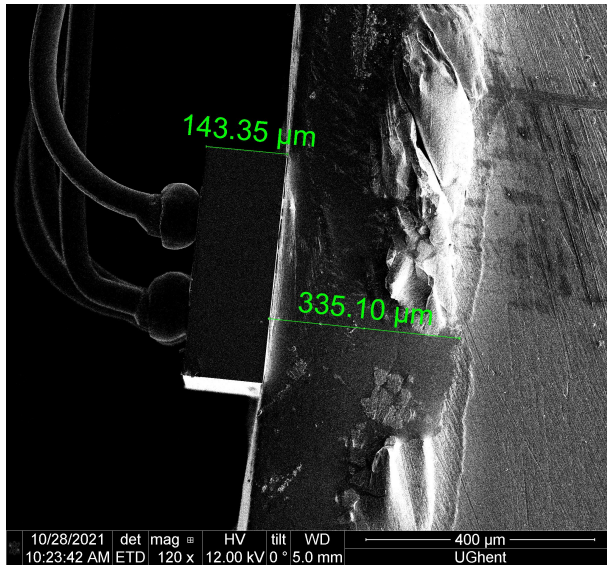


Figure 3.24: SEM image of the Innolume 1310 nm gain chip's mount, showing that the submount protrudes further than the laser die's facet around 300  $\mu\text{m}$  below the top of the die.

was fabricated with an angled facet and an AR coating optimized for transmission into air.

### Straight facet FBH chip

The first experiments were done with a chip with a straight facet, since these were already available at FBH. In order to decrease the spurious reflections back into the gain chip caused by a straight facet, the AR coating was optimized by FBH for the least reflections when coupling to the SU8 SSC on the cavity chips.

The material (and therefore refractive index) of the AR coating layers was fixed, since these were standardized in the coating process used. Therefore, only the layer thicknesses could be optimized.

In the optimization of the AR coating, a small air gap between the two chips could be considered a part of the AR coating, or it can be assumed that there will be no air gap in the system. Whether this can be achieved is dependent on the flatness of the facets of both chips and if the rotation of both chips relative to each other can be optimized completely.

It was opted to assume the air gap could be completely removed during the experiment, and the AR coating was optimized for the least reflection when coupled to

an SU8 SSC of the appropriate size for the best overlap between both modes. The thicknesses and refractive indices of the layers after the optimization performed by FBH were as shown in Table 3.1.

Layer	Thickness (nm)	Refractive index
1	10	1.8370
2	15	1.6589
3	78	2.3717

*Table 3.1: Optimized AR coating layer thicknesses and indices for the flat facet FBH gain chip.*

Simulating this AR coating in an EME simulation showed a reflection at the coupling interface of 0.006% from the gain chip waveguide and 0.03% from the cavity chip waveguide. The simulated transmission at the interface is 87.6%.

### **Angled facet FBH chip**

The experiments with the straight facet FBH chip showed no mode-locking at any of the tried operating conditions. This was attributed to the spurious reflections back into the waveguides caused by the straight facet since the AR coating is not perfect. Therefore, a second chip was fabricated with an output facet at an angle. The AR coating used on this chip was a standard coating optimized for the highest transmission into air.

A big advantage of this gain chip is that a laser with a straight, uncoated facet was also fabricated from the same wafer. This meant that a less complex laser with the same gain properties and known facet reflectivities could be used to compare the external cavity laser to. Unfortunately, there was still a small difference between the two gain chips in that the straight facet laser had no SA, while the angled facet gain chip did. Therefore, comparisons can only be made when the SA is connected in parallel to the gain section on the angled gain chip, but it gives the possibility to indirectly measure the coupling losses between the two chips, as will be shown in section 4.4.1.

## 3.4 Details of fabricated cavity chips

### 3.4.1 Design and simulation procedures

For every gain chip, the design of the cavity chip had to be slightly different. Firstly to match the mode size and emission angle of the gain chip used, and secondly to adjust the waveguide dimensions for the used wavelength. All chips used the same design elements and looked similar to the cavity chip shown in Fig. 3.25, which shows the cavity chip for the FBH gain chip.

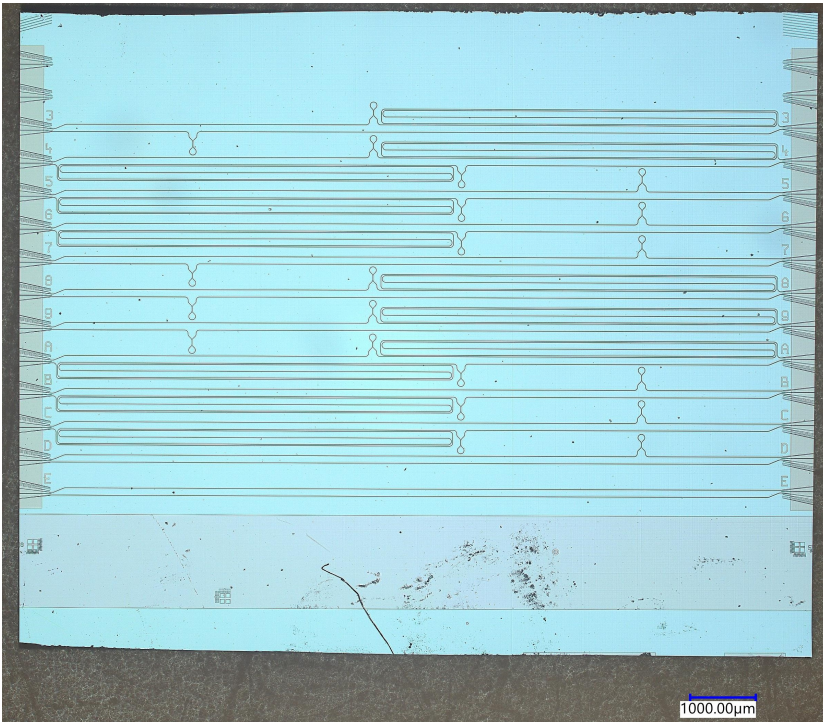


*Figure 3.25: Microscope image of the cavity chip used with the FBH gain chip. The measurements in this thesis were done for cavity number 4 on the right of this chip. The gain chip would be on the right of this image, and the lensed fiber on the left during those measurements.*

### SU8 SSC simulation

For the simulation of the SU8 coupler, two things need to be simulated. The mode overlap between the mode at the two facets and the taper structure that transitions

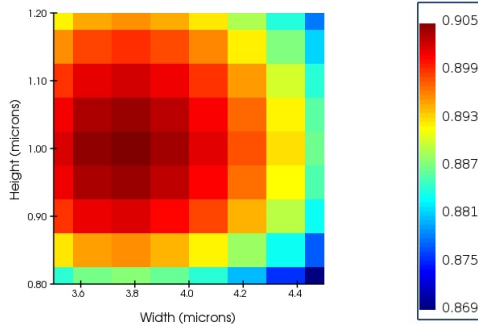


Figure 3.26: Simulation showing the overlap integral between the SMART gain chip output mode and the SU8 input mode for different widths and heights of the SU8 waveguide.

the mode between the SiN and SU8 waveguides. The mode-overlap simulation was done using the Finite-Difference Eigenmode (FDE) solver in Lumerical MODE, which can calculate the overlap integral between two different modes at their optimal alignment. The parameters of the SU8 that can be optimized are the width and height, both independently. Therefore a 2D sweep was performed to find the optimum dimensions of the SU8 waveguide. An example of such a sweep (done for the SMART laser) is given in Fig. 3.26. This same procedure was done for all acquired gain chips.

The second simulation for the SU8 coupler is the transition between the SU8 and SiN waveguide. The start and end waveguides are determined by the SiN width and the SU8 width and size. This means the only considerations are the length of the SiN inverted taper and the taper-tip width. The final taper-tip width was set by fabrication limitations (resist not falling over during development), and in this case was designed to be 150 nm for all cavities but the one for the FBH gain chip. That chip used 100 nm wide SiN taper-tips, which was enabled by improvements in the SiN patterning process, enabled by using proximity effect correction in the e-beam step.

Using an EME simulation, the length of the taper can very efficiently be swept to find an optimum value, therefore the EME solver of Lumerical MODE was used. In the end two different designs were used, depending on the SU8 coupler width. Either the SiN waveguide immediately tapered under the correct SU8 width waveguide (single-taper design), or the transition from SiN to SU8 was done in a 2  $\mu\text{m}$  wide SU8 waveguide, which then tapered up to the correct width (double-taper design). The single-taper design used an angled facet in simulation, but this was dropped for the double-taper design after it was clear from fabrication that the

45-degree angled tip shape did not pattern correctly during the lithography step.

An example of the simulation done for the taper length of the cavity used for the SMART chip (with a single-taper design) is shown in Fig. 3.27. It can be seen that the transmission is relatively flat for taper lengths above 30  $\mu\text{m}$ , ignoring the 2 percent-point oscillation, showing 30  $\mu\text{m}$  is the length for which the taper becomes adiabatic. This oscillation is caused by the fact that the SU8 waveguide in the SiN taper region is not completely single mode, and a small portion of the light is coupled to higher-order modes. In order to make sure that the fabricated device would also be adiabatic, a safety margin was taken, and a taper length of 50  $\mu\text{m}$  was chosen.

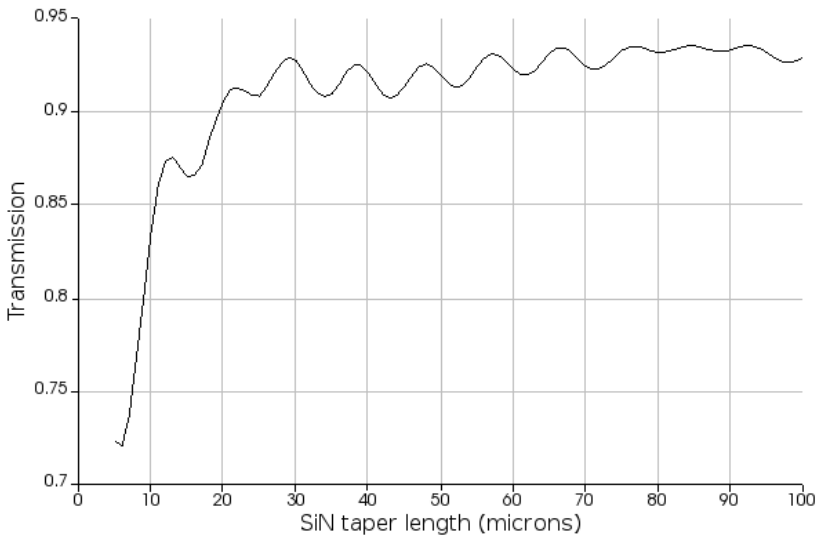


Figure 3.27: Example of the SiN single-taper length simulation done for the SMART cavity chip.

The SU8 coupler used for outcoupling from the cavity chip to the lensed fiber used an SU8 waveguide that was the same width for every design, of 3.5  $\mu\text{m}$ , which was simulated to have optimal coupling at a wavelength of 1550 nm. All the couplers used were defined on the same lithographic mask, which was reused for other wavelengths as well. The height of the SU8 waveguide for the fiber coupler was always the same as that for the chip-chip coupler since it is defined in the same lithography step.

To simulate the directional coupler to use for the Sagnac mirror, two simulations were performed, for the two different sections of a directional coupler. The amount of power coupling to the coupled output port of a directional coupler when light

power  $A$  is sent into one of the inputs is given by  $K = A \sin^2(k'L + k_0)$  [80], where  $k'$  is the coupling factor,  $L$  the length of the coupling section, and  $k_0$  the amount of coupling when the coupling section has zero length. The coupling ratio  $k_0$  caused by just the arms of the directional coupler was calculated using a Lumerical FDTD simulation of a directional coupler with a coupling section of  $0 \mu\text{m}$ , giving only the coupling factor caused by the bends in the directional coupler.

To simulate the coupling factor caused by the coupling section of the directional coupler, supermode-theory was used, following the derivation in [80]. Calculating the effective refractive index difference between the even and odd supermodes in the coupling section in Lumerical MODE allows to calculate the beat length between the two supermodes, and therefore the length of the directional coupler that would lead to the light coupling back and forth exactly once. From this the  $k'$  value can be calculated. Using the graph in Fig. 3.3, the correct directional coupler length can then be chosen for a desired reflectance. In all cases in this thesis, the targetted reflection was 70%, to make sure the cavity would still provide enough feedback for lasing, even if there were many other losses present. Since the fabrication process of the SiN waveguides shows quite some variance, often three different directional coupler lengths were used in the same fabrication run, to increase the chance of a working reflector being on the chip, which provides enough feedback for lasing, but also an amount of optical output power that would enable most characterization measurements without needing optical amplification.

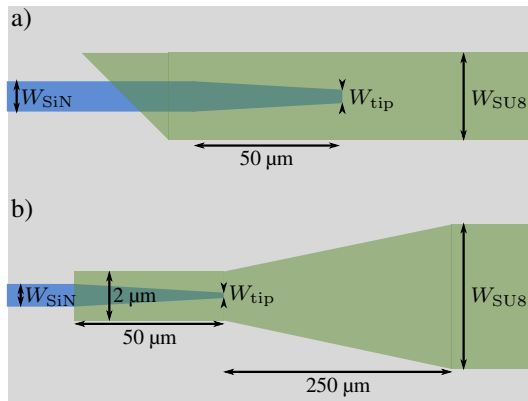


Figure 3.28: Schematic representation of both types of SiN to SU8 transition structures used. a) shows the single-stage taper, b) shows the double-stage taper. SiN is represented in blue, SU8 in green, and the  $\text{SiO}_2$  undercladding in gray.

### 3.4.2 Parameters of used chips

The design parameters used for the fabricated cavities and the gain chips used with them for all lasers that were measured are given in Table 3.2.

	FBH	Innolume A	Innolume B	SMART
Wavelength (nm)	1060	1180	1310	1550
SiN width ( $\mu\text{m}$ )	0.86	0.86	1.1	1.5
SiN tip width (nm)	100	150	150	150
SiN cavity lengths (cm)	0.3	1.0	0.2	0.1
	3.0	1.0	5.0	3.0
SU8 dimensions ( $\mu\text{m}$ )	$8.6 \times 1.6$	$11.5 \times 1.2$	$15.4 \times 1.3$	$3.8 \times 0.88$
SU8 angle at facet ( $^\circ$ )	6.7	10.9	10.9	15.2
Sagnac DC gap (nm)	270	210	270	270
Sagnac DC coupling lengths ( $\mu\text{m}$ )	35.0	13.5	25.0	23.0
	42.0	15.0	33.0	
	50.0	16.5	41.0	
SA length ( $\mu\text{m}$ )	200	175	-	50
Gain section (mm)	1.8	3.3	3.0	0.85
Output mode ( $\mu\text{m}$ )	$5.8 \times 2.1$	$5.6 \times 1.0$	$7.6 \times 1.1$	$3 \times 1.0$
Emission angle ( $^\circ$ )	10	17	17	23

Table 3.2: Design parameters of the cavity chips that were fabricated and the gain chips they were combined with to make ECMLLs.



# 4

## Characterization of hybrid-integrated extended cavity MLLs

---

<b>4.1</b>	<b>Aligning gain and cavity chips . . . . .</b>	<b>72</b>
4.1.1	Permanent butt-coupling . . . . .	72
4.1.2	Non-permanent butt-coupling setup . . . . .	73
<b>4.2</b>	<b>Mode-locked laser using the SMART MPW gain chip . . . . .</b>	<b>75</b>
4.2.1	Short laser cavity . . . . .	77
4.2.2	Long laser cavity . . . . .	79
<b>4.3</b>	<b>Self mode-locked laser . . . . .</b>	<b>82</b>
<b>4.4</b>	<b>Mode-locked laser at 1064 nm . . . . .</b>	<b>84</b>
4.4.1	Chip-Chip coupling loss . . . . .	84
4.4.2	LI curves . . . . .	86
4.4.3	Mode-locking points . . . . .	87
4.4.4	Heterodyne optical linewidth measurement . . . . .	89
4.4.5	Injection locking . . . . .	92
<b>4.5</b>	<b>Comparison of demonstrated integrated ECMLLs . . . . .</b>	<b>99</b>
4.5.1	Comparison of the presented 1550 nm and 1064 nm MLLs . . . . .	99
4.5.2	Comparison to other demonstrated hybrid integrated ECMLLs . . . . .	100

---

## 4.1 Aligning gain and cavity chips

A crucial part of making a system from two separate chips is the butt-coupling between them. The mode sizes in the chips I fabricated are a few microns wide, and at most 2 microns high. This requires very precise alignment. Any small misalignment will increase the coupling loss, and since this loss is part of the laser cavity it would decrease the laser's noise performance. The butt-coupling can be done in two ways: Permanent, or non-permanent. The permanent option is seen as part of the packaging process of chips and is offered as a service by at least one external company. The non-permanent option makes use of a measurement setup with precise and stable stages to align the chips. First, a short section will be dedicated to the permanent option. This is followed by a longer section about the non-permanent option, which was used in this work.

### 4.1.1 Permanent butt-coupling

It is possible to permanently butt-couple two chips, but it's a technique that was not used in this work because it means that both a new gain chip and a new cavity chip need to be used for every different laser that is experimented with. As only the cavities were made in-house, and the gain chips had to be bought, this would make it very costly to try several different cavities with the same gain chip.

At least one company (PhiX, Enschede, NL) offers services for the permanent butt-coupling of two chips. In this case, both chips are mounted on individual submounts, and a drop of glue is applied between the two submounts, while the chips are actively aligned. When the alignment is optimal, the glue is cured to bond the two chips together.

### Photonic wire bonding

A second option for permanently integrating the two chips together is through photonic wire bonding [20]. Using this technique, both chips are mounted to the same submount, but only coarsely aligned. The optical connection between the two chips is then made using a photonic wire bond that is made from a photosensitive polymer. The uncured polymer is applied to a large region covering both chips, and the parts that should become waveguide are exposed using a tightly focused high-intensity computer-controlled laser that can write 3D shapes by controlling the X-Y position and focus depth of the laser spot. Using this method, many different types of waveguides can be connected together. The transition between the on-chip waveguide and the polymer waveguide can either be an adiabatic transition on the

surface of the chip or abruptly at the facet of a chip.

### 4.1.2 Non-permanent butt-coupling setup

Non-permanent butt-coupling is the technique used in this work, specifically using 2 computer-controlled XYZ piezo stages. In this case, the alignment of three different components was necessary: The gain chip, the cavity chip, and the outcoupling lensed fiber. The gain and cavity chip need to be most stable relative to each other since any instability in the positioning of these two will show up as extra noise in the laser cavity itself. The alignment of the lensed fiber to the cavity is less critical since it will only impact the measurement, and not the laser performance itself. For this reason, it was chosen to keep one of the two chips at a fixed position and put the other chip on one of the piezo stages. The lensed fiber would then be on the second piezo stage. Two schemes were considered, one where the cavity chip was fixed, and the other where the gain chip was fixed.

To keep the alignment procedure simple, it would be easiest to put the cavity chip at a fixed position and move the gain chip and the lensed fiber relative to the cavity chip. In this way, changing the alignment between the gain chip and the cavity chip does not change the alignment between the lensed fiber and the cavity chip. The disadvantage of this method is that the gain chip has to be mounted on the piezo stage, together with the TEC, the heatsink, and the electrical connections that need to run to it. This would require a very light solution for the cooling system as well, to stay within the rated load of the piezo stage in the vertical direction.

Therefore, it was opted to fix the position of the gain chip, meaning the weight of the cooling system and all the electrical connections could be made without regard for weight or movement ranges. The cavity chip would then be on a piezo stage. This does come with the problem that changing the alignment between the cavity chip and the gain chip can only be done by moving the cavity chip, therefore also changing the alignment with the lensed fiber. Fortunately, if the angle between the lensed fiber and the cavity chip is known, this can be compensated for in software, since the piezo stages are computer-controlled. In this case, the lensed fiber will move in sync with the cavity chip when desired.

To enable the measurement of cavity chips with different angles for the outcoupling waveguide, the lensed fiber stage was placed on a rotation stage. This also made it possible to move the lensed fiber far away from the cavity chuck while changing chips, more than with just the travel range of the XYZ stage. An image of the final setup is shown in Fig. 4.1

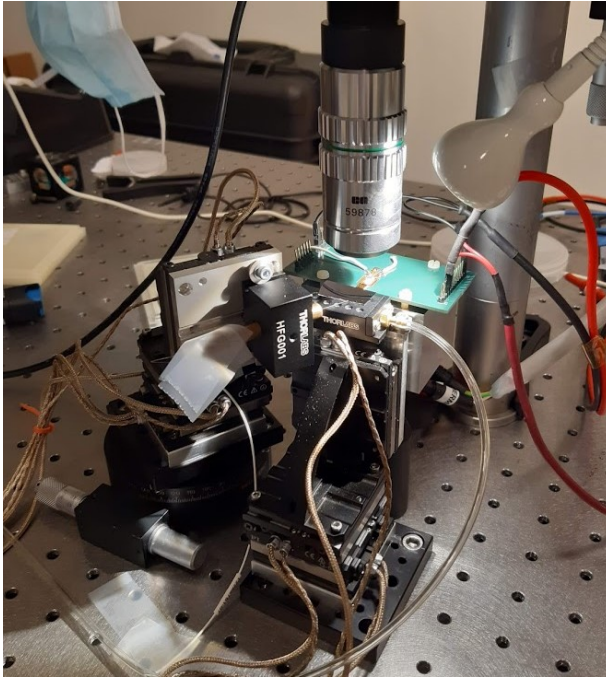


*Figure 4.1: An image of the butt coupling setup while it was used to measure the lasers with the SMART chip. The green PCB has the gain chip mounted on top of it. In front of that is the cavity chip on an XYZ stage. To the left of this, the lensed fiber is placed on an XYZ stage which is placed on a rotation stage. The lens above the setup gives a 20x magnification.*

### **Alignment procedure**

Before the characterization of the lasers, the two chips and the lensed fiber for outcoupling have to be aligned. This takes a few steps after the gain chip is mounted in the setup.

1. Before loading the cavity chip onto the chuck, rotate the lensed fiber away so there's space to move the chuck as far away from the gain chip as possible.
2. Put the cavity chip on the chuck using tweezers with the smallest angle difference to the gain chip as feasible.
3. by looking at the chips directly, bring the two chips together coarsely.
4. Find both the gain chip and the cavity chip facet using the microscope, and bring them to almost touch.

5. If the angle between both facets is not flat, move the cavity chip into the gain chip with small steps of less than 5  $\mu\text{m}$ . The chips will touch, and the force from the gain chip will rotate the cavity chip on the chuck. This can be seen as features on the cavity chip moving left or right relative to the gain chip. Once the features stop moving, the facets are aligned.
6. Visually align the facets in the two directions that can be seen on the camera.
7. Turn on the gain section and bias the SA section. The height of the cavity chip can now be tuned to maximize the current in the SA, which is acting as an in-cavity photodiode. Improving the alignment between both chips will also increase the feedback, and therefore intracavity power.
8. Rotate the outcoupling lensed fiber to the correct angle, and align for the highest amount of outcoupled power.
9. Once the lensed fiber is aligned, lock the movement of the fiber and the cavity chip together in the software to make adjusting for the optimal alignment easier.

## 4.2 Mode-locked laser using the SMART MPW gain chip

For the MPW gain chips, a custom fanout PCB was designed to route all the bond pads at the edge of the chip to pin headers for easy swapping between different lasers on the same chip. A view of the PCB used for the SMART gain chip can be seen in Fig. 4.2. In order to control the temperature of the gain chip, the PCB also has to serve as a heat sink that is temperature controlled using a TEC. Therefore, both the top and bottom copper layers were exposed where the chip was mounted, and they were thermally connected using via's. The PCB was then mounted to a hot-side heatsink with a TEC sandwiched in between the PCB and the hot-side heatsink. Nylon screws were used to prevent a direct thermal connection between the PCB and the hot-side heatsink. The TEC was kept in place using the mounting pressure. The chip and a thermistor were mounted to the top side of the PCB using silver epoxy. The chip was mounted with a slight overhang off the PCB of around 20  $\mu\text{m}$ .

On the SMART MLL chip, both ring laser and Fabry-Pérot (FP) lasers were available. Only the FP architecture laser has been measured, which was chosen because it meant only one waveguide had to be aligned, reducing the sensitivity to the difference in the leveling between both chips. On the cavity chip, both short and long cavities were made, with the same mirrors. Both these cavities were

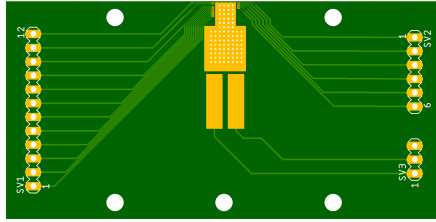


Figure 4.2: Image of the PCB design for the SMART MPW chip. The chip is mounted on the top of the image, with the optical facets pointing away from the PCB. The two large pads are for soldering the thermistor leads to the board.

coupled to the same gain section on the gain chip. All differences between the lasers are therefore only caused by the difference in the cavities used. During all measurements, the temperature of the PCB heatsink was kept at 20 °C. An image of the two chips aligned for the measurement of the short cavity laser can be seen in Fig. 4.3.

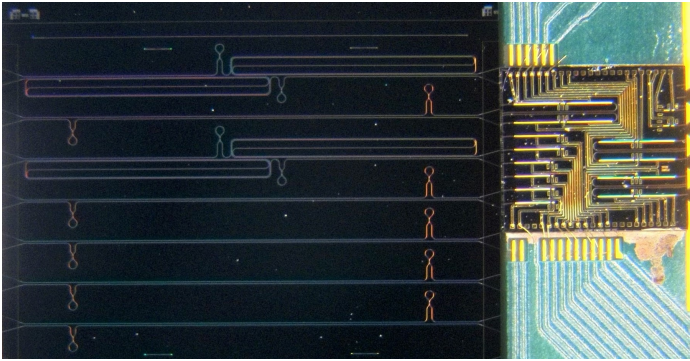


Figure 4.3: Image of the SMART laser where a short cavity on the SiN chip (on the left) is coupled to the second laser structure from the bottom on the SMART chip (on the right). This is the configuration used in section 4.2.1.

Firstly, an LI curve was made for both the short and the long cavity, which is shown in Fig. 4.4. For both these measurements, the SA bias was 0 V. It can be seen that the long cavity has a slightly higher threshold current than the short cavity, suggesting that the added propagation loss from the longer cavity is negligible. The maximum recorded output power is 0.45 mW coupled into the lensed fiber. This is limited by the saturation power of the Semiconductor Optical Amplifier (SOA) used in the SMART platform, which is optimized for high gain instead of high output power.

Afterwards, the lasers were measured in the mode-locking regime. The mode-

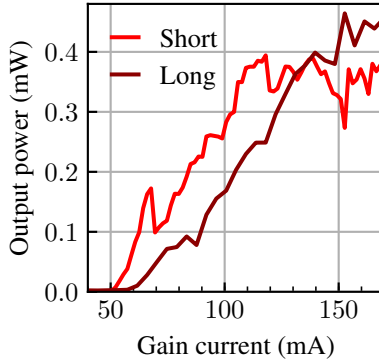


Figure 4.4: LI curves of the SMART laser coupled to a short and a long cavity. The recorded power is the power in the lensed fiber used for outcoupling.

locking operating parameters were investigated, as well as the laser performance at the optimal operating point.

### 4.2.1 Short laser cavity

The short cavity was coupled to the gain chip, and the gain current and SA bias were manually swept through the allowed ranges in large steps, to coarsely identify the operating parameters where mode-locking occurs. This analysis was done solely by looking at the optical spectrum of the laser. Afterwards, an automatic sweep was done, around the points where mode-locking was detected. For increasing gain currents, the SA bias voltage was swept from most negative to least negative before going to the next gain current. This was chosen because mode-locking is often started at a high reverse bias, after which the bias can be reduced without losing mode-locking [81]. At every point in the sweep the optical spectrum, a large span RF spectrum, and a zoom on the highest-intensity RF peak was saved. Optical powers could then be calculated for every measurement by integrating the optical spectrum. The results of this sweep can be seen in Fig. 4.5.

For this laser, only fundamental harmonic mode-locking was detected, at a frequency of 15.5 GHz. Mode-locking was found at a large range of operating parameters which are all the operating points where the RF peak power does not clip to the minimum color in Fig. 4.5 b). In these measurements, there is an RF line at the fundamental repetition rate frequency of the cavity.. The optimal point was chosen as the point where the RF linewidth, determined by fitting a Voigt shape, was the smallest. At the optimal point, the optical spectrum and a zoom on the RF

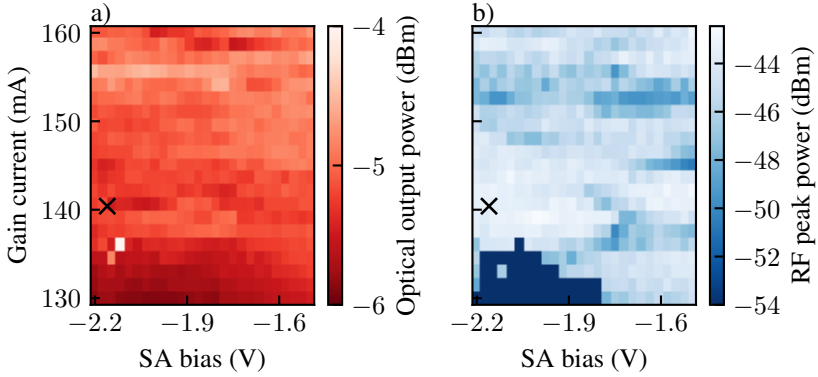


Figure 4.5: The mode-locking maps of the laser with the short cavity as a function of gain current and SA bias voltage. a) shows the optical output power. b) shows the power of the strongest RF peak. The cross shows the optimal operating point.

peak can be seen in Fig. 4.6. A Voigt profile was fit to the measurement data of the RF peak, indicating a -10 dB linewidth of 940 kHz.

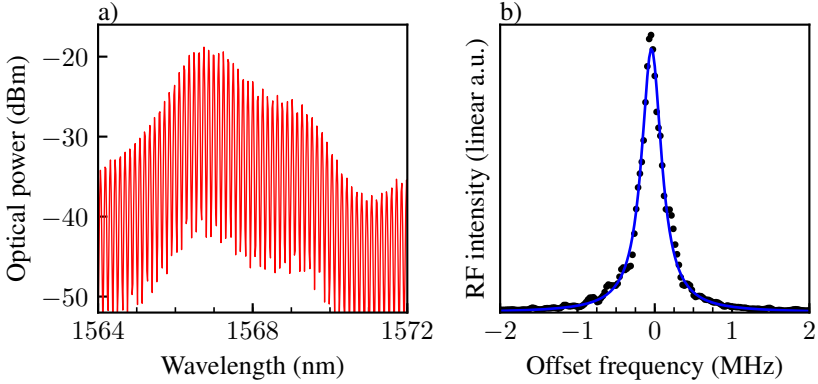


Figure 4.6: a) shows the optical spectrum and b) shows a zoom on the RF beat note at the optimal operating point of the SMART laser coupled to a short cavity. The black markers in b) indicate the measured data points, and the blue line is a Voigt fit of the peak, with a -10 dB width of 940 kHz.

An autocorrelation trace was also measured. In order to have a detectable signal, the laser output was first amplified using an Erbium Doped Fiber Amplifier (EDFA), before being sent into the APE PulseCheck 150 autocorrelator. The measured

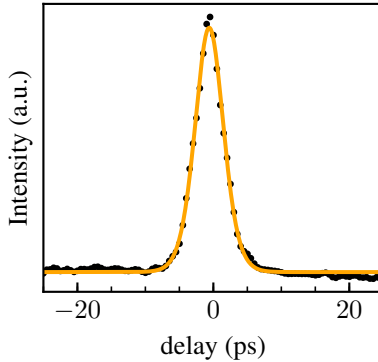


Figure 4.7: Autocorrelation trace data (black markers) and 3.1 ps  $\text{sech}^2$  pulse fit of the SMART laser coupled to a short cavity.

autocorrelation trace can be seen in Fig. 4.7. The autocorrelation function of a  $\text{sech}^2$  pulse ( $\frac{3(\tau \cosh(\tau) - \sinh(\tau))}{\sinh^3(\tau)}$  [82]) was fitted to the data, showing an FWHM of 4.8 ps. Using the deconvolution factor of 1.543 for a  $\text{sech}^2$  pulse [82] this means the pulse itself has a pulse width of 3.1 ps.

## 4.2.2 Long laser cavity

For the long laser cavity, the same procedure was performed as for the short laser cavity. The mode-locking maps can be seen in Fig. 4.8. In this laser, mode-locking was detected at the fundamental cavity frequency (2.18 GHz) and the first harmonic frequency (4.36 GHz), as well as Q-switching. In the RF peak-power map, the boundaries between the three regions are indicated. As expected, for increasing gain current, the laser switches from Q-switching to fundamental mode-locking to second harmonic mode-locking. The optimal operating point was chosen as the point where fundamental mode-locking occurs with the lowest RF linewidth.

The Optical spectra and the large-span RF spectrum at the optimal operating point can be seen in Fig. 4.9. It can be seen from the optical spectrum that the laser's FSR is below the resolution of the OSA (30 pm), since no individual comb lines can be seen. The RF spectrum also shows a very flat response, with the fundamental and all harmonics having the same intensity, indicating stable mode-locking [77].

Since the RF linewidth was so narrow that it was not easily resolvable in the normal sweeping mode of the ESA, the phase-noise mode was used to measure the phase noise in the fundamental peak in the RF spectrum. The measurement is shown

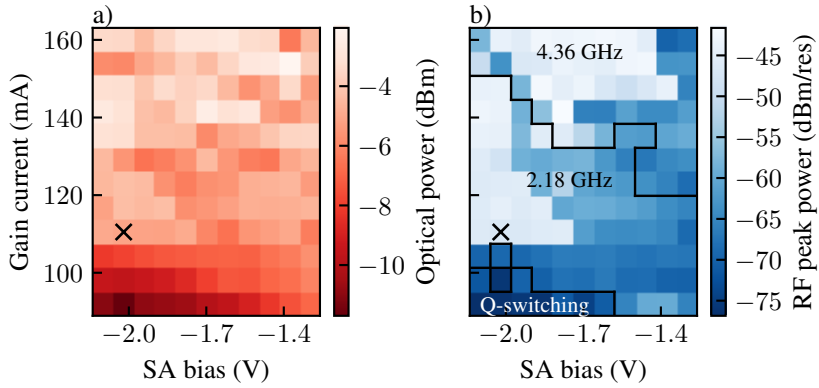


Figure 4.8: The mode-locking maps of the laser with the long cavity as a function of gain current and SA bias voltage. a) shows the optical output power. b) shows the power of the strongest RF peak and boundaries between mode-locking regimes. The cross shows the optimal operating point.

in Fig. 4.10. It can be seen that most of the phase noise spectrum makes a slope of -20 dB/decade, indicating that this noise has a Lorentzian lineshape, which is the expected shape caused by fundamental noise sources in MLLs [65]. This Lorentzian shape was fitted and indicated a fundamental RF linewidth of 31 Hz.

The autocorrelation trace was also measured, again using an EDFA to amplify the laser signal to a detectable level. The autocorrelation trace is shown in Fig. 4.10. The same calculation as used for the short cavity was used, indicating a pulse width of 6.3 ps.

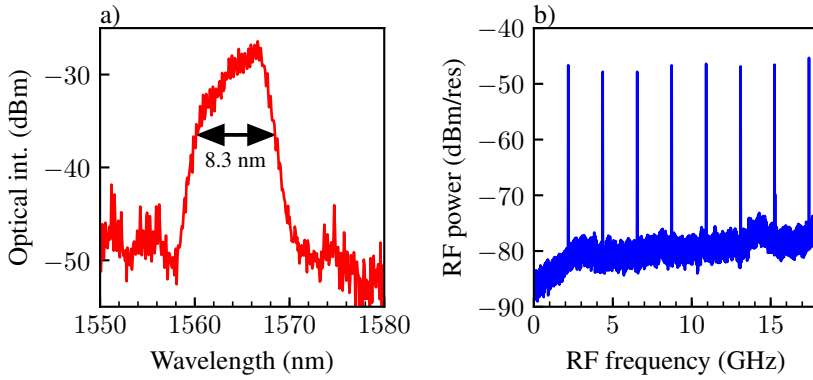


Figure 4.9: a) shows the optical spectrum and b) shows the RF spectrum at the optimal operating point of the SMART laser coupled to a long cavity.

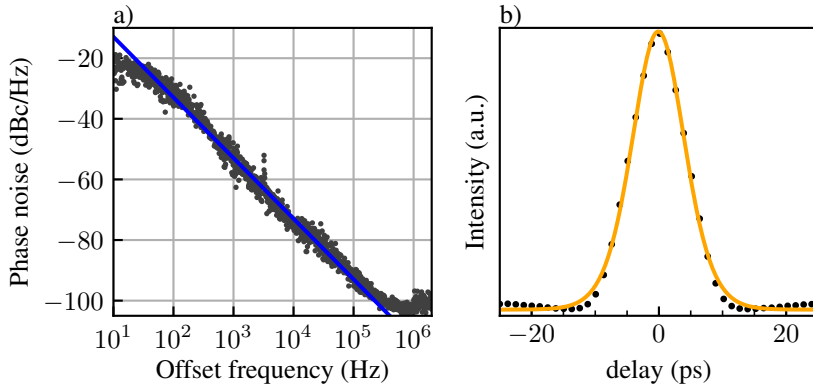


Figure 4.10: a) Phase noise with a 31 Hz Lorentzian fit (blue) and b) Autocorrelation trace of the SMART laser coupled to a long cavity, with a 6.3 ps fit (orange).

### 4.3 Self mode-locked laser

For the Innolume 1310 gain chip, a SiN cavity chip was made with many different cavities, with two different lengths, and three different Sagnac mirrors. This was done to increase the chance of finding a mode-locking point since the SA bias could not be varied during the experiments as an extra tuning parameter.

The LI curves of two different laser cavities coupled to the same gain chip are shown in Fig. 4.11. The only difference between these two lasers is the external cavity length. It can be seen that the LI curve for the short cavity laser has a complex behaviour, not dissimilar from the LI curve measured in a very similar laser in [4].

The shape of the spectrum however is very different from the work in [4], showing much more of a chaotic multi-mode laser characteristic, and less of the pedestal shape that usually indicates mode-locking. Additionally, for all six cavity variations, and all gain currents tested, an RF beat note could never be measured.

Since there is a possibility that the comb is FM-modelocked, 1 km of SMF28 fiber was added between the laser and the photodiode, to add dispersion to the system. In case the output spectrum is a perfectly flat FM-modulated comb, this would bunch the light up in the time domain. Since the center wavelength of the comb increases more than 5 nm with increasing gain current, there will be an operating point where the comb is significantly far from the 0-dispersion wavelength, even though it's near 1310 nm. Since the 0-dispersion slope is below  $0.092 \text{ ps}/(\text{nm}^2\text{km})$ , and the comb bandwidth is around 10 nm, a dispersion of 2.3 ps is the minimum value if the zero-dispersion wavelength was exactly in the center of the measured wavelengths. Even with this added dispersion, no RF beat notes were measured with any of the tried operating parameters, indicating that significant mode-locking does not happen.

Most likely, the dispersion inside the laser cavity is not correct for self-mode-locking to occur. There is no section in the laser that has any anomalous dispersion that could counteract normal dispersion in the SOA section of the laser. A well-designed Bragg grating could be used to introduce anomalous dispersion in the currently used SiN platform, or a platform with a thicker SiN layer could be used to fabricate waveguides with anomalous dispersion, which could then be combined with a Sagnac mirror while still having a net anomalous dispersion from the external cavity.

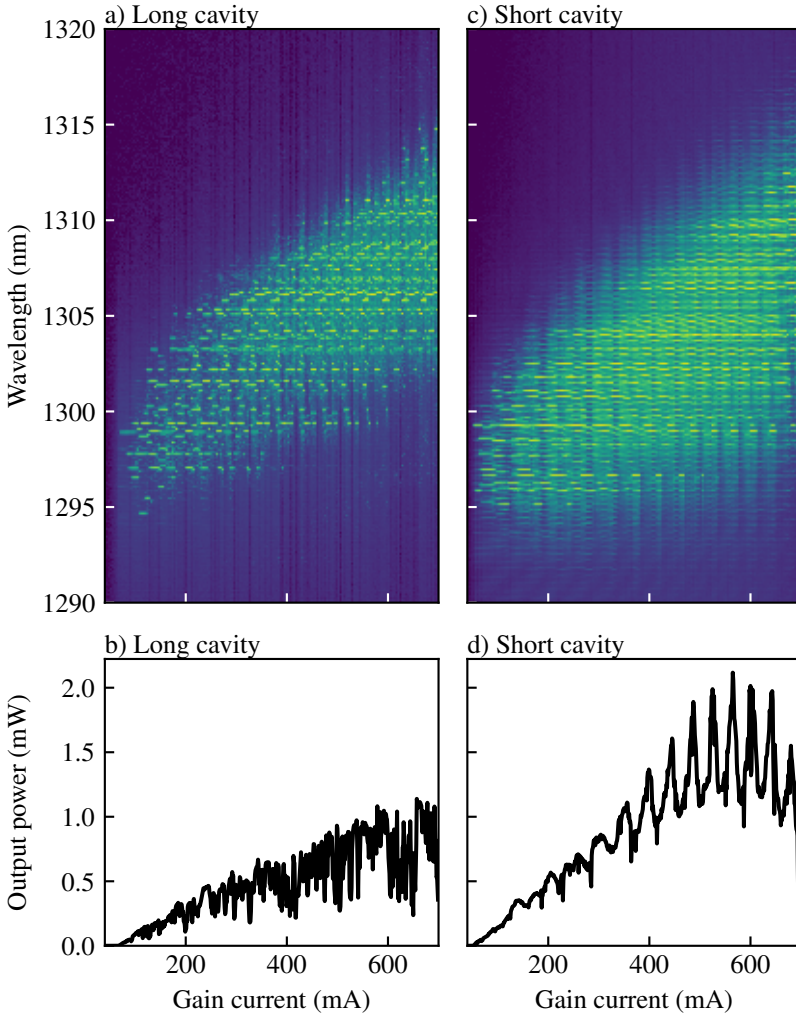


Figure 4.11: LI curve and optical spectrum as a function of gain current for both the 1310 nm laser with a long cavity (a and b), and with a short cavity (c and d).

## 4.4 Mode-locked laser at 1064 nm

### 4.4.1 Chip-Chip coupling loss

For this mode-locked laser, a lot of information was available about the gain chip, since it was made by the collaborating research institute FBH. The most useful was a laser bar made with a straight as-cleaved low-reflection facet, the same high-reflectivity HR rear facet, and the same total length as the gain chip used in the mode-locked laser. No SA was defined in this simple laser. The LI curve of this laser is shown in Figure 4.12, and shows a threshold current of 22 mA and a slope efficiency of 0.87 W/A. By connecting the gain section and SA section in the Extended Cavity Mode-Locked Laser (ECMLL) in parallel, the LI curve of the ECMLL under test can be compared to that of the simple laser. If the threshold currents are the same, it is known that the extended cavity gives the same amount of feedback as the LR facet of the as-cleaved laser bar which is a known value of 30%. If all other losses on the cavity chip are known, this makes it possible to calculate the coupling loss between the gain chip and the cavity chip.

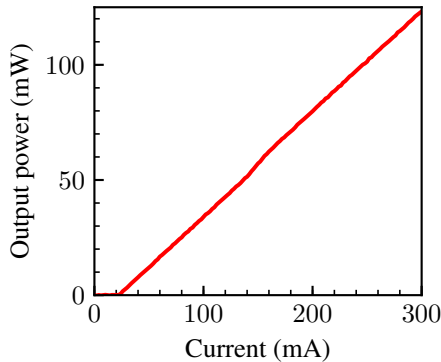


Figure 4.12: LI curve of the as-cleaved laser from the FBH epitaxial material.

On the external cavity chip, long and short cavities were made, with lengths of around 3 cm and 0.3 cm respectively, where for both lengths three different variants of a Sagnac mirror were fabricated, with differing amounts of reflection. All of these cavities were coupled to the gain chip, and the cavity with the closest operating threshold current to the as-cleaved laser had a threshold current of 25 mA. When assuming the threshold currents are the same, this means the coupled cavity chip gives the same amount of optical feedback to the gain chip as the as-cleaved facet. Together with the slope efficiencies of both LI curves, a system of two equations can

be solved, for two unknowns. All on-chip losses on the cavity chip were determined beforehand using test structures, but the mirror reflection was still used as a free parameter in the system of equations since it's the component in the cavity that is most influenced by small fabrication variations.

The measured slope efficiencies are 0.87 W/A and 0.064 W/A for the simple laser and the integrated laser respectively. The simple laser was measured using an integrating sphere and is therefore already normalized. The light from the ECMLL was coupled out using a lensed fiber. The coupling efficiency was measured using separate test structures and was 1.68 dB. Between the output coupler and the Sagnac reflector was 0.88 cm of waveguide with a propagation loss of 1.26 dB/cm, for a total loss of 1.11 dB. Normalizing for this, the actual slope efficiency calculated right after the reflector is  $0.064 \times 10^{(1.68+1.11)/10} = 0.127$  W/A.

The first equation in the system gives the amount of feedback  $F$  given by the cavity chip as a function of coupling loss and mirror reflection. It is built up from the chip-chip coupler loss  $L_{CC}$ , the propagation loss of the 0.2 cm in-cavity waveguide between the coupler and the reflector  $L_{cav}$ , and the mirror reflection  $R$ :

$$F = L_{CC}^2 L_{cav}^2 R$$

The two loss terms are squared, because the light has to pass them twice during a roundtrip. Since both lasers have the same threshold current, the feedback  $F$  is the same for both measured lasers.

The second equation makes use of the fact that the light intensity right before exiting the gain chip will also be the same for both lasers, making the intra-cavity slope efficiency  $E_{gain}$  the same in both lasers. This equation relates  $E_{gain}$  of the laser to the actually measured slope efficiency of the entire laser, taking into account the losses from  $R$ ,  $L_{CC}$ , and  $L_{cav}$ :

$$E_{gain} = \frac{E_{out}}{L_{cav} L_{CC} (1 - R)}$$

The loss terms are not squared in this expression since the light only passes them once when it is coupled out from the cavity. Both these equations use linear values for the losses. Therefore  $L_{cav} = 0.943$ , for 0.2 cm of waveguide with 1.26 dB/cm loss.

Both the feedback  $F$  and  $E_{gain}$  can be calculated from the simple Fabry-Pèrot laser. The feedback  $F$  is calculated from the Fresnel reflection at the as-cleaved facet, for an effective mode index  $n_1 = 3.33$  and  $n_2 = 1$  for air:

$$F = \left( \frac{n_1 - n_2}{n_1 + n_2} \right)^2 = 0.30$$

The factor  $E_{\text{gain}}$  can be calculated for the same laser by dividing the measured slope efficiency by the mirror transmission ( $1 - F$ ), giving the intra-cavity slope efficiency right before the gain chip facet:

$$E_{\text{gain}} = \frac{0.87 \text{ W/A}}{(1 - 0.3)} = 1.24 \text{ W/A}$$

These calculated values will have to be the same in the case of the ECMLL (when the threshold current is the same). Therefore, the only two unknowns left in the two equations for the ECMLL after filling in the known values are  $L_{CC}$  and  $R$ :

$$F = 0.3 = 0.943^2 L_{CC}^2 R$$

$$E_{\text{gain}} = 1.24 = \frac{0.127}{0.943 L_{CC} (1 - R)}$$

Solving this system of equations leads to two mathematical solutions:  $L_{CC} = -0.529$ ,  $R = 1.205$  and  $L_{CC} = 0.638$ ,  $R = 0.83$ . Of course, only the second solution is a physical one, with both positive coupling loss and a reflection between 0 and 1. Therefore:

$$L_{CC} = 0.638, R = 0.83$$

The mirror reflection of 83% is close to the targeted reflection of 75%, with the difference being attributed to the imprecise control of the etch depth during processing. The chip-chip coupling factor of 0.638 translates to a single pass coupling of  $10 \log_{10}(0.638) = -1.95$  dB. The simulated coupling loss was 0.84 dB, meaning 1.11 dB of extra unsimulated losses are added. This is attributed to waveguide and facet roughness, misalignment of the taper structure, and the small amount of space that's left between the facets.

#### 4.4.2 LI curves

The mode-locked laser of interest was the one with the longer cavity, to reach the lowest repetition rates. Therefore, all characterization that did not have to do with the coupling loss extraction was done for the longest laser cavity. The longer laser cavity had a designed repetition rate of 2 GHz. Initially, LI curves were measured for the laser for several absorber bias voltages. The results are shown in Fig. 4.13. The measurements show the expected behaviour, where the threshold current of the laser increases with increasing negative bias on the SA. The maximum output power measured was 3 mW. Mode-locking was not observed at any of the operating conditions in this measurement.

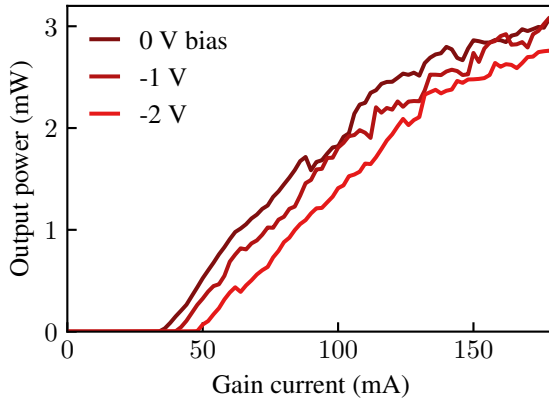


Figure 4.13: LI curves for the long cavity FBH laser for different SA bias voltages.

### 4.4.3 Mode-locking points

Initially, the gain-current and SA bias were swept over a large range while manually looking at the optical spectrum and RF spectrum on the OSA and ESA connected to the setup. From this, 2 regions of stable mode-locking were found. One of the points showed mode-locking at the second cavity harmonic at 4.06 GHz (called the 4 GHz point from here on). The second point showed mode-locking at the third cavity harmonic at 6.09 GHz (6 GHz point from here on). A finer sweep was done around the located points automatically, saving both the optical spectrum and the RF spectrum at every point. The optical output power and the peak RF power are shown as a function of the operating parameters for both the 4 GHz and 6 GHz operating points in Fig. 4.14.

In these maps, the bright areas show the operating points where mode-locking did occur, as indicated by both the increase in RF power and the increase in optical output power. The Rf peak power increases because of the pulsed output during mode-locking, and the optical output power increases because the SA absorbs a smaller portion of the light in the cavity when it is saturated during every pass of the optical pulse. In the 4 GHz map, a dark horizontal patch shows up at 105 mA gain current. Between 104 and 106 mA the optical spectrum jumps 2 nm to the red side. In between this jump, no stable mode-locking could be detected. Optical spectra at 104, 105, and 106 mA at -2.74 V are shown in Fig. 4.15.

Two optimal operating points were chosen from the points measured in the mode-locking maps, one for 4 GHz and one for 6 GHz. Since all measured operating points showed residual RF power at the fundamental cavity repetition rate, the

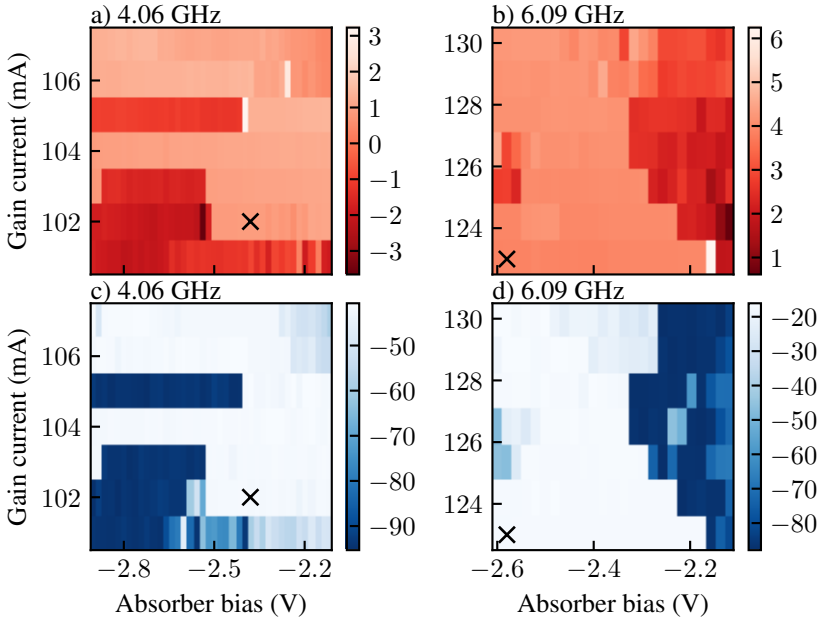


Figure 4.14: The mode-locking maps at the 4 and 6 GHz operating points. a) and c) show the optical output power in dBm for the 4 and 6 GHz operating points respectively. b) and d) show the RF peak power in dBm for the 4 and 6 GHz operating points respectively. The crosses indicate the chosen optimal operating point, where the residual amplitude modulation intensity was the lowest.

optimal point was defined as the location with the lowest power in the RF peak at the fundamental cavity repetition rate of 2.03 GHz. The optical and RF spectra at both these operating points are shown in Fig. 4.16. In Fig. 4.17, the phase noise and optical pulse width measurements are shown. The extracted ASE-limited RF linewidth from this measurement is below 1.7 Hz. The extracted optical pulse width is a  $6.03 \text{ ps sech}^2$  pulse.

No mode-locking point at the fundamental repetition frequency was found. Often, harmonic mode-locking is found at higher gain currents than fundamental frequency mode-locking. It is known, that higher-order harmonic mode-locking appears with increasing gain current due to the rise of the unsaturated gain [25]. We think that the absence of fundamental mode-locking is caused by a combination of several parameters such as the dependence of the modal gain on the carrier density, the carrier lifetime in the SA, and the round-trip time which prevent the existence of a suitable net gain window for fundamental mode-locking but still enables

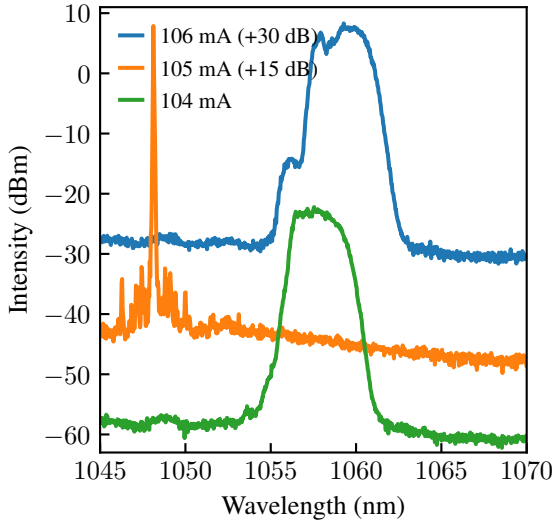


Figure 4.15: The optical spectrum of the MLL at the same absorber bias, but for different gain currents, showing a discontinuity in the mode-locking map. Mode-locking does occur at 104 and 106 mA (both at 4.06 GHz) but not at 105 mA.

higher-harmonic mode locking [83].

#### 4.4.4 Heterodyne optical linewidth measurement

In order to measure the linewidth of single-mode lasers, off-the-shelf measurement equipment is available. In our lab, there is an OEwaves 4000 tool that can do this. Unfortunately, the manual explicitly states this tool can be used for CW laser characterization, and it's unclear whether the detectors inside the machine could handle pulsed light. Therefore, the risk of using the equipment for an optical linewidth measurement of these MLLs was not taken, and a heterodyne measurement was performed.

At the 6 GHz operating point, a second laser was available that overlapped with the optical spectrum of the MLL under test. Therefore, a heterodyne measurement could be done to measure the optical linewidth. The external laser used was a Koheras Adjustik Y10 from NKT Photonics, a fiber laser emitting near 1064 nm. The datasheet specifies the maximum optical linewidth as 160 KHz FWHM over 120  $\mu$ s.

In a heterodyne measurement, the output of the laser under test and the reference

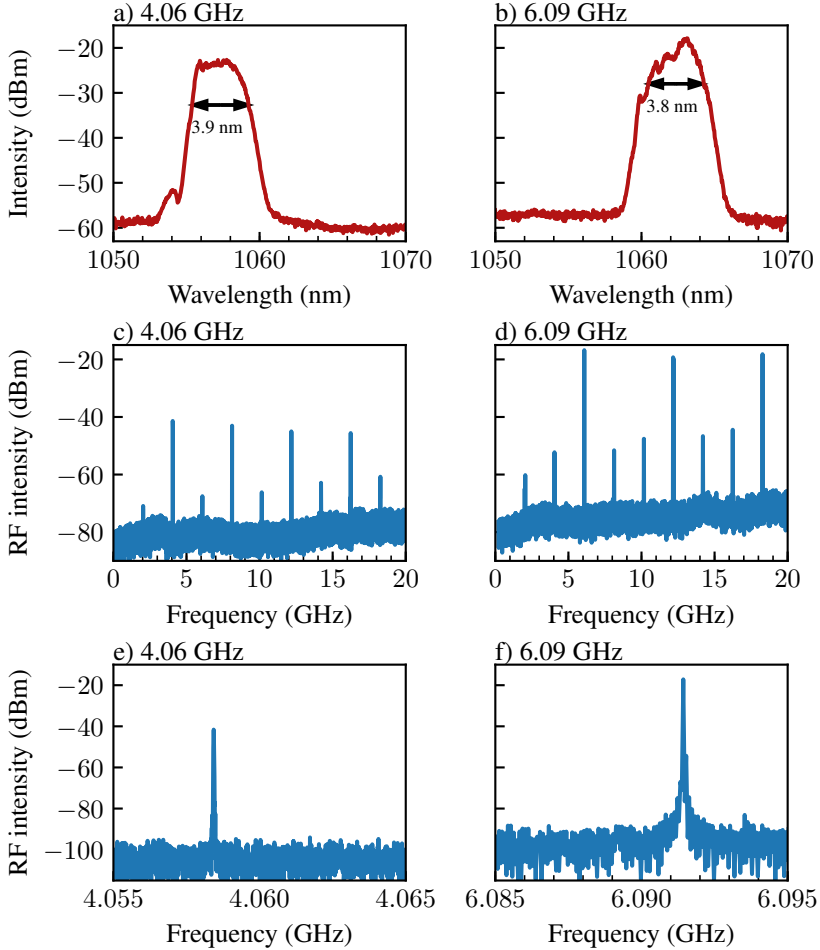


Figure 4.16: The optical and electrical spectrum at the 4 and 6 GHz mode-locking points. a) and b) show the optical spectrum with the 10dB bandwidth indicated, c) and d) the RF spectrum over a large span, and e) and f) show a tighter zoom on the mode-locking peak in the RF spectrum. a), c) and e) show the 4 GHz operating point, and b), d) and f) show the 6 GHz operating point.

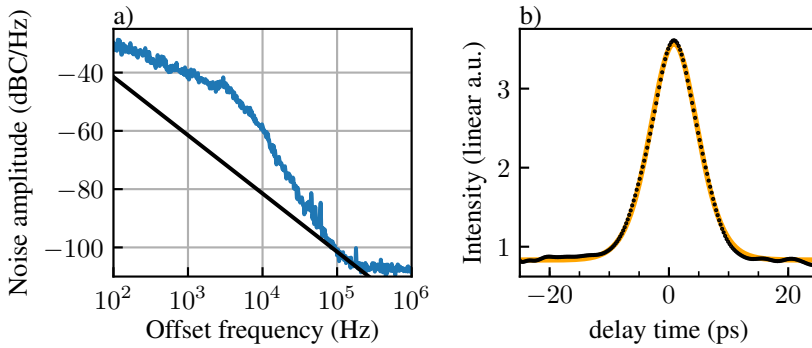


Figure 4.17: a) Phase noise- and b) pulse autocorrelation-measurement of the laser at the optimal 4 GHz operating point. The black line in the phase noise plot a) is added to show what the phase noise of a purely ASE-limited RF line with a linewidth of 1.7 Hz would look like. It's the highest Lorentzian linewidth that would cause a measurement that never goes above the measured phase noise. The orange fit in the pulse width measurement b) shows the autocorrelation of a  $\text{sech}^2$  pulse fit to the measurement, with a FWHM of 9.3 ps, indicating an optical pulse width of 6.03 ps

laser are combined and sent to a high-speed photodiode. The resulting RF signal is then analyzed using an Electrical Spectrum Analyzer (ESA) or captured and analyzed using a real-time oscilloscope or a Data Acquisition system (DAQ). In this case, it was analyzed using a Keysight N9070 MXA ESA.

Fig. 4.18 shows the heterodyne measurement performed. Since the external laser beats with a comb, many beat notes will be recorded. A Voigt curve was fitted to the strongest beat note, and the resulting FWHM linewidth was 4.5 MHz when the resolution bandwidth was set to 1 MHz. This measurement is an upper limit on the linewidth. When the resolution bandwidth was decreased, the apparent linewidth measured on the ESA increased, due to the beat note frequency drifting more during the increased trace acquisition time. Increasing the resolution bandwidth of course increases the apparent linewidth due to the effect of the increased filter bandwidth. This apparent broadening for both higher and lower resolution bandwidths was attributed to instability in both  $F_{\text{rep}}$  and  $F_{\text{CEO}}$  of the MLL under test. The drift is attributed to instability in the coupling of both chips, temperature fluctuations in the chips, and electrical noise in the gain and SA drivers.

To strengthen the argument of the instability further, the expected intrinsic linewidth of the laser can be calculated using the Schawlow-Townes linewidth equation, according to section 2.3.1. Doing this for a laser with a wavelength of 1064 nm, an output power of 5 mW (right after the output coupler), a mirror transmission

of 24%, and a parasitic loss of 90%, the calculated linewidth is 3.25 Hz. This is without taking into account any of the extra factors, but these would not bridge the gap of 6 orders of magnitude with the lower limit measured in the heterodyne measurement.

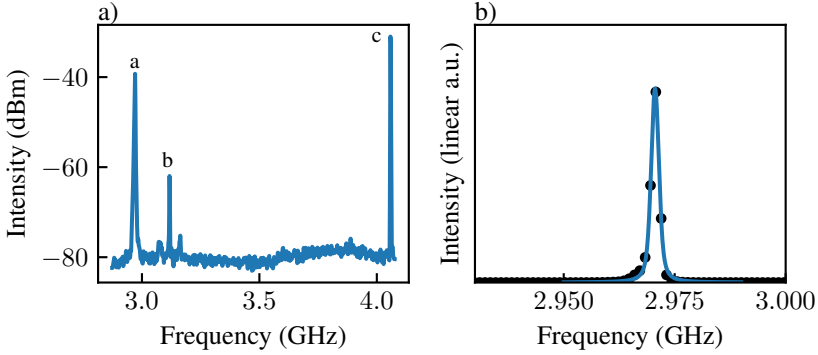


Figure 4.18: The Heterodyne optical linewidth measurement performed at the 6 GHz operating point. a) shows some of the beat notes recorded. Peak c shows the residual RF power at 4.06 GHz, peak a shows the strongest beat note between the external laser and the main MLL peak at 6.09 GHz (outside of the recorded area, but visible in Fig. 4.16). peak b shows the smaller beat note between the external laser and peak c. b) shows a zoom on peak a. Both a) and b) show data from the same measurement trace. Decreasing the resolution- or video-bandwidth of the ESA would increase the measured linewidth, because of the instability of the MLL in both  $F_{rep}$  and  $F_{CEO}$ .

#### 4.4.5 Injection locking

In order to improve the stability of the comb, optical injection locking can be used. Optical injection locking is a technique where an external laser (called the leader- or master laser) that is more stable than the laser under test (follower- or slave laser) is coupled into the laser cavity through the outcoupling mirror. If either of the lasers is tuned so the wavelength difference of both lasers is within the injection-locking range, the follower laser will make a sudden jump in wavelength and lock to the leader laser, after which the follower is locked to the leader. As long as the wavelength fluctuations stay within the locking range, the follower will also follow the fluctuations in the leader laser line caused by laser noise. This effect causes the noise properties of the leader to be copied to the follower, allowing the technique to be used to improve the noise properties of a follower laser. [84] Injection locking has been used to improve the noise performance of single-frequency lasers, but it also works on mode-locked lasers [85]. In this case, one of the optical lines in the

spectrum follows the leader laser.

Injection locking has been performed with the 1064 nm MLL, using the same Koheras Adjustik external fiber laser as used for the heterodyne measurement as a leader laser. The measurement setup is shown in Fig. 4.19. The fiber laser is split, and one part is coupled into the follower laser. The other part is sent through an Acousto-Optic Modulator (AOM). The output of the follower laser is combined with the signal after the AOM and sent to an OSA and an ESA. Because of the AOM in the system, the beat notes will be measured for each comb line with the AOM-shifted version of the leader laser. This allows to verify the coherence between comb lines different from the one that locks, and the leader laser. If this coherence exists, it shows that the entire comb is affected by the leader laser, and not only the comb line that actually locks to the leader laser. Without the AOM, these beat notes showing coherence to the leader laser would be at the same RF frequencies as the beat notes in the RF spectrum of the follower MLL itself.

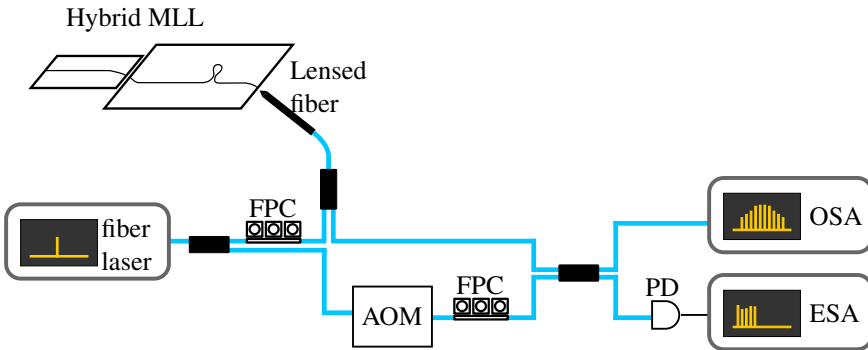


Figure 4.19: The setup used for injection locking the MLL using a fiber laser.

### Low-power injection locking

Initial experiments were done to try injection-locking the laser. The amount of injected power coupled into the MLL was 0.24 mW, and the wavelength was set to the lowest possible value of 1062.95 nm. The wavelength of the external laser could then be tuned over 14 pm using a piezo element in the laser cavity. Because of the wavelengths that could be reached by the external laser, the injection locking could only be performed at the operating point at 6.09 GHz. The spectrum of the operating point at 4.06 GHz is 3 nm away from the lower limit of the external laser wavelength.

To achieve injection locking, the ESA was set to sweep with a sweep time of 100 ms. The frequency range was set to zoom in on the most intense beatnote caused by the

beating between the non-shifted laser line and a comb-line, and the comb line it was beating with. This beat note would quickly drift back and forth within a range of 100 MHz and slowly drift up or down in frequency. By tuning the external laser, the beat note was visually moving closer to one of the beat notes of the frequency comb itself. When the beat note got within around 200 MHz of the comb, it snapped into the beat note, and the AOM-shifted laser line was measured exactly 200 MHz lower than the beat note of the frequency comb. This situation lasted anywhere from 2 to 10 seconds, after which the locking was lost. Because of this short time, only a low-quality ESA trace could be captured from this measurement, which is shown in Fig. 4.20.

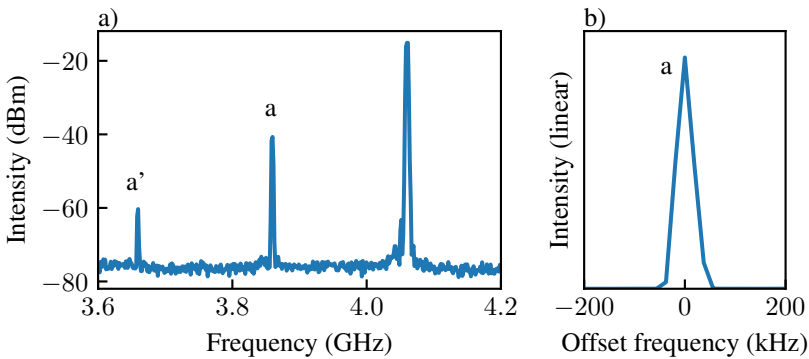


*Figure 4.20: Initial injection locking results with an injected power of 0.24 mW. The line labeled a corresponds to the same label a in Fig. 4.21. the line labeled a' is the same beating, but with the second order modulated line from the AOM, therefore with twice the offset frequency from the MLL line. A zoomed measurement on the beat note could not be taken, because the injection locking didn't sustain long enough.*

In this figure, it can be seen that the comb line the external laser snapped to in the measurement is not the most intense beat note in the comb spectrum as was initially expected. A less intense optical line locked to the injection locking laser. Therefore, the most intense beat notes of the AOM shifted external laser with the frequency comb could be seen at the AOM modulation frequency above the 2 GHz peak and below the 4 GHz peak, as schematically shown in Fig. 4.21.

### Improved injection locking

To improve the time the injection locking would sustain, a new experiment was tried. The splitter ratios used in the setup were changed to increase the power injected in the laser to 1.2 mW. Between the two experiments, the chips had been taken out of

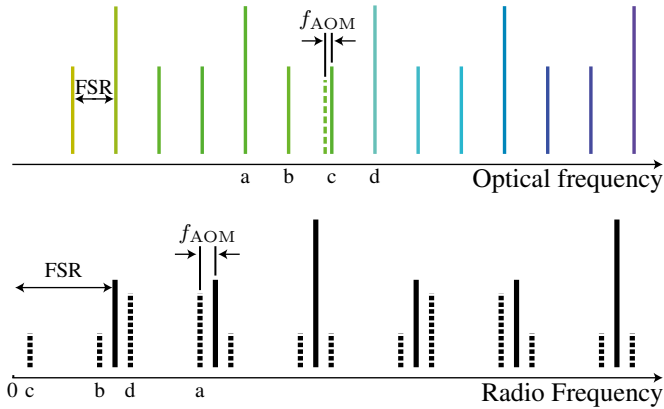


Figure 4.21: Schematic view of the beat notes in the RF spectrum during the first injection locking experiment, and where they come from in the optical spectrum. Solid-colored lines are optical lines in the comb spectrum. The colored dashed line is the AOM-shifted external laser line. Solid black lines are the beat notes from the frequency comb, and dashed black lines are the beat notes of the AOM-shifted external laser and a single comb line. The corresponding optical lines are marked with the same letter in both spectra.

the setup. Therefore, the alignment between both chips is slightly different for this measurement compared to the other measurements described above. This caused the optical spectrum at the 6 GHz operating point to be different, and slightly redshifted. This is likely caused because mode-locking would only occur at a higher gain current with the new alignment, causing a redshift of the gain profile. The external laser was again set to its lowest possible wavelength of 1062.95 nm. Unfortunately, this wavelength is at the very edge of the comb spectrum, but the spectra could not be shifted further.

The results of the injection-locking experiment with more injection power can be seen in Fig. 4.22. In these experiments, the injection locking was sustained for more than 10 minutes at a time. Additionally, the optical line that locked to the external laser was one of the strongest lines, associated with the 6 GHz repetition rate. The optical and electrical spectra are given for the used operating point without the leader laser turned on, and for the leader laser turned on. It can be seen that turning on the injection locking laser did not significantly change the mode-locking characteristic. It can also be seen that the beat note at 5.89 GHz (of the AOM shifted follower laser and one of the comb lines) is narrow, showing coherence between a comb line that is not directly injection-locked and the leader laser. Compared to the heterodyne measurement, the beat note was now completely stable, allowing a measurement with a better resolution bandwidth. The MLL stayed injection locked

while going through the entire leader-laser fine-tuning range of 14 pm (3.7 GHz at 1064 nm).

With injection locking, only one line is really stabilized, and not either  $F_{\text{rep}}$  or  $F_{\text{CEO}}$  on its own. Therefore, using injection locking could increase the noise in  $F_{\text{rep}}$ . A direct measurement of this was not performed, but an indirect one has been performed. In Fig. 4.22 e), both the  $F_{\text{rep}}$  peak and the AOM shifted peak are the same width of 5 sample points, and significantly wider than the resolution bandwidth used. This indicates both peaks have the same width. Therefore, the high-resolution measurement of the AOM shifted peak could be compared to a high-resolution measurement of the  $F_{\text{rep}}$  peak in the free-running state without injection locking. This comparison can be seen in Fig. 4.23. It shows that the injection locking increased the linewidth of the  $F_{\text{rep}}$  peak. Additionally, the repetition rate was slightly reduced by 200 kHz when the injection locking was turned on. Such a shift in repetition rate frequency can also be observed when the gain current and/or the absorber bias is slightly changed since it changes the equilibrium conditions in the MLL.

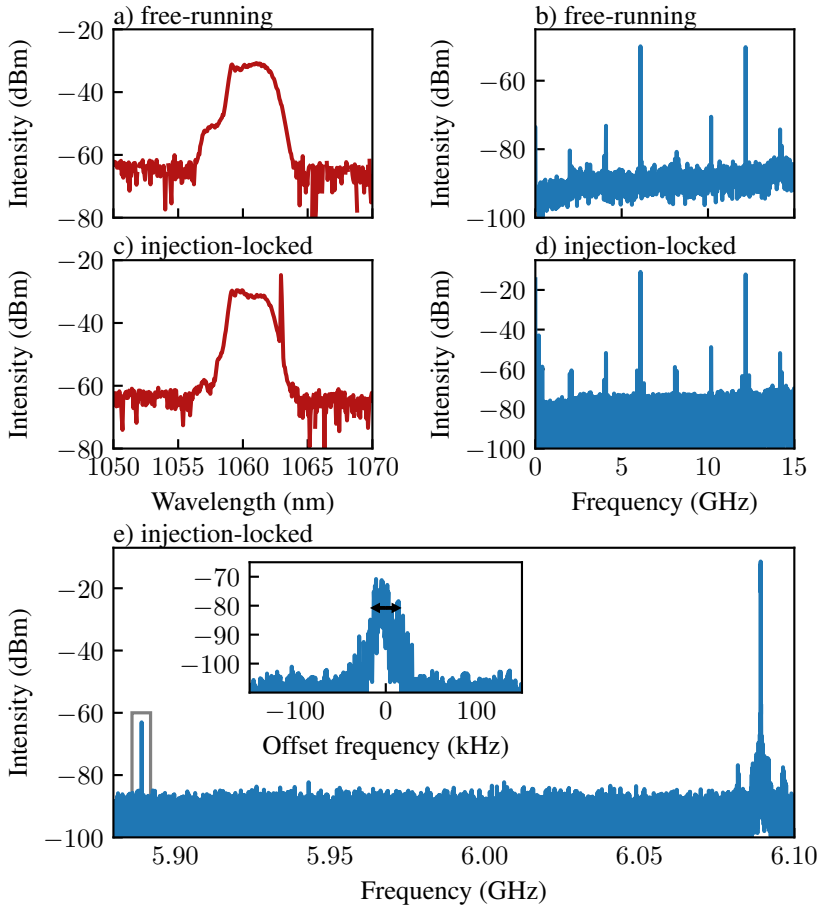


Figure 4.22: Measurements showing injection locking of the MLL to an external fiber laser. a) and b) show the optical- and electrical spectra of the laser without injection locking. c) and d) show the optical and electrical spectra after the injection locking laser is turned on. b) and d) show the mode-locking regime does not change when the laser is injection-locked. e) shows a zoom on the repetition rate peak at 6.09 GHz, and the beat note with the AOM offset leader laser at 5.89 GHz. Both peaks have the same width in the plot. The inset in e) shows a zoom on the peak at 5.89 GHz, with the 10 dB width of 28 kHz indicated.

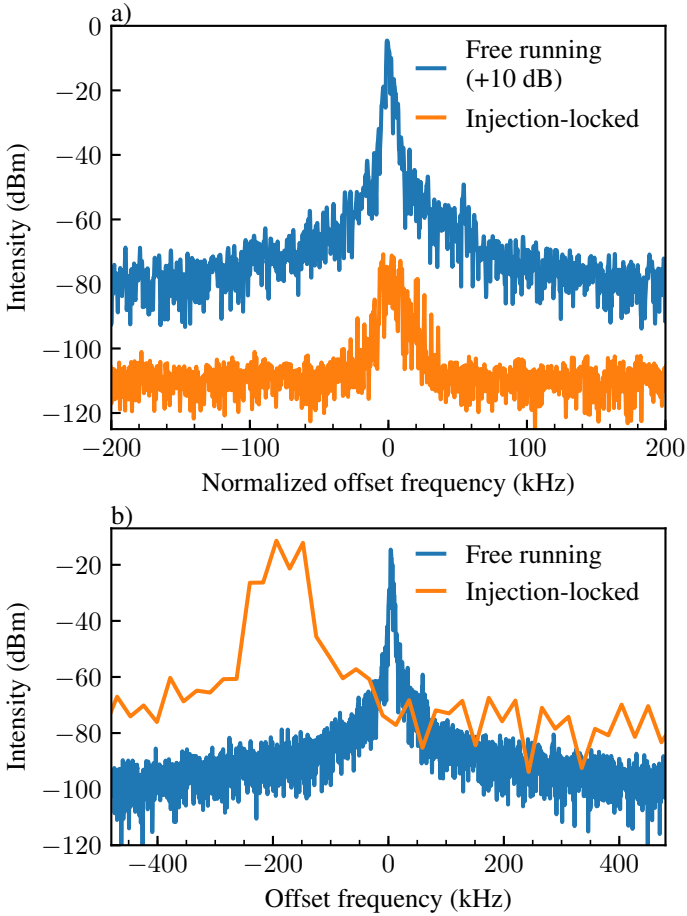


Figure 4.23: Comparison of  $F_{\text{rep}}$  with and without injection locking. a) shows the difference in linewidth, while b) shows the difference in frequency. a) is a comparison of the free-running  $F_{\text{rep}}$  in blue, and the AOM-shifted beat note measured at a high resolution as a substitute for the  $F_{\text{rep}}$  in orange, aligned at 0 offset frequency. b) shows measurements of  $F_{\text{rep}}$  for both the blue and the orange trace.

## 4.5 Comparison of demonstrated integrated ECMLLs

### 4.5.1 Comparison of the presented 1550 nm and 1064 nm MLLs

In Fig. 4.24 the phase noise of the two demonstrated hybrid-integrated mode-locked lasers is plotted in the same graph. The measurements are very comparable since the lasers used the same integration technique, alignment setup, driving electronics, and measurement equipment. There are three significant differences between the MLLs, which are the operating wavelength (1060 nm for FBH, 1550 nm for SMART), the repetition rate (4.06 GHz (second harmonic) for FBH, 2.18 GHz for SMART), and the output power of the laser (2 dBm for FBH, -4 dBm for SMART).

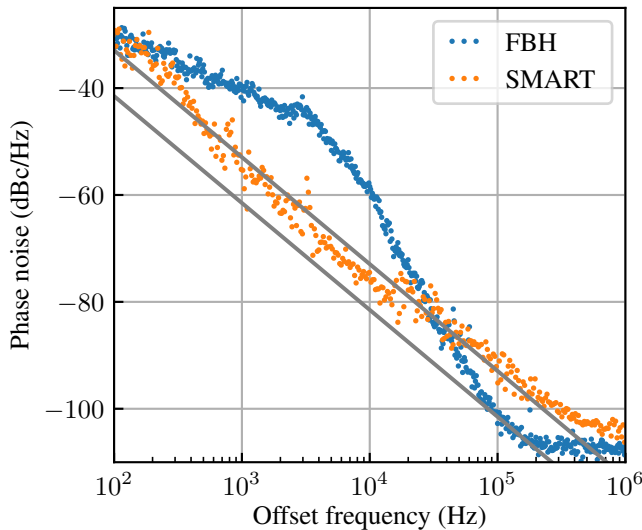


Figure 4.24: Comparison of the phase noise of the FBH and SMART lasers. Note that the repetition rate of the lasers is not directly comparable, since the FBH RF peak measured was at 4.06 GHz, while the SMART RF peak was at 2.18 GHz.

The phase noise properties of both lasers are very different. At frequency offsets below 30 kHz the FBH laser is noisier, while above this frequency the SMART laser shows more noise. Classical (or technical) noise sources are mostly present at lower frequencies and will fall off quickly at higher frequencies. At high offset frequencies only the quantum-limited noise caused by ASE is still present, with a Lorentzian shape, which is a straight line with a slope of -20 dB/decade in a phase-noise plot. For the SMART laser this region is above 100 Hz, until the detector noise dominates the measurement above 1 MHz, where the measurement

flattens. For the FBH laser, the Lorentzian shape is likely still visible from around 80 kHz until around 120 kHz. In these frequency ranges, the two black lines at -20 dB/decade overlap with the measured data points. In both measurements, the shape of the phase noise plot is a straight line with a slope of -20 dB/decade at high frequencies that are still lower than where the noise floor of the measurement is measured, indicating the quantum-limited noise has been detected. [86].

Therefore, it can be concluded from this comparison that the FBH laser has more technical noise and less quantum-limited noise compared to the SMART laser. The reduced quantum-limited noise can be contributed to the higher intra-cavity power of the laser, through the Schawlow-Townes linewidth equation, as described in section 2.3.1. The linewidth is simultaneously increased by the higher photon energy at 1060 nm compared to 1550 nm, but this has a smaller effect than the increased intra-cavity power.

The increased technical noise of the FBH laser compared to the SMART laser was not expected, but it is assumed to be caused by two factors. Firstly, for the same vibration amplitude modifying the distance between both chips, the phase difference experienced by the resonator modes is larger for the lower wavelength laser. In semiconductor gain media, optical phase and gain are coupled through the linewidth enhancement factor  $\alpha$ . Assuming a similar linewidth factor, the lower wavelength laser will therefore experience more phase and amplitude fluctuations due to the same mechanical vibrations modulating the distance between both chips. Secondly, the FBH laser has a 2000  $\mu\text{m}$  SOA length compared to 900  $\mu\text{m}$  for the SMART laser. The thermo-optic coefficient of the FBH laser's SOA material is also slightly higher at  $2.4 \times 10^{-4}$  for GaAs compared to  $2.1 \times 10^{-4}$  for the InP in the SMART laser [87]. This means that similar temperature fluctuations on the SOA cause larger optical phase differences for the FBH laser compared to the SMART laser. The external cavity length in SiN is the same for both lasers, so the same phase fluctuations caused by temperature fluctuations in the external cavity are expected.

## 4.5.2 Comparison to other demonstrated hybrid integrated EC-MLLs

During the time of this PhD, several other integrated ECMLLs have been demonstrated as well, both using hybrid integration and heterogeneous integration. Most of them aimed to decrease the repetition rate of the mode-locked laser using the external cavity. The comparable lasers with repetition rates below 5 GHz are discussed below, and their performance characteristics are summarized in table 4.1.

$\lambda_c$ ( $\mu\text{m}$ )	$f_{\text{rep}}$ (GHz)	$\Delta\nu$ (nm)	$\tau_p$ (ps)	$P_{\text{avg}}$ (mW)	$\delta f_{\text{rep}}$ (kHz)	Integration method	Ref.
1.06	4.06	3	6.03	1.26	0.002	Hybrid	[88] <sup>a</sup>
1.53	5.5	... <sup>b</sup>	...	2	18	Hybrid	[57]
1.54	2	25	...	1.7	110	Hybrid	[89]
1.54	2.2	... <sup>b</sup>	...	9	...	Hybrid	[58]
1.55	0.36	0.5	...	1	...	Hybrid	[4]
1.57	2.18	4.1	6.31	0.3	0.031	Hybrid	[90] <sup>a</sup>
1.58	0.755	1.7	7.5	0.1	0.001	T. printing	[41]
1.60	1	8.5	7	0.3	0.3 <sup>c</sup>	Bonding	[91]
1.61	3	1.7	8	6	0.4	T. printing	[92]

<sup>a</sup>Also presented in this work

<sup>b</sup>Due to the mode-locking method, only two lines in the -3 dB bandwidth

<sup>c</sup>While injection locking and hybrid mode-locking

Table 4.1: Performance characteristics of demonstrated ECMLLs with repetition rates below 5 GHz. The  $\Delta\nu$  and  $\delta f_{\text{rep}}$  bandwidths are both -3 dB bandwidths. Table adapted from [35]

## Hybrid integrated ECMLLs

**H.M.J. Bastiaens et al.** from the University of Twente demonstrated the laser that was most similar to the SMART laser in this work in [89]. The gain section and the first mirror were fabricated in an InP chip, and the second mirror was a tunable Sagnac mirror made in a SiN feedback chip. The SA placement was also the same. A significant difference is that the mirror in the InP chip reflects only 40 percent of the light, and couples out the remaining part, used as a monitor port. The repetition rate of the laser is 2.09 GHz. Compared to the SMART laser, the optical spectrum is significantly wider, with a -3 dB width of 25 nm compared to 4.0 nm for the SMART laser. However, the linewidth of the repetition rate beat note is significantly wider as well, with a 3 dB linewidth of 61 KHz. On the SMART laser, 10 dB linewidths below 1 kHz were measured using an ESA sweep.

**Y. Ibrahim et al.** from III-V lab demonstrated a hybrid integrated self-mode-locked laser in [4]. This laser works at 1550 nm, using an RSOA made in InP. The second mirror is a Bragg reflector on the external cavity SiN chip. There is no SA in this laser, but it does show self-mode-locking. It was attempted to replicate this type of mode-locking for this PhD with the self-mode-locked laser described in section 4.3, but this was not successful. The main difference between the two systems is the reflector in SiN is a narrow-band Bragg reflector in the working laser, and a wide-band Sagnac reflector in the non-working laser. On top of that, the Bragg reflector introduces some anomalous dispersion to the laser cavity, which is not present in the non-working laser.

**Two different publications** from the University of Twente show mode-locking using a new method [57, 58]. This method uses the same chip architecture as a typical single-frequency laser with a Vernier mirror. Through careful tuning of the rings in the Vernier mirror, two adjacent cavity modes can have the same reflection, causing them both to start lasing. Through the process of four-wave mixing, these two laser lines generate extra lines in the comb that are locked in phase, creating a comb spectrum at the output.

Compared to conventional mode-locking techniques, this method generates frequency combs with only a few lines, and therefore a very small optical bandwidth. Additionally, the lines generated through the nonlinear processes are also more than 10 dB below the most intense lines, meaning the -10 dB bandwidth only contains 2 lines. It's unclear whether the width of combs generated using this method can be extended or not. These lasers do have the advantage that a single laser can be fabricated that can work both as both a mode-locked laser and a single-frequency laser, depending on the operating parameters.

### **Heterogeneously integrated ECMLLs**

Passively mode-locked ECMLLs using heterogeneous integration have also been demonstrated during the same timeframe. There are three different demonstrations with a repetition rate below 5 GHz, one using bonding and 2 using transfer printing. All of these demonstrations were done by researchers at Ghent University.

**K. Van Gasse et al.** demonstrated an ECMLL made with a bonding process of InP onto Si [93]. This laser has also successfully been stabilized in both  $f_{\text{rep}}$  and  $f_{\text{CEO}}$  using a combination of hybrid mode-locking and injection locking, in order to use the laser for dual-comb gas-spectroscopy experiments in combination with an electro-optic comb. In contrast to the experience of using hybrid-integrated MLLs on a dynamic setup, the laser worked very repeatably, with stable operation over ten weeks (more than 1000 operation hours) reported in the work [91].

**A. Hermans et al.** demonstrated an ECMLL using transfer printing of InP SOAs onto an SiN cavity, targeting to increase pulse energies over previous demonstrations [92]. To prevent nonlinear losses due to two-photon absorption at the used wavelength around 1.55  $\mu\text{m}$ , a SiN cavity was used instead of a Si cavity, since two-photon absorption cannot happen at 1.55  $\mu\text{m}$  due to the higher bandgap of SiN. It reached the highest average power of all the demonstrated ECMLLs, at 6 mW average output power.

**S. Cuyvers et al.** demonstrated another ECMLL using transfer printing of InP onto SiN [41]. From the demonstrated ECMLLs that contain an SA, this one reached

the lowest repetition rate of 755 MHz.



# 5

## Conclusion and outlook

---

<b>5.1 Conclusions . . . . .</b>	<b>105</b>
<b>5.2 Outlook . . . . .</b>	<b>106</b>

---

### 5.1 Conclusions

The main goal of this work was to demonstrate hybrid integrated external cavity mode-locked lasers and characterize their noise performance. Afterwards, the comb spectrum would be stabilized to use the MLLs for spectroscopy experiments at MPQ.

The main goal has been achieved, and two hybrid integrated ECMLLs have been demonstrated and characterized. The first one worked at 1550 nm, the second at 1060 nm. With regards to the additional goal, the 1060 nm MLL has also been partly stabilized using injection locking. With this technique, only one of the laser lines in the frequency comb is stabilized. Therefore, this is not a suitable source for precision spectroscopy applications yet. The next goal would be to stabilize both  $f_{\text{rep}}$  and  $f_{\text{CEO}}$  simultaneously to fully define the frequency comb. Since full comb stabilization was not achieved yet, no spectroscopy experiments have been performed with the demonstrated MLLs.

During the same time as the work on this PhD was done, work by K. Van Gasse et al. showed that full comb stabilization of an integrated ECMLL is indeed possible [91]. This demonstration was done with a heterogeneously integrated laser, and not a hybrid-integrated laser on a dynamic setup.

Compared to heterogeneous integration, hybrid integration could theoretically be advantageous in a research environment to test coupling several different cavity chips to the same gain chip, to keep as many variables the same in the experiments. However, in practice, this seems to be hard to achieve, as was shown by the injection locking experiments. When taking both chips out of the setup, and realigning them at a later stage, the same alignment could not be reproduced, and therefore the mode-locking regime had changed as well. If this can happen while realigning the same chips, it cannot be known whether the different operating characteristics when using multiple different chips are due to the chips themselves, or due to the exact alignment of the chips. This problem might be alleviated by improving the measurement setup and controlling the three angles of the chips as well.

Discussions with researchers doing transfer printing revealed that similar problems around reproducibility are experienced using that technique. In the case of transfer-printing the mode-locked operating points of 2 different MLLs using the exact same design can differ significantly, especially regarding the wavelength of the comb spectrum. This can be detrimental if the application of the MLL requires a very specific wavelength, for example for spectroscopy or datacom applications.

## 5.2 Outlook

In order to continue the work as initially planned, and use one of the demonstrated MLLs for spectroscopy experiments, it is likely necessary to glue together the gain chip and the cavity chip permanently. This will maybe improve the short-term stability of the laser, but it will definitely improve the long-term stability of the laser, which currently requires realignment around every 30 minutes, and even quicker shortly after the gain current is changed.

Secondly, more thorough experiments should be done to optimize the injection locking of the laser. Currently, only two different injection powers have been used. The repetition rate linewidth during injection could maybe be reduced by using a different injection power. On top of this, a method for simultaneously stabilizing the repetition rate of the laser should be found. In the demonstration of the fully stabilized integrated ECMLL this was achieved using hybrid mode-locking [91]. However, for the MLL demonstrated in this work this is not an option, since there is no way to inject RF power into the SA efficiently. This is because the electrical

contact to the SA was not designed with hybrid mode-locking in mind.

A different scheme that could be used to fully stabilize the comb is to do injection locking using a seed laser that is modulated with the desired repetition rate frequency. This causes sidebands to form at exactly the desired repetition rate, which will cause more than one line to lock to the seed laser. When 2 lines are locked, both  $f_{\text{CEO}}$  and  $f_{\text{rep}}$  are locked as well.

Regarding the fabrication, work should be done to improve the reproducibility of the wavelength span of the frequency comb output between several chips with the same design. In the case of hybrid integration, this could likely be done by improving the alignment setup. In the case of transfer printing, a more precise transfer printing tool could also be the solution. On top of this, fabrication in a more controlled fab might also help in this regard. Once this fabrication can be done reliably, small-size spectroscopy-, communications- and LIDAR systems could start being designed around these physically small comb sources.



# References

- [1] Anton Lukashchuk, Johann Riemensberger, Maxim Karpov, Junqiu Liu, and Tobias J. Kippenberg. *Dual chirped microcomb based parallel ranging at megapixel-line rates*. Nature Communications, 13(1):3280, Jun 2022.
- [2] Rafael A. Probst, Gaspare Lo Curto, Gerardo Avila, Bruno L. Canto Martins, José Renan de Medeiros, Massimiliano Esposito, Jonay I. González Hernández, Theodor W. Hänsch, Ronald Holzwarth, Florian Kerber, Izan C. Leão, Antonio Manescau, Luca Pasquini, Rafael Rebolo-López, Tilo Steinmetz, Thomas Udem, and Yuanjie Wu. *A laser frequency comb featuring sub-cm/s precision for routine operation on HARPS*. In Suzanne K. Ramsay, Ian S. McLean, and Hideki Takami, editors, Ground-based and Airborne Instrumentation for Astronomy V, volume 9147, page 91471C. International Society for Optics and Photonics, SPIE, 2014.
- [3] Nathalie Picqué and Theodor W. Hänsch. *Frequency comb spectroscopy*. Nature Photonics, 13(3):146–157, feb 2019.
- [4] Yasmine Ibrahimi, Sylvain Boust, Quentin Wilmart, Jean-François Paret, Alexandre Garreau, Karim Mekhazni, Catherine Fortin, François Duport, Jean-Marc Fedeli, Corrado Sciancalepore, Stéphanie Garcia, and Frédéric van Dijk. *Low FSR Mode-Locked Laser Based on InP-Si<sub>3</sub>N<sub>4</sub> Hybrid Integration*. J. Lightwave Technol., 39(24):7573–7580, Dec 2021.
- [5] Weng W. Chow, Songtao Liu, Zeyu Zhang, John E. Bowers, and Murray Sargent. *Multimode description of self-mode locking in a single-section quantum-dot laser*. Opt. Express, 28(4):5317–5330, Feb 2020.
- [6] The Nobel Foundation. *The Nobel Prize in Physics 1956*. <https://www.nobelprize.org/prizes/physics/1956/summary/>, accessed 16 jan 2023.
- [7] The Nobel Foundation. *The Nobel Prize in Physics 2000*. <https://www.nobelprize.org/prizes/physics/2000/summary/>, accessed 16 jan 2023.

- [8] NVIDIA corporation. *NVIDIA ADA GPU Architecture*. <https://images.nvidia.com/aem-dam/Solutions/geforce/ada/nvidia-ada-gpu-architecture.pdf>, accessed 16 jan 2023.
- [9] The Nobel Foundation. *The Nobel Prize in Physics 1964*.
- [10] ZhI Alferov, VM Andreev, EL Portnoi, and MK Trukan. *Injection lasers based on heterojunctions of the AlAs-GaAs system having a low emission threshold at room temperature(Low threshold injection lasers in IR and visible spectrum at room temperature employing AlAs-GaAs heterojunctions, noting use for CW mode)*. *Fizika I Tekhnika Poluprovodnikov*, 3:1328–1332, 1969.
- [11] F. P. Kapron, D. B. Keck, and R. D. Maurer. *Radiation losses in glass optical waveguides*. *Applied Physics Letters*, 17(10):423–425, nov 1970.
- [12] Meint Smit, Kevin Williams, and Jos van der Tol. *Past, present, and future of InP-based photonic integration*. *APL Photonics*, 4(5):050901, may 2019.
- [13] M. Suzuki, Y. Noda, H. Tanaka, S. Akiba, Y. Kushiro, and H. Isshiki. *Monolithic integration of InGaAsP/InP distributed feedback laser and electroabsorption modulator by vapor phase epitaxy*. *Journal of Lightwave Technology*, 5(9):1277–1285, 1987.
- [14] Yikai Su, Yong Zhang, Ciyuan Qiu, Xuhan Guo, and Lu Sun. *Silicon Photonic Platform for Passive Waveguide Devices: Materials, Fabrication, and Applications*. *Advanced Materials Technologies*, 5(8):1901153, 2020.
- [15] Houssein El Dirani, Marco Casale, Sébastien Kerdiles, Carole Socquet-Clerc, Xavier Letartre, Christelle Monat, and Corrado Sciancalepore. *Crack-Free Silicon-Nitride-on-Insulator Nonlinear Circuits for Continuum Generation in the C -Band*. *IEEE Photonics Technology Letters*, 30(4):355–358, 2018.
- [16] Kerstin Wörhoff, René G. Heideman, Arne Leinse, and Marcel Hoekman. *TriPLeX: a versatile dielectric photonic platform*. *Advanced Optical Technologies*, 4(2), jan 2015.
- [17] Scott Watson, Steffan Gwyn, Shaun Viola, Giovanni Giuliano, Thomas J. Slight, Szymon Stanczyk, Szymon Grzanka, Amit Yadav, Duncan Rowe, Leslie Laycock, Kevin E. Docherty, Edik Rafailov, Piotr Perlin, Steve Najda, Mike Leszczynski, and Anthony E. Kelly. *InGaN/GaN Laser Diodes and their Applications*. In 2018 20th International Conference on Transparent Optical Networks (ICTON). IEEE, jul 2018.
- [18] Nikolai B. Chichkov, Amit Yadav, Evgeny Zharebtsov, Meng Wang, Gela Kipshidze, Gregory Belenky, Leon Shtrengas, and Edik U. Rafailov. *Wavelength-Tunable, GaSb-Based, Cascaded Type-I Quantum-Well Laser Emitting Over a*

- Range of 300 nm*. IEEE Photonics Technology Letters, 30(22):1941–1943, nov 2018.
- [19] Richard Jones, Pierre Doussiere, Jeffrey B. Driscoll, Wenhua Lin, Haijiang Yu, Yulia Akulova, Tin Komljenovic, and John E. Bowers. *Heterogeneously Integrated InP/Silicon Photonics: Fabricating Fully Functional Transceivers*. IEEE Nanotechnology Magazine, 13(2):17–26, apr 2019.
- [20] N. Lindenmann, G. Balthasar, D. Hillerkuss, R. Schmogrow, M. Jordan, J. Leuthold, W. Freude, and C. Koos. *Photonic wire bonding: a novel concept for chip-scale interconnects*. Optics Express, 20(16):17667, jul 2012.
- [21] PhiX B.V. *Prototype packages*. <https://www.phix.com/our-offering/prototype-package/>, accessed 26 jan 2023.
- [22] Michael Theurer, Martin Moehrle, Ariane Sigmund, Karl-Otto Velthaus, Ruud M. Oldenbeuving, Lennart Wevers, Ferry M. Postma, Richard Mateman, Frederik Schreuder, Dimitri Geskus, Kerstin Worhoff, Ronald Dekker, Rene G. Heideman, and Martin Schell. *Flip-Chip Integration of InP to SiN Photonic Integrated Circuits*. Journal of Lightwave Technology, 38(9):2630–2636, may 2020.
- [23] The Nobel Foundation. *The Nobel Prize in Physics 2005*. <https://www.nobelprize.org/prizes/physics/2005/summary/>, accessed 16 jan 2023.
- [24] J. Reichert, R. Holzwarth, Th. Udem, and T.W. Hänsch. *Measuring the frequency of light with mode-locked lasers*. Optics Communications, 172(1-6):59–68, dec 1999.
- [25] Scott A. Diddams, David J. Jones, Jun Ye, Steven T. Cundiff, John L. Hall, Jinendra K. Ranka, Robert S. Windeler, Ronald Holzwarth, Thomas Udem, and T. W. Hänsch. *Direct Link between Microwave and Optical Frequencies with a 300 THz Femtosecond Laser Comb*. Physical Review Letters, 84(22):5102–5105, may 2000.
- [26] Christopher W. Oates and Andrew D. Ludlow. *Optical lattice clocks*. Optics & Photonics news, 26, 2015.
- [27] Ian Coddington, Nathan Newbury, and William Swann. *Dual-comb spectroscopy*. Optica, 3(4):414–426, Apr 2016.
- [28] Lars Lundberg, Magnus Karlsson, Abel Lorences-Riesgo, Mikael Mazur, Victor Torres-Company, Jochen Schröder, and Peter A. Andrekson. *Frequency Comb-Based WDM Transmission Systems Enabling Joint Signal Processing*. Applied Sciences, 8(5), 2018.

- [29] Minhao Pu, Luisa Ottaviano, Elizaveta Semanova, and Kresten Yvind. *Efficient frequency comb generation in AlGaAs-on-insulator*. *Optica*, 3(8):823, July 2016.
- [30] L. A. Lugiato, F. Prati, M. L. Gorodetsky, and T. J. Kippenberg. *From the Lugiato–Lefever equation to microresonator-based soliton Kerr frequency combs*. *Philosophical Transactions of the Royal Society A: Mathematical, Physical and Engineering Sciences*, 376(2135):20180113, nov 2018.
- [31] Myoung-Gyun Suh and Kerry Vahala. *Gigahertz-repetition-rate soliton microcombs*. *Optica*, 5(1):65, jan 2018.
- [32] Travis C. Briles, Su-Peng Yu, Lin Chang, Chao Xiang, Joel Guo, David Kinghorn, Gregory Moille, Kartik Srinivasan, John E. Bowers, and Scott B. Papp. *Hybrid InP and SiN integration of an octave-spanning frequency comb*. *APL Photonics*, 6(2):026102, feb 2021.
- [33] Chao Xiang, Junqiu Liu, Joel Guo, Lin Chang, Rui Ning Wang, Wenle Weng, Jonathan Peters, Weiqiang Xie, Zeyu Zhang, Johann Riemensberger, Jennifer Selvidge, Tobias J. Kippenberg, and John E. Bowers. *Laser soliton microcombs heterogeneously integrated on silicon*. *Science*, 373(6550):99–103, jul 2021.
- [34] Lars Lundberg, Magnus Karlsson, Abel Lorences-Riesgo, Mikael Mazur, Victor Torres-Company, Jochen Schröder, and Peter Andrekson. *Frequency Comb-Based WDM Transmission Systems Enabling Joint Signal Processing*. *Applied Sciences*, 8(5):718, May 2018.
- [35] Artur Hermans, Kasper Van Gasse, and Bart Kuyken. *On-chip optical comb sources*. *APL Photonics*, 7(10):100901, oct 2022.
- [36] Nicola Andriolli, Tommaso Cassese, Marco Chiesa, Cristina de Dios, and Giampiero Contestabile. *Photonic Integrated Fully Tunable Comb Generator Cascading Optical Modulators*. *Journal of Lightwave Technology*, 36(23):5685–5689, dec 2018.
- [37] Francesca Bontempi, Nicola Andriolli, Filippo Scotti, Marco Chiesa, and Giampiero Contestabile. *Comb Line Multiplication in an InP Integrated Photonic Circuit Based on Cascaded Modulators*. *IEEE Journal of Selected Topics in Quantum Electronics*, 25(6):1–7, nov 2019.
- [38] Isaac Luntadila Lufungula, Amirhassan Shams-Ansari, Dylan Renaud, Camiel Op de Beeck, Stijn Cuyvers, Stijn Poelman, Gunther Roelkens, Marko Loncar, and Bart Kuyken. *On-chip electro-optic frequency comb generation using a heterogeneously integrated laser*. In *Conference on Lasers and Electro-Optics*. Optica Publishing Group, 2022.

- [39] Mian Zhang, Brandon Buscaino, Cheng Wang, Amirhassan Shams-Ansari, Christian Reimer, Rongrong Zhu, Joseph M. Kahn, and Marko Lončar. *Broadband electro-optic frequency comb generation in a lithium niobate microring resonator*. *Nature*, 568(7752):373–377, mar 2019.
- [40] Martijn J. R. Heck, Michael L. Davenport, Hyundai Park, Daniel J. Blumenthal, and John E. Bowers. *Ultra-Long Cavity Hybrid Silicon Mode-locked Laser Diode Operating at 930 MHz*. In *Optical Fiber Communication Conference*. OSA, 2010.
- [41] Stijn Cuyvers, Bahawal Haq, Camiel Op de Beeck, Stijn Poelman, Artur Hermans, Zheng Wang, Agnieszka Gocalinska, Emanuele Pelucchi, Brian Corbett, Gunther Roelkens, Kasper Van Gasse, and Bart Kuyken. *Low Noise Heterogeneous III-V-on-Silicon-Nitride Mode-Locked Comb Laser*. *Laser & Photonics Reviews*, 15(8):2000485, jun 2021.
- [42] ioffe NSM. *Band structure of Si*. <http://www.ioffe.ru/SVA/NSM/Semicond/Si/bandstr.html>, accessed 11 jan 2023.
- [43] ioffe NSM. *Band structure of InP*. <http://www.ioffe.ru/SVA/NSM/Semicond/InP/bandstr.html>, accessed 11 jan 2023.
- [44] Y Suematsu and A R Adams, editors. *Handbook of semiconductor lasers and photonic*. Chapman and Hall, London, England, 1994 edition, September 1994.
- [45] Michael J. Connelly. *Semiconductor Optical Amplifiers*. Kluwer Academic Publishers, Boston, 2006.
- [46] Peter W. Milonni and Joseph H. Eberly. *Laser Physics*. John Wiley & Sons, Inc., March 2010.
- [47] Rüdiger Paschotta. *Mode locking*. [https://www.rp-photonics.com/mode\\_locking.html](https://www.rp-photonics.com/mode_locking.html), accessed 11 jan 2023.
- [48] Rebecca Kayla Schaevitz. *Electroabsorption Mechanisms in Germanium Quantum Well Material*. PhD thesis, Stanford University, 2011.
- [49] H. Haus. *Theory of mode locking with a slow saturable absorber*. *IEEE Journal of Quantum Electronics*, 11(9):736–746, sep 1975.
- [50] H. Haus. *A theory of forced mode locking*. *IEEE Journal of Quantum Electronics*, 11(7):323–330, jul 1975.

- [51] Hermann A. Haus. *Theory of mode locking with a fast saturable absorber*. Journal of Applied Physics, 46(7):3049–3058, jul 1975.
- [52] Rüdiger Paschotta. *Upper-state Lifetime*. [https://www.rp-photonics.com/upper\\_state\\_lifetime.html](https://www.rp-photonics.com/upper_state_lifetime.html), accessed 30 may 2023.
- [53] Rüdiger Paschotta. *Mode-locked Diode Lasers*. [https://www.rp-photonics.com/mode\\_locked\\_diode\\_lasers.html](https://www.rp-photonics.com/mode_locked_diode_lasers.html), accessed 30 may 2023.
- [54] R. Paschotta and U. Keller. *Passive mode locking with slow saturable absorbers*. Applied Physics B: Lasers and Optics, 73(7):653–662, November 2001.
- [55] J. Javaloyes and S. Balle. *Anticolliding design for monolithic passively mode-locked semiconductor lasers*. Optics Letters, 36(22):4407, nov 2011.
- [56] Sylwester Latkowski, Valentina Moskalenko, Saeed Tahvili, Luc Augustin, Meint Smit, Kevin Williams, and Erwin Bente. *Monolithically integrated 25 GHz extended cavity mode-locked ring laser with intracavity phase modulators*. Optics Letters, 40(1):77, dec 2014.
- [57] Jesse Mak, Albert van Rees, Youwen Fan, Edwin J. Klein, Dimitri Gekus, Peter J. M. van der Slot, and Klaus.-J. Boller. *Linewidth narrowing via low-loss dielectric waveguide feedback circuits in hybrid integrated frequency comb lasers*. Optics Express, 27(9):13307, apr 2019.
- [58] Yvan Klaver, Jörn P. Epping, Chris G. H. Roeloffzen, and David A. I. Marpaung. *Self-mode-locking in a high-power hybrid silicon nitride integrated laser*. Optics Letters, 47(1):198, dec 2021.
- [59] A. L. Schawlow and C. H. Townes. *Infrared and Optical Masers*. Physical Review, 112(6):1940–1949, dec 1958.
- [60] Melvin Lax. *Classical Noise. V. Noise in Self-Sustained Oscillators*. Physical Review, 160(2):290–307, aug 1967.
- [61] J J Zayhowski. *Passively Q-switched microchip lasers*. In Solid-State Lasers and Applications, pages 1–76. CRC Press, December 2017.
- [62] K. Petermann. *Calculated spontaneous emission factor for double-heterostructure injection lasers with gain-induced waveguiding*. IEEE Journal of Quantum Electronics, 15(7):566–570, July 1979.
- [63] Tin Komljenovic, Sudharsanan Srinivasan, Erik Norberg, Michael Davenport, Gregory Fish, and John E. Bowers. *Widely Tunable Narrow-Linewidth Monolithically Integrated External-Cavity Semiconductor Lasers*. IEEE Journal of Selected Topics in Quantum Electronics, 21(6):214–222, November 2015.

- [64] Anatol Khilo, Steven J. Spector, Matthew E. Grein, Amir H. Nejadmalayeri, Charles W. Holzwarth, Michelle Y. Sander, Marcus S. Dahlem, Michael Y. Peng, Michael W. Geis, Nicole A. DiLello, Jung U. Yoon, Ali Motamedi, Jason S. Orcutt, Jade P. Wang, Cheryl M. Sorace-Agaskar, Miloš A. Popović, Jie Sun, Gui-Rong Zhou, Hyunil Byun, Jian Chen, Judy L. Hoyt, Henry I. Smith, Rajeev J. Ram, Michael Perrott, Theodore M. Lyszczarz, Erich P. Ippen, and Franz X. Kärtner. *Photonic ADC: overcoming the bottleneck of electronic jitter*. Optics Express, 20(4):4454, February 2012.
- [65] Lukas Drzewietzki, Stefan Breuer, and Wolfgang Elsäßer. *Timing jitter reduction of passively mode-locked semiconductor lasers by self- and external-injection: Numerical description and experiments*. Optics Express, 21(13):16142, 2013.
- [66] K. Van Gasse, S. Uvin, V. Moskalenko, S. Latkowski, G. Roelkens, E. Bente, and B. kuyken. *Recent Advances in the Photonic Integration of Mode-Locked Laser Diodes*. IEEE Photonics Technology Letters, 31(23):1870–1873, dec 2019.
- [67] V. Moskalenko, S. Latkowski, T. de Vries, L. M. Augustin, X. J. M. Leijtens, M. K. Smit, and E. A. J. M. Bente. *A Wide Bandwidth Coherent Optical Comb Source Based on a Monolithically Integrated Mode-Locked Ring Laser*. In Optical Fiber Communication Conference. OSA, 2014.
- [68] Luc M. Augustin, Rui Santos, Erik den Haan, Steven Kleijn, Peter J. A. Thijs, Sylwester Latkowski, Dan Zhao, Weiming Yao, Jeroen Bolk, Huub Ambrosius, Sergei Mingaleev, Andre Richter, Arjen Bakker, and Twan Korthorst. *InP-Based Generic Foundry Platform for Photonic Integrated Circuits*. IEEE Journal of Selected Topics in Quantum Electronics, 24(1):1–10, jan 2018.
- [69] Rüdiger Paschotta. *Upper-state Lifetime*. [https://www.rp-photonics.com/fresnel\\_equations.html](https://www.rp-photonics.com/fresnel_equations.html), accessed 31 may 2023.
- [70] Camiel op de Beeck. *Heterogeneous Integration of III-V Semiconductor Light Sources on Low-Refractive-Index Platforms*. PhD thesis, Universiteit Gent, 2022.
- [71] Jau-Wen Lin and Ming-Hon Cheng. *Investigation of chipping and wear of silicon wafer dicing*. Journal of Manufacturing Processes, 16(3):373–378, 2014.
- [72] Haolan Zhao. *Coherent Raman Spectroscopy Enabled by Photonic Integrated Circuits*. PhD thesis, Universiteit Gent, 2017.

- [73] Kayaku Advanced Materials. *SU-8 Permanent Negative Epoxy Photoresist technical data sheet*. <https://kayakuam.com/wp-content/uploads/2020/09/KAM-SU-8-2-25-Datasheet-9.3.20-final.pdf>, accessed 1 feb 2023.
- [74] Albertas Žukauskas, Gintarė Batavičiūtė, Mindaugas Ščiuka, Tomas Jukna, Andrius Melninkaitis, and Mangirdas Malinauskas. *Characterization of photopolymers used in laser 3D micro/nanolithography by means of laser-induced damage threshold (LIDT)*. *Optical Materials Express*, 4(8):1601, 2014.
- [75] Andrius Melninkaitis, Mindaugas Ščiuka, Gintarė Batavičiūtė, Julius Mirauskas, Saulius Bucka, and Valdas Sirutkaitis. *Automated test station for characterization of optical resistance with ultrashort pulses at multi kilohertz repetition rates*. In Gregory J. Exarhos, Vitaly E. Gruzdev, Joseph A. Menapace, Detlev Ristau, and M J Soileau, editors, *Laser-Induced Damage in Optical Materials: 2012*, volume 8530, page 85301M, dec 2012.
- [76] Luc M. Augustin, Rui Santos, Erik Den Haan, Steven Kleijn, Peter J.A. Thijs, Sylwester Latkowski, Dan Zhao, Weiming Yao, Jeroen Bolk, Huub Ambrosius, Sergei Mingaleev, André Richter, Arjen Bakker, and Twan Korthorst. *InP-Based Generic Foundry Platform for Photonic Integrated Circuits*. *IEEE Journal of Selected Topics in Quantum Electronics*, 24(1):1–12, 2018.
- [77] Valentina Moskalenko. *Extended cavity passively mode-locked lasers in indium phosphide generic integration technology*. PhD thesis, Technische Universiteit Eindhoven, 2016.
- [78] Emil Kleijn, Meint K. Smit, and Xaveer J.M. Leijtsens. *Multimode interference reflectors: A new class of components for photonic integrated circuits*. *Journal of Lightwave Technology*, 31(18):3055–3063, 2013.
- [79] Augustinas Vizbaras, Ieva Šimonytė, Arūnas Miasojedovas, Augustinas Trinkūnas, Tadas Bučiūnas, Mindaugas Greibus, Greta Naujokaitė, Nicolas Torcheboeuf, Serge Droz, Dmitri Boiko, Žilvinas Dambrauskas, Antanas Gulbinas, and Kristijonas Vizbaras. *Swept-wavelength lasers based on GaSb gain-chip technology for non-invasive biomedical sensing applications in the 1.7-2.5 μm wavelength range*. *Biomed. Opt. Express*, 9(10):4834–4849, Oct 2018.
- [80] Yufei Xing, Umar Khan, Antônio Ribeiro Alves Júnior, and Wim Bogaerts. *Behavior model for directional coupler*. In *Proceedings Symposium IEEE Photonics Society Benelux*, pages 128–131, 2017.
- [81] Hubertus Bastiaens, Govert Neijts, Anzal Memon, Youwen Fan, Jesse Mak, Dimitri Geskus, Marcel Hoekman, Valentina Moskalenko, Erwin Bente, and

- Klaus Boller. *First demonstration of a hybrid integrated InP-Si<sub>3</sub>N<sub>4</sub> diode laser for broadband optical frequency comb generation*. In Alexey A. Belyanin and Peter M. Smowton, editors, *Novel In-Plane Semiconductor Lasers XX*. SPIE, March 2021.
- [82] Andrew M. Weiner. *Ultrafast Optics*. Wiley, October 2008.
- [83] Steve Sanders, Amnon Yariv, Joel Paslaski, Jeffrey E. Ungar, and Hal A. Zarem. *Passive mode locking of a two-section multiple quantum well laser at harmonics of the cavity round-trip frequency*. *Applied Physics Letters*, 58(7):681–683, 1991.
- [84] Zhixin Liu and Radan Slavík. *Optical Injection Locking: From Principle to Applications*. *Journal of Lightwave Technology*, 38(1):43–59, 2020.
- [85] Sarah Uvin, Shahram Keyvaninia, Francois Lelarge, Guang-Hua Duan, Bart Kuyken, and Gunther Roelkens. *Narrow line width frequency comb source based on an injection-locked III/V-on-silicon mode-locked laser*. *Opt. Express*, 24(5):5277–5286, Mar 2016.
- [86] Lukas Drzewietzki, Stefan Breuer, and Wolfgang Elsäßer. *Timing jitter reduction of passively mode-locked semiconductor lasers by self- and external-injection: Numerical description and experiments*. *Opt. Express*, 21(13):16142–16161, Jul 2013.
- [87] Francesco G. Della Corte, Giuseppe Cocorullo, Mario Iodice, and Ivo Rendina. *Temperature dependence of the thermo-optic coefficient of InP, GaAs, and SiC from room temperature to 600 K at the wavelength of 1.5 μm*. *Applied Physics Letters*, 77(11):1614–1616, sep 2000.
- [88] Ewoud Vissers, Stijn Poelman, Hans Wenzel, Heike Christopher, Kasper Van Gasse, Andrea Knigge, and Bart Kuyken. *Hybrid integrated mode-locked laser using a GaAs-based 1064 nm gain chip and a SiN external cavity*. *Optics Express*, 30(23):42394, nov 2022.
- [89] H. M. J. Bastiaens, G. Neijts, A. Memon, Y. Fan, J. Mak, D. Geskus, M. Hoekman, V. Moskalenko, E. A. J. M. Bente, and K.-J. Boller. *Broadband optical frequency comb generation using hybrid integrated InP-Si<sub>3</sub>N<sub>4</sub> diode lasers*. In *2021 Conference on Lasers and Electro-Optics Europe & European Quantum Electronics Conference (CLEO/Europe-EQEC)*. IEEE, jun 2021.
- [90] Ewoud Vissers, Stijn Poelman, Camiel Op de Beeck, Kasper Van Gasse, and Bart Kuyken. *Hybrid integrated mode-locked laser diodes with a silicon nitride extended cavity*. *Optics Express*, 29(10):15013, apr 2021.

- 
- [91] Kasper Van Gasse, Zaijun Chen, Edoardo Vicentini, Jeonghyun Huh, Stijn Poelman, Zhechao Wang, Gunther Roelkens, Theodor W. Hänsch, Bart Kuyken, and Nathalie Picqué. *An on-chip III-V-semiconductor-on-silicon laser frequency comb for gas-phase molecular spectroscopy in real-time*, 2020.
- [92] Artur Hermans, Kasper Van Gasse, Jon Ø. Kjellman, Charles Caër, Tasuku Nakamura, Yasuhisa Inada, Kazuya Hisada, Taku Hirasawa, Stijn Cuyvers, Sulakshna Kumari, Aleksandrs Marinins, Roelof Jansen, Günther Roelkens, Philippe Soussan, Xavier Rottenberg, and Bart Kuyken. *High-pulse-energy III-V-on-silicon-nitride mode-locked laser*. *APL Photonics*, 6(9):096102, sep 2021.
- [93] Zhechao Wang, Kasper Van Gasse, Valentina Moskalenko, Sylwester Latkowski, Erwin Bente, Bart Kuyken, and Gunther Roelkens. *A III-V-on-Si ultra-dense comb laser*. *Light: Science & Applications*, 6(5):e16260–e16260, dec 2016.



